

A General-Purpose Self-Supervised Model for Computational Pathology

Richard J. Chen^{1,2,3,4,5‡}, Tong Ding^{1‡}, Ming Y. Lu^{1,2,3,4,6‡}, Drew F. K. Williamson^{1,2,3‡}, Guillaume Jaume^{1,2,3,4}, Bowen Chen^{1,2}, Andrew Zhang^{1,2,3,4,7}, Daniel Shao^{1,2,3,4,7}, Andrew H. Song^{1,2,3,4}, Muhammad Shaban^{1,2,3,4}, Mane Williams^{1,2,3,4,5}, Anurag Vaidya^{1,2,3,4,7}, Sharifa Sahai^{1,2,3,4,9}, Lukas Oldenburg¹, Luca L. Weishaupt^{1,2,3,4,7}, Judy J. Wang¹, Walt Williams^{1,8}, Long Phi Le^{2,7}, Georg Gerber¹, Faisal Mahmood^{*1,2,3,4,10}

¹*Department of Pathology, Brigham and Women’s Hospital, Harvard Medical School, Boston, MA*

²*Department of Pathology, Massachusetts General Hospital, Harvard Medical School, Boston, MA*

³*Cancer Program, Broad Institute of Harvard and MIT, Cambridge, MA*

⁴*Cancer Data Science Program, Dana-Farber Cancer Institute, Boston, MA*

⁵*Department of Biomedical Informatics, Harvard Medical School, Boston, MA*

⁶*Electrical Engineering and Computer Science, Massachusetts Institute of Technology (MIT), Cambridge, MA*

⁷*Health Sciences and Technology, Harvard-MIT, Cambridge, MA*

⁸*Harvard John A. Paulson School of Engineering And Applied Sciences, Harvard University, Cambridge, MA*

⁹*Department of Systems Biology, Harvard University, Cambridge, MA*

¹⁰*Harvard Data Science Initiative, Harvard University, Cambridge, MA*

‡ *Contributed Equally*

***Corresponding author:** Faisal Mahmood (faisalmahmood@bwh.harvard.edu)

Tissue phenotyping is a fundamental computational pathology (CPath) task in learning objective characterizations of histopathologic biomarkers in anatomic pathology. However, whole-slide imaging (WSI) poses a complex computer vision problem in which the large-scale image resolutions of WSIs and the enormous diversity of morphological phenotypes preclude large-scale data annotation. Current efforts have proposed using pretrained image encoders with either transfer learning from natural image datasets or self-supervised pretraining on publicly-available histopathology datasets, but have not been extensively developed and evaluated across diverse tissue types at scale. We introduce UNI, a general-purpose self-supervised model for pathology, pretrained using over 100 million tissue patches from over 100,000 diagnostic haematoxylin and eosin-stained WSIs across 20 major tissue types, and evaluated on 33 representative CPath clinical tasks in CPath of varying diagnostic difficulties. In addition to outperforming previous state-of-the-art models, we demonstrate new modeling capabilities in CPath such as resolution-agnostic tissue classification, slide classification using few-shot class prototypes, and disease subtyping generalization in classifying up to 108 cancer types in the OncoTree code classification system. UNI advances unsupervised representation learning at scale in CPath in terms of both pretraining data and downstream evaluation, enabling data-efficient AI models that can generalize and transfer to a gamut of diagnostically-challenging tasks and clinical workflows in anatomic pathology.

arXiv:2308.15474v1 [cs.CV] 29 Aug 2023

Introduction

The clinical practice of pathology involves performing a large range of tasks: from tumor detection and subtyping to grading and staging, and with thousands of possible diagnoses, a pathologist must be adept at solving an incredibly diverse group of problems, often simultaneously. Contemporary computational pathology (CPath) has expanded this array even further by enabling ‘omics’ predictions¹⁻³, direct prognostication⁴⁻⁷, and therapeutic response prediction⁸ from microscopic images, among other applications⁹⁻¹⁷. With a vast array of tasks and the fact that many tasks in pathology are difficult to acquire data for due to the rarity of the underlying diseases or the need for expensive manual annotations by pathologists, training a single deep learning model from scratch for every possible task is impractical. These factors have led to the broad reliance on transfer learning techniques in CPath, which have proven effective in tasks such as metastasis detection¹⁸, mutation prediction^{19,20}, prostate cancer grading²¹, and outcome prediction^{22,23}.

The transfer learning, generalization and scaling capabilities of self-supervised (or pretrained) models are intrinsically tied to the size and diversity of the training data²⁴⁻²⁸. In general computer vision, the development and evaluation of many fundamental self-supervised models²⁹⁻³⁴ are based on the ImageNet Large Scale Visual Recognition Challenge^{35,36}, starting with ImageNet-1K (IN-1K) encompassing 1.2 million images from 1,000 classes, followed by ImageNet-22K (IN-22K, 14.2 million images, 21,841 classes), and then even larger datasets such as LVD-142M²⁵, JFT-300M³⁷, and beyond³⁸⁻⁴⁰. Such models have also been described as “foundation models” due to their ability to adapt to a wide range of downstream tasks when pretrained on massive amounts of data at scale^{41,42}. In CPath, The Cancer Genome Atlas (TCGA, ~29,000 FFPE and Frozen H&E WSIs, 32 cancer types)⁴³ similarly serves as the basis for most self-supervised models^{44-58,58,59} along with other histology datasets⁶⁰⁻⁷², with a number of prior works demonstrating great progress in learning meaningful representations of histology tissue for clinical pathology tasks^{46,47,73-86}. However, current pretrained models for CPath remain constrained by: 1) limited size and diversity of pretraining data, as the TCGA is comprised of mostly primary cancer histology slides, and 2) limited evaluation of generalization performance across diverse tissue types, as many pan-cancer analyses and popular clinical tasks in CPath are also based on annotated histology region-of-interests (ROIs) and slides from TCGA^{3,19,20,22,83,87-94}. Addressing these two limitations is critical for the broader development of foundation models in CPath that can generalize and transfer to real-world clinical settings with widespread applications.

In this work, we build upon these prior efforts by introducing a new general-purpose, self-supervised vision encoder for pathology, **UNI**, a Vision Transformer (ViT-Large)⁹⁵ pretrained on the largest histology slide collection used in self-supervised learning to date, termed **Mass-100K**. Mass-100K is a pretraining dataset that consists of over 100 million tissue patches from 100,426 diagnostic H&E whole-slide images (WSIs) across 20 major tissue types collected from from Massachusetts General Hospital (MGH) and Brigham & Women’s

Hospital (BWH), as well as Genotype-Tissue Expression (GTEx) consortium⁹⁶, providing a rich source of information for learning objective characterizations of histopathologic biomarkers (**Figure 1a, Extended Data Table 1**). In the pretraining stage, we directly employ a self-supervised learning approach called DINOv2²⁵, which has been shown to yield strong, off-the-shelf representations for downstream tasks without the need for further finetuning with labeled data (**Figure 1b**); more details regarding model design and training are available in the **Online Methods**. We demonstrate the versatility of UNI on diverse machine learning settings within CPath, including ROI-level classification, segmentation and image retrieval, and slide-level weakly-supervised and semi-supervised learning (**Figure 1c**). In total, we assess UNI on 33 clinical tasks across anatomic pathology that range in diagnostic difficulty, such as nuclear segmentation, primary and metastatic cancer detection, cancer grading and subtyping, gene mutation prediction and molecular subtyping, organ transplant assessment, and several pan-cancer classification tasks which includes subtyping to 108 cancer types in the OncoTree cancer classification system⁹⁷ (**Figure 1d, Figure 2a**). In addition to outperforming previous state-of-the-art models such as CTransPath⁴⁶ and REMEDIS⁴⁷, we also demonstrate new capabilities such as resolution-agnostic tissue classification and few-shot class prototypes for prompt-based slide classification, highlighting the potential of UNI as a foundation model for further developing AI models in anatomic pathology.

Results

Pretraining scaling laws in CPATH.

A pivotal characteristic of foundation models lies in their capability to deliver improved downstream performance on a variety of tasks when trained on larger datasets. Though datasets such as CAMELYON16⁹ and TCGA-NSCLC⁹⁹ are commonly used to benchmark pretrained encoders using weakly-supervised multiple instance learning (MIL) algorithms^{46,49,100,101}, they only source tissue slides from a single organ and are mainly used for predicting binary disease states, which is not reflective of the broader array of disease entities seen in real-world anatomic pathology practice. Instead, we assess the generalization capabilities of UNI across diverse tissue types and disease categories by constructing a large-scale hierarchical classification task for CPath that follows the OncoTree (OT) cancer classification system⁹⁷. Using in-house BWH slides, we defined a dataset that comprises 5,564 WSIs from 43 cancer types further subdivided into 108 OncoTree codes, with at least 20 WSIs per OncoTree code. The dataset forms the basis of two tasks that vary in diagnostic difficulty: 1) 43-class cancer type classification (OT-43) and 2) 108-class OncoTree code classification (OT-108), which to our knowledge is the most label-complex CPath task proposed to date (**Figure 2a**). To assess scaling trends, we also pretrain UNI across varying data scales, with Mass-100K is subsetted to create: 1) Mass-22K (16 million histology image patches, 21,444 WSIs) and 2) Mass-1K (1 million images, 1,404 WSIs) (**Extended Data Table 2,3**). We assess UNI on Mass-1K/-22K/-100K on both OT-43 and OT108. For weakly-supervised slide classification, we follow the conventional paradigm of first pre-extracting patch-level features

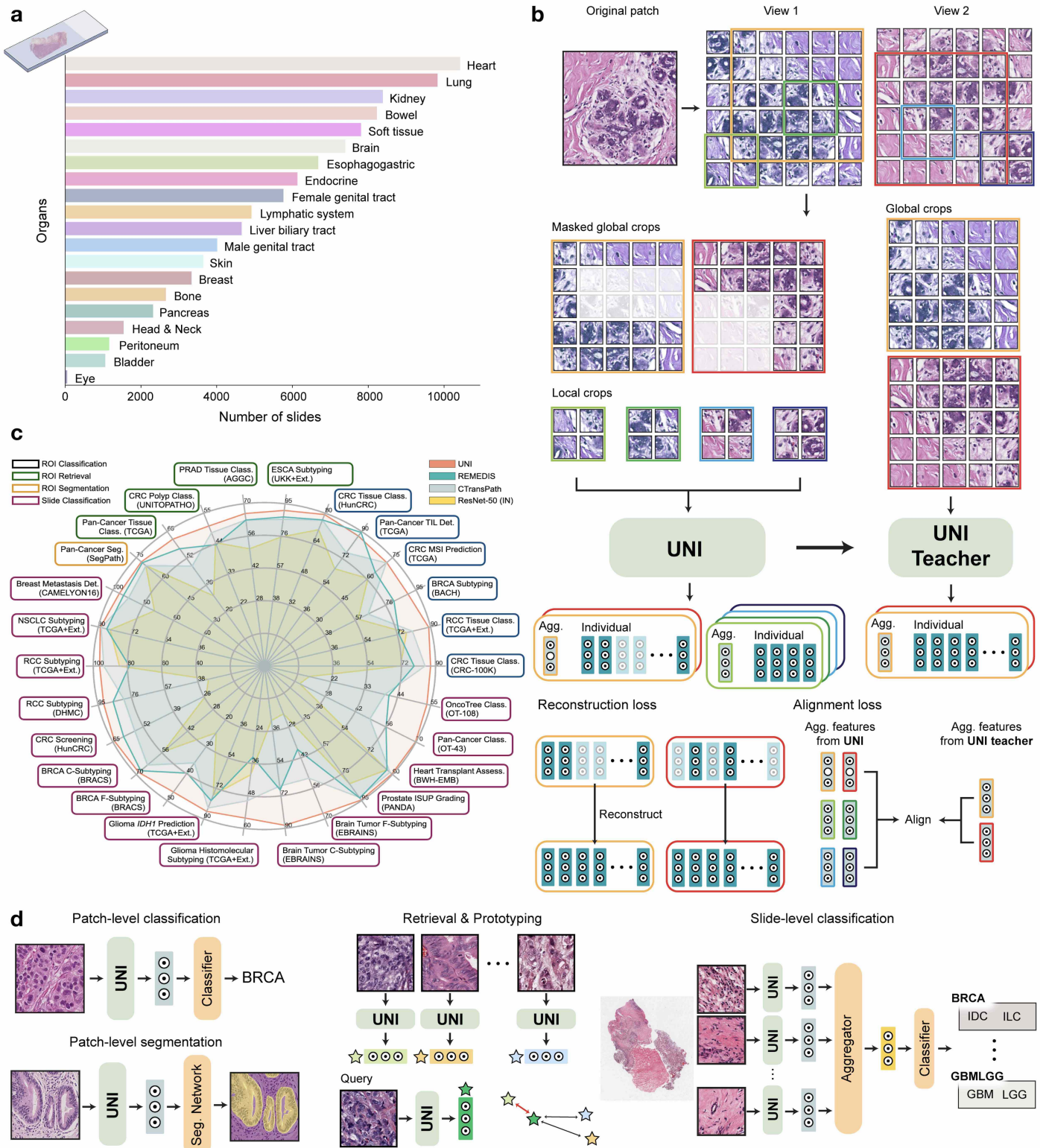


Figure 1: **Overview of UNI.** UNI is a general-purpose, self-supervised vision encoder for anatomic pathology based on the Vision Transformer architecture, achieving state-of-the-art performance across 33 clinical tasks in anatomic pathology. **a.** Slide distribution of Mass-100K, a large-scale and diverse pretraining dataset of 100 million tissue patches sampled from over 100,000 diagnostic whole-slide images across 20 major organ types. **b.** UNI is pretrained on Mass-100K using the DINOv2 self-supervised training algorithm²⁵, which consists of: 1) a mask image modeling objective⁹⁸ and a self-distillation objective³⁰. **c.** UNI outperforms other pretrained encoders on 33 clinical tasks in anatomical pathology (average performance of the 8 SegPath tasks reported). **d.** The evaluation tasks are comprised of ROI-level classification, segmentation, retrieval & prototyping, and slide-level classification tasks. Further details are described in the **Online Methods**.

from tissue-containing patches in the WSI using a pretrained encoder, followed by training an Attention-Based MIL (ABMIL) algorithm¹⁰² that localizes and aggregates patch-level features with high diagnostic relevance for predicting the slide-level label. To reflect the label complexity challenges of these tasks, we report top- k accuracy ($k = 1, 3, 5$) as well as weighted F1 and AUROC performance, with top-1 and top-5 accuracy as the primary evaluation metrics. Additional details regarding the OncoTree classification tasks are described in the **Online Methods**, distribution of cancer types and OncoTree codes provided in **Extended Data Table 4**, with detailed reporting of all model performances provided in **Extended Data Table 10-13**.

Overall, we demonstrate data scaling capabilities of self-supervised models in UNI, with the scaling trend for UNI on OT-43 and OT-108 visualized in **Figure 2c** and **Figure 2e**. On OT-43, we observe a +4.2% and +3.6% performance increase (both $p < 0.001$, two-sided paired permutation test) in top-1 and top-5 accuracy when scaling UNI from Mass-1K to Mass-22K, and a +3.7% and +0.7% performance increase ($p < 0.001$) when scaling from Mass-22K to Mass-100K. Similarly, on OT-108, we observe a +6.5% and +8.6% performance increase ($p < 0.001$) when comparing UNI pretrained on Mass-1K versus Mass-100K. **Extended Data Table 11** and **Extended Data Table 13** illustrate the effect of the number of images seen by UNI when evaluating intermediate checkpoints on OT-43 and OT-108 respectively, demonstrating gains with longer pretraining in addition to increasing dataset size. After 50,000 training iterations (115 million samples seen by the network during pretraining), UNI pretrained on Mass-22K outperforms UNI on Mass-100K on OT-43, with comparable performance on OT-108. When comparing models with 50,000 iterations (115 million samples) versus 125,000 iterations (384 million samples), performance on OT-43 and OT-108 monotonically increases for UNI pretrained on Mass-100K, whereas UNI performance pretrained on Mass-22K is less stable and decreases compared to earlier iterations. These scaling trends align with findings observed in many ViT models applied to natural images^{24,38,95}, in which the performance of larger ViT variants improves as the pretraining dataset grows.

We compare UNI pretrained on Mass-100K to publicly-available pretrained encoders used in CPath on OT-43 and OT-108 tasks: 1) ResNet-50¹⁰³ pretrained on IN-1K, 2) CTransPath⁴⁶ pretrained on TCGA and PAIP¹⁰⁴, and 3) and REMEDIS⁴⁷ pretrained on TCGA. We observe that UNI outperforms all baselines by a wide margin. On OT-43, UNI achieves a top-5 accuracy of 93.8% and AUROC of 0.976, outperforming the next best-performing model (REMEDIS) by +6.3% and +0.022 on these respective metrics (both $p < 0.001$) (**Figure 2b**, **Extended Data Table 10**). On OT-108, we observe a similar margins of performance increase with +10.8% and +0.020 ($p < 0.001$) over REMEDIS (**Figure 2c**, **Extended Data Table 12**). On more challenging performance metrics such as top-1 accuracy, UNI outperforms the next best-performing models by +13.8% and +12.6% on OT-43 and OT-108, respectively. We observe similar performance gains with other UNI configurations over these models. We also emphasize the superior pretraining efficiency of UNI over others. Though UNI is pretrained on a larger histology dataset (number of total patches and WSIs included),

CTransPath and REMEDIS are respectively trained $4\times$ and $13\times$ longer than UNI (total number of images seen).

Weakly-supervised slide classification.

We investigate UNI’s capabilities further across a diverse range of 15 slide-level classification tasks, which include: breast cancer metastasis detection (CAMELYON16)⁹, ISUP grading in prostate cancer (PANDA)²¹, and cardiac transplant assessment (in-house BWH slides)¹⁰⁵ among others. Similar to the OT-43 and OT-108 evaluations, we compare the pre-extracted features from UNI with that of other pretrained encoders in training ABMIL for weakly-supervised slide classification. As CTransPath and REMEDIS were trained using almost all TCGA slides, the reported performance of these models on TCGA tasks may be contaminated with data leakage and thus unfairly inflated. As a result, we exclude TCGA tasks that lack external test cohorts from our comparisons. A detailed description of tasks and evaluations are provided in the **Online Methods**, with detailed reporting of all slide classification performance presented in **Extended Data Table 10-26**.

Across all 15 slide-level classification tasks, UNI consistently outperforms all baselines (ResNet-50, CTransPath, REMEDIS), with more substantial improvements observed on tasks characterized by higher diagnostic complexity (**Figure 2f**). On conventional cancer detection and subtyping and detection benchmark tasks such as NSCLC subtyping (trained on TCGA⁹⁹ and tested on CPTAC¹⁰⁶⁻¹⁰⁸) and RCC subtyping (trained on TCGA¹⁰⁹⁻¹¹¹ and tested on CPTAC¹¹² and DHMC¹¹³) and breast metastasis detection (official folds in CAMELYON16), UNI achieves balanced accuracy scores of 88.9%, 96.3% and 95.7% respectively, outperforming the conventional ResNet-50 baseline (by +3.7%, $p < 0.001$; +13.9%, $p < 0.001$; +23.1%, $p < 0.001$) as well as CTransPath (by +0.5%, $p = 0.598$; +2.4%, $p = 0.408$; +6.0%, $p = 0.102$) and REMEDIS (by +3.5%, $p < 0.001$; +17.3%, $p = 0.001$; +2.7%, $p = 0.247$) (**Extended Data Table 14-16**). On more challenging tasks such as the ISUP grading task in PANDA, UNI achieves a balanced accuracy of 75.7% and a quadratic weighted Cohen’s κ of 0.946, outperforming the next best-performing model (REMEDIS) by +4.6% ($p < 0.001$) and +0.014 ($p < 0.05$) on these respective metrics (**Extended Data Table 25**). On hierarchical classification tasks such as BRCA subtyping in BRACS¹¹⁴ (**Extended Data Table 5**), we observe increases in balanced accuracy and AUROC over the next best-performing model (REMEDIS) when scaling from the coarse-grained subtyping task (+1.1%, $p = 0.865$; +0.023, $p = 0.442$) to the fine-grained subtyping task (+7.0%, $p = 0.285$; +0.088, $p < 0.01$) (**Extended Data Table 19 and 20**). For further assessment of UNI’s performance on hierarchical classification tasks, we also developed several challenging slide-level tasks of varying label complexity using the EBRAINS Digital Tumor Atlas¹¹⁵ and the TCGA-GBMLGG cohort^{116,117}, which include: a 2-class glioma *IDH1* mutation prediction task, a 5-class glioma histomolecular subtyping task (predicting both *IDH1*/1p19q status and histologic subtype), a 12-class brain tumor subtyping task (predicting main cancer type), and a 30-class brain tumor subtyping task (predicting diagnosis) (**Extended Data Table**

6,7). On these 4 respective tasks, UNI achieves balanced accuracy scores of 85.6%, 56.2%, 88.3% and 67.5%, outperforming the next best-performing model (either CTransPath or REMEDIS), by +2.0% ($p = 0.076$), +6.4% ($p = 0.001$), +19.6% ($p < 0.001$), and +16.1% ($p < 0.001$) respectively (**Extended Data Table 21-24**). Overall, UNI achieves the highest average supervised performance across all tasks 77.4%, with average performance increases of +26.4%, +8.3%, and +10.0% respective to ResNet-50 (51.0%), CTransPath (69.1%) and REMEDIS (67.4%).

Data contamination is a growing concern in foundation models trained on large collections of public datasets¹¹⁸⁻¹²². Though labels may not be explicitly leaked into the model during self-supervised training, models evaluated with transductive inference (*e.g.* the test set is made available to the model in either unsupervised or supervised training) may exhibit optimistically-biased performance, which has been empirically observed in CPath¹²³. Though comparisons of all pretrained encoders were evaluated on held-out testing data that were not seen during pretraining, we also assess and compare UNI against CTransPath and REMEDIS on TCGA-evaluated data in the NSCLC subtyping, RCC subtyping, glioma *IDH1* mutation prediction and glioma histomolecular subtyping tasks. We note that though all ABMIL models in these tasks were developed on histology slides of their respective TCGA data sources, all results presented in **Figure 2** are from evaluation on external data sources (CPTAC, DHMC, and EBRAINS). To study optimistic bias of self-supervised models with transductive inference, we additionally hold out an internal test fold in TCGA in our supervised evaluation of these tasks, a common practice in many CPath study designs that use TCGA^{49,56,100,101}. We denote all results with transductive inference as “gray” in **Extended Data Table 15, 16, 21, 22**.

In comparing UNI against REMEDIS and CTransPath on TCGA-evaluated data, we not only find UNI still outperforms these models on several tasks, but also observe substantial performance decreases when comparing the in-domain versus out-of-domain performance of these models. Foremost, UNI still outperforms the ResNet-50 baseline on these tasks, with an overall improvement of +12.78%. On NSCLC and RCC subtyping, UNI interestingly outperforms CTransPath by a larger margin on the internal TCGA test sets than the external test cohorts (+2.0% versus +0.5% on NSCLC subtyping, +5.5% versus +2.4% on RCC subtyping). Compared to REMEDIS, though UNI reaches the best performance on NSCLC subtyping, REMEDIS reaches a best balanced accuracy of 97.3% on the TCGA test set in RCC subtyping (compared to 94.7% from UNI). However, we observe substantial performance decreases in REMEDIS (97.3% to 79.0% from internal to external test set evaluation), whereas UNI maintains its performance (increasing from 94.7% to 96.3%). We make a similar observation in glioma *IDH1* mutation prediction, in which both CTransPath and REMEDIS outperform UNI on the TCGA test set (89.1% and 81.9% respectively compared to 80.8%), but then underperform on the EBRAINS test set (decrease to 83.6% and 79.2% in CTransPath and REMEDIS respectively, with increase to 85.6% in UNI). On glioma histomolecular subtyping, UNI achieves the best performance on internal and external test evaluation. Overall, we find evidence of data contamination of self-supervised models in CPath

when evaluated on the same data source used in pretraining. We emphasize that data contamination only exists in how the models are utilized, not in the models themselves which have been demonstrated to transfer well in on clinical settings independent of TCGA^{47,74,75,80}. However, as many CPath studies are reliant on TCGA, UNI is more generalizable and adaptable to clinical settings (both pre-clinical research and clinical translation) studying diverse cancer types.

Label efficiency of few-shot slide classification.

To study the label efficiency of UNI in the MIL paradigm, we additionally evaluate all slide-level tasks using few-shot learning. Few-shot learning is an evaluation scheme that studies the generalization capabilities of pretrained models on new tasks (C classes) given a limited number of examples (K training samples per class, also called supports or shots), and is posed as solving a “ C -way, K -shot” learning task. For all pretrained encoders, we trained an ABMIL model with $K \in \{1, 2, 4, 8, 16, 32\}$ training examples per class, where K is limited to 32 due to small support sizes in rare disease categories. As the performance can fluctuate depending on which K examples are chosen for each class, we repeat experiments over five runs with $C \cdot K$ training examples randomly sampled each time. A detailed description of our few-shot MIL experimentation is provided in the **Online Methods**, with few-shot performance for all tasks summarized in **Extended Data Figure 1**.

UNI generally outperforms all other baselines when trained and evaluated with the same number of training examples per class within each task, consistently demonstrating superior label efficiency (**Figure 2g-j, Extended Data Figure 1**). When comparing the 4-shot performance of UNI with that of other models (using the median performance), aside from the coarse-grained BRACS subtyping task, UNI outperforms all other baselines on all tasks, with the next best-performing model needing up of $8\times$ as many training examples per class to reach the same 4-shot performance of UNI. On challenging tasks such as fine-grained brain tumor subtyping in EBRAINS, the 4-shot performance of UNI outperforms other models by a large margin, only matched by the 32-shot performance of REMEDIS (**Figure 2i**). On ISUP grading in PANDA, UNI is consistently twice as label efficient across all few-shot settings (**Figure 2j**). For several tasks such as BRACS subtyping and glioma *IDH1* mutation prediction, the 1-shot UNI performance is lower than that of other pretrained encoders, with performance gains not observed until 4-shot training and evaluation (**Figure 2g, Extended Data Figure 1h**). Overall, our comprehensive evaluation of slide classification tasks demonstrates UNI’s potential as the foundational model to be used routinely for histopathology research tasks, outperforming other baselines in performance and label efficiency.

Supervised ROI classification in linear classifiers.

In addition to slide-level tasks, we also assess the capabilities of UNI on a diverse set of 10 ROI-level tasks

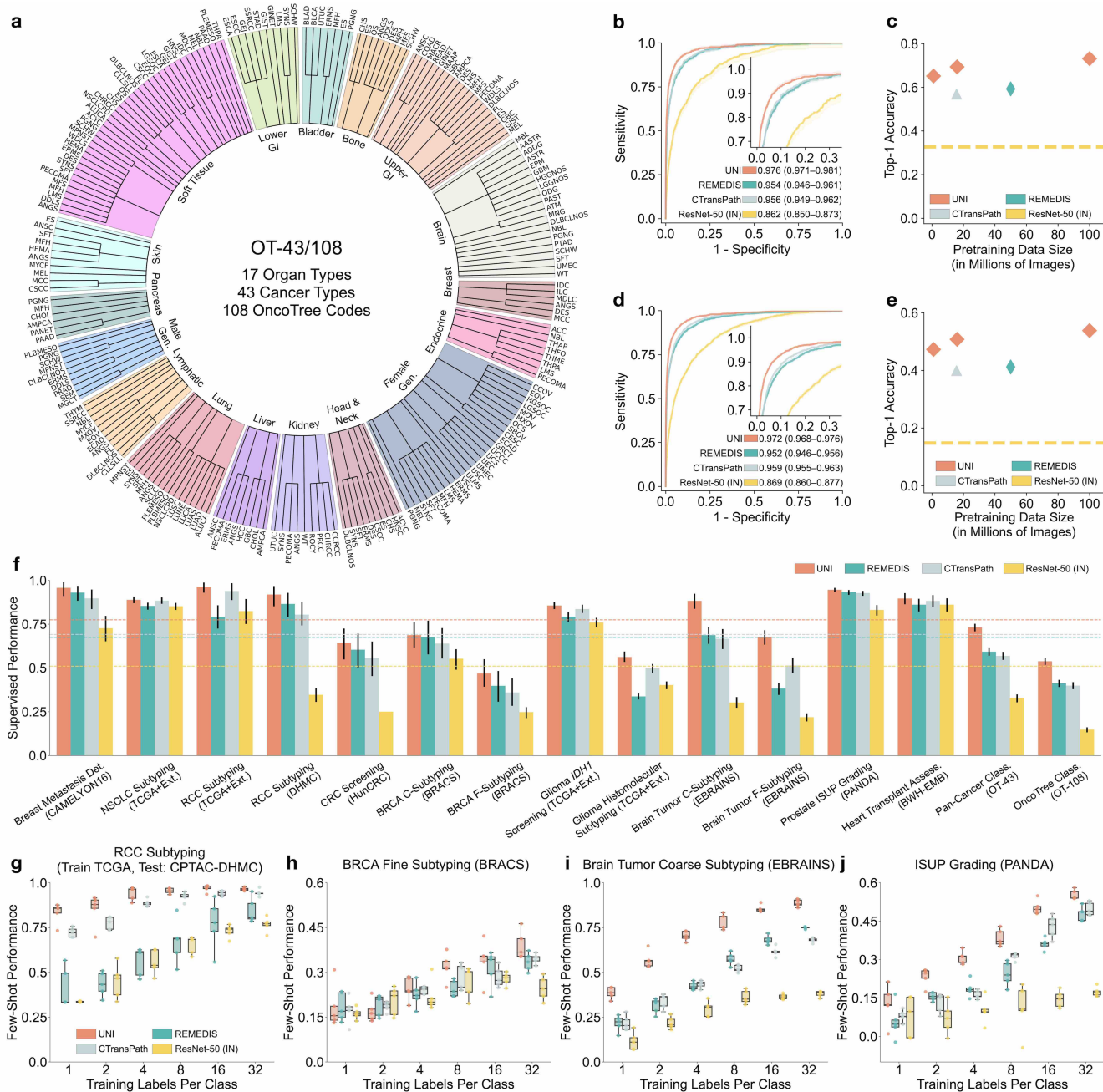


Figure 2: Slide-level tasks for OncoTree-43, OncoTree-108, and other slide-level tasks. **a.** Organ and OncoTree code distribution for the slide-level OncoTree-43 (OT-43) and OncoTree-108 (OT-108) classification tasks. All comparisons with UNI are evaluated on 43-way cancer type classification and 108-way oncotree code classification tasks with OT-43 and OT-108, respectively. Further details regarding data distribution are provided in **Extended Data Table 4**. **b.** AUROC comparisons of UNI with other pretrained encoders on OT-43. **c.** Top-1 accuracy comparisons of UNI across different pretraining data scales (Mass-1K, Mass-22K, Mass-100K) on OT-43. **d.** AUROC comparisons of UNI with other pretrained encoders on on OT-108. **e.** Top-1 accuracy comparisons of UNI across different pretraining data scales (Mass-1K, Mass-22K, Mass-100K) on OT-108. **f.** Supervised performance of UNI and its comparisons across 15 weakly-supervised slide-level classification tasks. Detailed performance metrics for all slide classification tasks are further provided in **Extended Data Table 10-26**. **g-j.** The few-shot slide-level performance with $K \in \{1, 2, 4, 8, 16, 32\}$ slides per class reported for four tasks. Boxes indicate quartile values of model performance ($n = 5$ runs) and whiskers extend to data points within $1.5 \times$ the interquartile range, with comparisons on all tasks visualized in **Extended Data Figure 1**.

of different tissue types, which include: colorectal tissue and polyp classification (CRC-100K-NONORM¹²⁴, HunCRC¹²⁵, UniToPatho¹²⁶), CCRCC tissue classification (TCGA)¹²⁷, CRC microsatellite instability (MSI) prediction (TCGA)³, PRAD tissue classification (AGGC)¹²⁸, BRCA subtyping (BACH)¹²⁹, ESCA subtyping (UKK)¹³⁰, and two pan-cancer tasks: tumor-immune lymphocyte (TIL) detection⁸⁷ and 32-class cancer tissue classification (TCGA)⁸⁸. We note that 3 out of 10 tasks were trained and evaluated on TCGA, which may unfairly inflate the performance of CTransPath and REMEDIS in comparisons. To mitigate potential biases of site-specific staining variability in TCGA-derived tasks¹³¹, we stain normalize¹³² all images in CRC MSI prediction, TIL detection, and 32-class pan-cancer tissue classification. For tasks that do not have official train-test folds, we also case- and site-stratify all samples when possible, such as using ROIs from the Helsinki Hospital (HEL) subset in the CCRCC tissue classification task and ROIs from the University Hospital Berlin—Charité (CHA) subset in the ESCA subtyping task as external cohorts respectively. For evaluation and comparisons, we perform logistic regression and K-nearest neighbors (KNN) on top of the pre-extracted features of each encoder, a common practice referred to as linear probing and KNN probing which measure discriminative performance and representation quality of pre-extracted features respectively²⁸. We evaluate all tasks using balanced accuracy, with PRAD tissue classification additionally evaluated using weighted F1 score¹²⁸. A detailed description of ROI tasks and evaluation settings (linear and KNN probing) are provided in the **Online Methods**, with detailed reporting of all ROI classification performance presented in **Extended Data Table 27-46**.

Across all 10 ROI-level tasks, UNI outperforms nearly all baselines on all tasks with statistical significance, with overall improvements of +19.9%, +9.5%, +7.7% on linear probing for ResNet-50, CTransPath, and REMEDIS respectively **Figure 3a**. On conventional ROI benchmarks such as CRC tissue classification (CRC-100K) with linear probing, UNI outperforms ResNet-50 (+15.9%, $p < 0.001$), CTransPath (+2.9%, $p < 0.001$) and REMEDIS (+8.7%, $p < 0.001$) by significant margins. Similar performance gains are also seen on more challenging tasks such as PRAD tissue classification (in weighted F1 score, +0.131, $p < 0.001$; +0.020, $p < 0.001$; +0.027, $p < 0.001$) and ESCA subtyping (+25.3%, $p < 0.001$; +10.1%, $p < 0.001$; +5.5%, $p < 0.001$) for all three models respectively. **Figure 3b** visualizes UNI predictions on prostate cancer grading, in which a simple linear classifier trained with pre-extracted UNI features can achieve high agreement with pathologist annotations (**Extended Data Figure 2**). On CRC MSI prediction and TIL detection, CTransPath and REMEDIS achieve similar or better performance than UNI, which we note are 2 out of the 3 tasks that were pretrained and evaluated on TCGA data only. Interestingly, on a 32-class pan-cancer tissue classification task curated entirely from TCGA, UNI achieves the highest overall balanced accuracy and AUROC of 65.7% and 0.975, still outperforming the next best-performing model (REMEDIS) by +4.7% and +0.017 (both $p < 0.001$). In comparing performances with and without stain normalization, we observe a uniform decrease in performance across all pretrained encoders (**Extended Data Figure 41-46**). On KNN probing, UNI similarly outperforms ResNet-50, CTransPath, and REMEDIS with an average of +16.9%, +10.1%, +9.4%

performance increase across all tasks.

ROI retrieval.

In addition to using the semantically-rich representations extracted from UNI for building task-specific classifiers in a supervised learning setting, representations can also be used to perform content-based image retrieval (CBIR). In CBIR, a query image is used to find similar images from a large database - *e.g.* images sharing similar morphologies, diagnosis, or tissue site. Specifically, the query image is embedded into a low-dimensional feature representation using UNI, and then compared to other candidate images in the embedding space via a KNN look-up. For simplicity, we evaluate and compare the effectiveness of UNI with other baselines in retrieving histopathology image ROIs, and acknowledge that more sophisticated preprocessing, indexing, ranking, and filtering techniques may be used to boost performance, scalability and speed^{58,89,133,134} further. We evaluate histology image retrieval on 6 ROI-level tasks (tasks with at least 5 classes). In each task, we consider Acc@K for $K \in \{1, 3, 5\}$, which represent the standard top-K accuracy scores in retrieving images with the same class label as the query and MVAcc@5, which more strictly enforces that the majority vote of retrieved images must be the same class as the query for retrieval to be considered successful. For each task we use the same test set introduced in the supervised ROI-level evaluation section as queries and treat the supervised training set as the database of keys. Note that no supervised learning occurs in these experiments, and the labels are only used for evaluation. Additional details regarding ROI retrieval are provided in the **Online Methods**, with detailed reporting of all retrieval tasks provided in **Extended Data Table 47-52**.

UNI outperforms other encoders on all tasks, demonstrating superior retrieval performance across diverse settings. On PRAD tissue classification (AGGC), UNI outperforms the next best-performing model (REMEDIS) by +4.3% and +3.6% on Acc@1 and MVAcc@5, respectively (both $p < 0.001$). A similar trend is noted for CRC tissue classification (HunCRC) (by +2.8% and +2.5% respectively compared to REMEDIS, both $p < 0.001$), ESCA subtyping (by +3.8% and +3.0% respectively compared to REMEDIS, both $p < 0.001$) and CRC polyp classification (UniToPatho) (by +2.4%, $p = 0.037$ and +3.3%, $p < 0.001$ respectively compared to CTransPath). On CRC tissue classification (CRC-100K), the gap between the top performing models is relatively small (by +1.8%, $p < 0.001$ and +1.0%, $p = 0.015$ respectively compared to REMEDIS), presumably because the different tissue types have very distinct morphology, as shown by the relatively high classification performance in linear probing. Lastly, on the more challenging 32-class pan-cancer tissue classification task, UNI outperforms the second-best performing model REMEDIS by a large margin of +4.6% for Acc@1 and +4.2% for MVAcc@5 (both $p < 0.001$).

Representation quality of extracted features from high image resolutions.

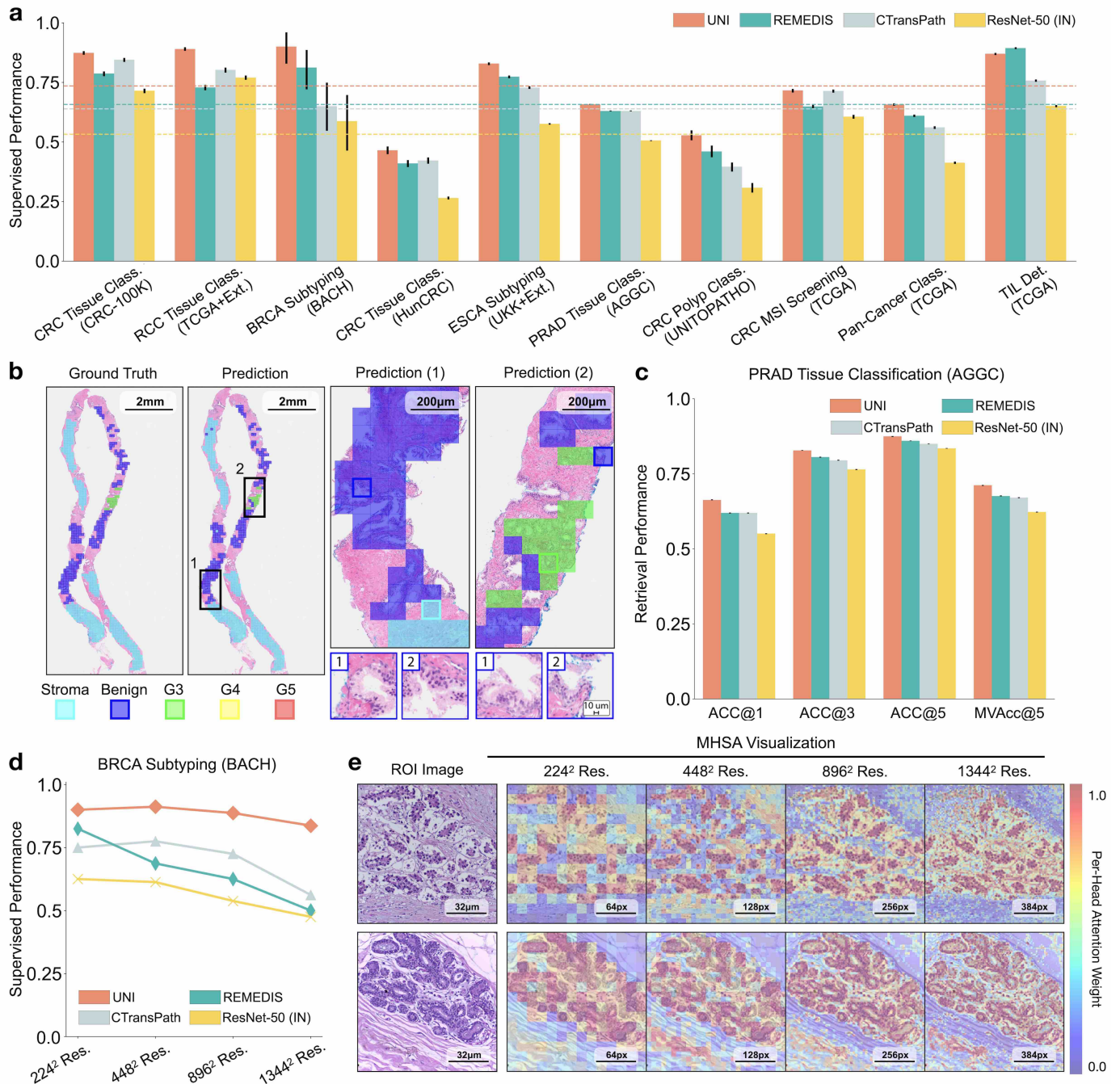


Figure 3: **ROI-level tasks.** **a.** Supervised linear probe performance of UNI across 10 ROI-level classification tasks. Dashed lines represent average performance of each model across all tasks, with error bars representing 95% confidence intervals. **b.** Illustrative examples of UNI on ROI classification for prostate adenocarcinoma (PRAD) tissue classification in AGGC. **Left** panel shows ground truth ROI-level labels overlaid on the WSI, and **right** panel shows predicted patch labels. Regions of interest are enlarged for better visualization, with further comparisons visualized in **Extended Data Figure 2**. **c.** ROI retrieval performance of UNI on PRAD tissue classification. We report Recall@ K for $K \in \{1, 3, 5\}$ and the mean recall, with error bars representing 95% confidence intervals. All ROI retrieval comparisons are provided in **Extended Data Figure 6**. **d.** Supervised KNN probe performance of UNI across various image resolutions in BRCA subtyping in BACH. **e.** Multi-head self-attention (MHSA) heatmap visualization of UNI across different image resolutions in BACH. Each colored square represents a 16×16 patch token encoded by UNI, with heatmap color corresponding to the attention weight of that patch token to the global [CLS] token of the penultimate layer in UNI. **Top** and **bottom** respectively show visualizations for the invasive- and normal-labeled images, with further visualizations and interpretations provided in **Extended Data Figure 3-5**.

Though the evaluation of visual recognition models is mostly performed on resized 224×224 (224^2) images, we note that image resizing operations may change the image magnification and thus alter the interpretation of certain morphological features such as cellular atypia. To this end, we additionally study the representation quality of UNI’s extracted features at varying resolutions in the BRCA subtyping (BACH) and CRC polyp classification (UniToPatho) tasks. Specifically, we resize and center-crop the original ROI images (BRCA subtyping - 2048×1536 at 0.42 microns per pixel or mpp, & CRC polyp classification - 1812×1812 at 0.44 mpp) to $\{224^2, 448^2, 896^2, 1344^2\}$ and $\{224^2, 448^2, 896^2, 1792^2\}$ size, respectively, and perform linear and KNN probing. We note that all pretrained encoders use data augmentations that would change the image aspect ratio during self-supervised learning, with UNI additionally pretrained on high-resolution images following DINOv2. Additional details regarding multiple resolution evaluation are provided in the **Online Methods** and dataset descriptions for BRCA subtyping and CRC polyp classification, with detailed reporting of ROI classification performance for all resolutions reported in **Extended Data Figure 3, Extended Data Table 31, 32, 37, 38**.

On both tasks, we observe UNI can adapt to high resolutions images, outperforming all comparisons across almost all resolutions and evaluation metrics. When evaluating on 224^2 -resized images (2.88 mpp) in BRCA subtyping, UNI outperforms the next best-performing model (CTransPath) by +5.0% and +15.0% on balanced accuracy in linear and KNN probing (**Figure 3d, Extended Data Figure 3a**). On 224^2 -resized images (3.60 mpp) in CRC polyp classification, UNI outperforms CTransPath by +7.2% on linear probing, with lower performance than CTransPath on KNN probing (**Extended Data Figure 3b**). When scaling the image resolutions used for evaluation, we observe wider margins of improvement as UNI outperforms CTransPath on 1344^2 -resized images (0.48 mpp) in BRCA subtyping (by +25.0% linear probe, $p < 0.001$; by +27.5% KNN probe, $p < 0.001$), and 1792^2 -resized images (0.45 mpp) in CRC polyp classification (by +13.2% linear probe, $p < 0.001$; by +6.2% KNN probe, $p < 0.001$). Additionally, we observe that UNI performance is robust across resolutions for both tasks, with the minimum and maximum performance gap ranges -5.0% (linear) and -7.5% (KNN) for BRCA subtyping and +2.6% (linear) and +5.1% (KNN) for CRC polyp classification. Such robustness is missing in other pretrained encoders, such as the -22.5% (linear) and -21.3% (KNN) performance gap for BRCA subtyping using CTransPath. In **Figure 2e** and **Extended Data Figure 4-5**, we can further visualize high-attention 16×16 patch tokens (represented as a colored square) that contribute to the extracted feature representation of UNI via interpretation of multi-head self-attention (MHSA) weights. In 224^2 -resized images from the BRCA subtyping task in BACH, In comparing MHSA heatmap visualizations across increasing image resolutions in BRCA subtyping, we observe that the high-attention 16×16 patch tokens in UNI become more fine-grained in localizing individual cells, with more specific delineation of tumor-stroma boundaries observed in 1344^2 -resized images. Interestingly, in 224^2 -resized images, we find that high-attention patch tokens are still able to localize invasive tumor cell nests and the cell-lining of ducts at a low resolution, which demonstrates UNI capabilities in encoding resolution-agnostic features. In contrast to CRC polyp classification, we observe

that high-attention patch tokens in UNI for 224²-resized images have poor specificity in corresponding to any cell- or tissue-based morphological patterns in comparison with that of 1796²-resized images, which alludes to the important effect of image resizing on ROI datasets (**Extended Data Figure 5**). Overall, these observations suggest that UNI can encode semantically-meaningful representations agnostic to most image resolutions, which is especially valuable in CPath tasks known to be optimal at different image magnifications.

ROI cell type segmentation.

We assess UNI on the largest, public ROI-level segmentation dataset, SegPath¹³⁵, a dataset for segmenting 8 major cell types in tumor tissue: epithelial cells, smooth muscle cells, red blood cells, endothelial cells, leukocytes, lymphocytes, plasma cells, and myeloid cells. Segmentation masks for each cell type were obtained via immunofluorescence and DAPI nuclear staining. All pretrained encoders are finetuned end-to-end using Mask2Former¹³⁶, a flexible framework commonly used for evaluating the off-the-shelf performance of pretrained encoders^{25, 137, 138}. As the SegPath dataset divides the cell types into separate dense prediction tasks (8 tasks total), each model is individually finetuned per cell type, with the dice score used as the primary evaluation metric. As plain (non-hierarchical) ViT architectures lack vision-specific inductive biases for dense prediction tasks¹³⁹, we additionally used the ViT-Adapter module alongside the Mask2Former head for finetuning UNI^{25, 140}. Additional details regarding segmentation tasks are provided in the **Online Methods**, with detailed reporting of all segmentation tasks provided in **Extended Data Table 53**.

Though hierarchical vision backbones such as Swin Transformers (CTransPath) and Convolutional Neural Networks (ResNet-50 and REMEDIS) have well-known advantages over plain backbones (ViT-Large in UNI) on dense prediction tasks, we observe UNI still outperforms all comparisons on a majority of cell types in SegPath. On individual segmentation tasks for the epithelial, smooth muscle, and red blood cell types, UNI achieves dice scores of 0.827, 0.690, and 0.803, outperforming the next best-performing model (REMEDIS) by +0.003 ($p = 0.164$), +0.016 ($p < 0.001$), and +0.008 ($p = 0.001$). On other segmentation tasks, UNI is the best-performing model on most cell types, with comparable results on lymphocyte (0.651 vs. 0.653, $p = 0.419$), and plasma cell segmentation (0.737 vs. 0.742, $p = 0.378$) against the best-performing model (REMEDIS). Across all 8 cell types in SegPath, UNI achieves the overall performance with an average dice score of 0.721, outperforming ResNet-50 (0.696), CTransPath (0.695), and REMEDIS (0.716). Despite architectural constraints in using plain ViTs, we demonstrate that UNI is still competitive with state-of-the-art CNN and hierarchical vision models on cell segmentation.

Few-shot ROI classification with class prototypes.

Similar to slide-level classification, we also assess the label-efficiency of UNI on ROI-level tasks. We evaluate

all pretrained encoders using the non-parametric SimpleShot framework¹⁴¹, a strong baseline in the few-shot classification literature that proposes averaging extracted feature vectors of each class as the support examples in $K = 1$ nearest neighbors (or nearest centroid) classification¹⁴². These averaged feature vectors can also be viewed as “class prototypes”, a set of one-shot exemplars that are unique in representing semantic information such as class labels (*e.g.*, LUAD versus LUSC morphologies). At test time, unseen test examples are assigned the label of the nearest class prototype via Euclidean distance (**Figure 4a**). For all pretrained encoders, we evaluate their pre-extracted features using SimpleShot with $K \in \{1, 2, 4, 8, \dots, 256\}$ training examples per class for a majority of tasks (BRCA subtyping, CRC tissue classification in HunCRC, and ESCA subtyping limited to $K = 64, 128, 128$ respectively), with experiments repeated over 1000 runs where $C \cdot K$ training examples are sampled for each run. A detailed description of the SimpleShot framework is provided in the **Online Methods**, with few-shot performance for all tasks summarized in **Extended Data Figure 7**.

We observe similar label efficiency trends as few-shot slide classification in few-shot ROI classification tasks, as UNI outperforms all pretrained encoders across almost all tasks and few-shot evaluation settings. In the 1-shot and 2-shot evaluation of most tasks, though the median value for UNI is generally higher than that of the next best-performing model, the variance in balanced accuracy performance across runs is very high, which can be attributed to poor selection of support examples. However, as the number of support examples increases in forming the class prototypes, we observe a monotonic decrease in variance of few-shot performance runs (0.32 – 1.59% standard deviation across tasks in UNI’s 256-shot performance), which demonstrates performance stability in permuting training examples to average as class prototypes in SimpleShot. When comparing the median 8-shot performance of UNI with that of other models, UNI consistently exceeds the 128-shot and 256-shot performance of the next best-performing model on many tasks (16 – 32× label efficiency), which include challenging tasks such as PRAD tissue classification (AGGC), CRC polyp classification (UniToPatho), pan-cancer tissue classification (TCGA), and other tasks (**Figure 4c-e, Extended Data Figure 7**). On these tasks, we also observe several instances in which the lowest few-shot performance of UNI exceeds the median and even the maximum few-shot performance reported across 1000 runs of other models. On PRAD tissue classification, the lowest-performing runs for UNI in 32-shot and 128-shot evaluation outperforms the best-performing run possible for CTransPath and REMEDIS, respectively. We observe a similar finding in CRC polyp classification, in which the lowest-performing run for UNI in 64-shot evaluation outperforms the median performance of all few-shot evaluation settings for CTransPath and REMEDIS. In pan-cancer tissue classification, the lowest-performing run for UNI in 2-shot, 8-shot, and 32-shot evaluation outperforms the best possible run possible for ResNet-50, CTransPath, and REMEDIS, respectively. To assess SimpleShot-like evaluation in a fully-supervised setting, we also report results in using all training examples as the support set for forming class prototypes, in which SimpleShot evaluation reaches competitive performance with linear and KNN probing. Overall, these findings demonstrate not only the label efficiency of UNI in discriminative tasks, but also its superior representation quality, such that averaging the extracted features for a few ROIs can create

effective class prototypes.

Prompt-based slide classification using class prototypes.

Though weakly-supervised learning via MIL has shifted slide-level classification to no longer requiring patch-level annotations¹⁸, accessing and curating histology slide collections may still exist as barriers for clinical tasks that address rare and underrepresented diseases. Moreover, ROI-level analysis is still an important component of many study designs in CPath in further post-hoc interpretability of MIL^{22,143,144} and other fine-grained assessment of the tissue microenvironment^{17,87,92,145–149}. From observing the strong retrieval performance and few-shot capabilities in UNI, we re-visit the problem of few-shot slide classification using a semi-supervised, prompt-inspired approach based on class prototypes. Previous works in CPath have demonstrated that textual prompts encoding class labels (known as a class prompt) can be used for “zero-shot” slide classification⁷⁶, in which the class prompt with the best average retrieval score computed using their top- K retrieved patches (top- K average pooling) assigns the slide label. We note that SimpleShot and textual prompting, though using different modalities, perform retrieval-based classification using an embedding space. Though the requirement of annotations for class prototype construction prevents zero-shot learning in the SimpleShot setting, we demonstrate UNI only needs a few examples per class. Similar to textual prompting, we used the class prototypes from SimpleShot as “prompts” for top- K average pooling of retrieved patches (with class prototypes replacing textual prompts), which we term Multiple Instance SimpleShot (MI-SimpleShot) (**Figure 4b**). We evaluate this approach on two slide-level tasks which have matching ROI training examples from datasets that can be used as the support set - NSCLC subtyping (**Figure 4f**) and RCC subtyping (**Figure 4g**), which can be used in conjunction with the annotated LUAD, LUSC, CCRCC, PRCC, and CHRCC ROIs from the pan-cancer tissue classification task based on TCGA⁸⁸. Similar to our evaluation in few-shot slide classification, we evaluate MI-SimpleShot on $\{1, 2, 4, 8, 16, 32\}$ training slides per class using the same 5 folds as the trained ABMIL models, with prototypes created from ROIs annotated within the same training slides. We compare against pre-extracted features of other encoders using MI-SimpleShot, as well as the MIL baseline for UNI. We also develop similarity heatmaps that visualize the normalized Euclidean distances of all patches within a slide with respect to the class prototype of the ground-truth label, with pathologist annotations of tissue regions that match the slide label outlined in blue. A detailed description of the MI-SimpleShot framework is provided in the **Online Methods**, with further reporting of results provided in **Extended Data Figure 8,9**, and **Extended Data Table 54,55**

Using only a few annotated ROI examples per class as prototypes, we demonstrate the potential of applying UNI with MI-SimpleShot as a simple but highly-efficient system for slide-level disease subtyping and detection. On NSCLC and RCC subtyping (trained on TCGA and tested on external cohorts), MI-SimpleShot with top-5 pooling achieves better performance than ABMIL when using 1, 2, and 4 training slides per class

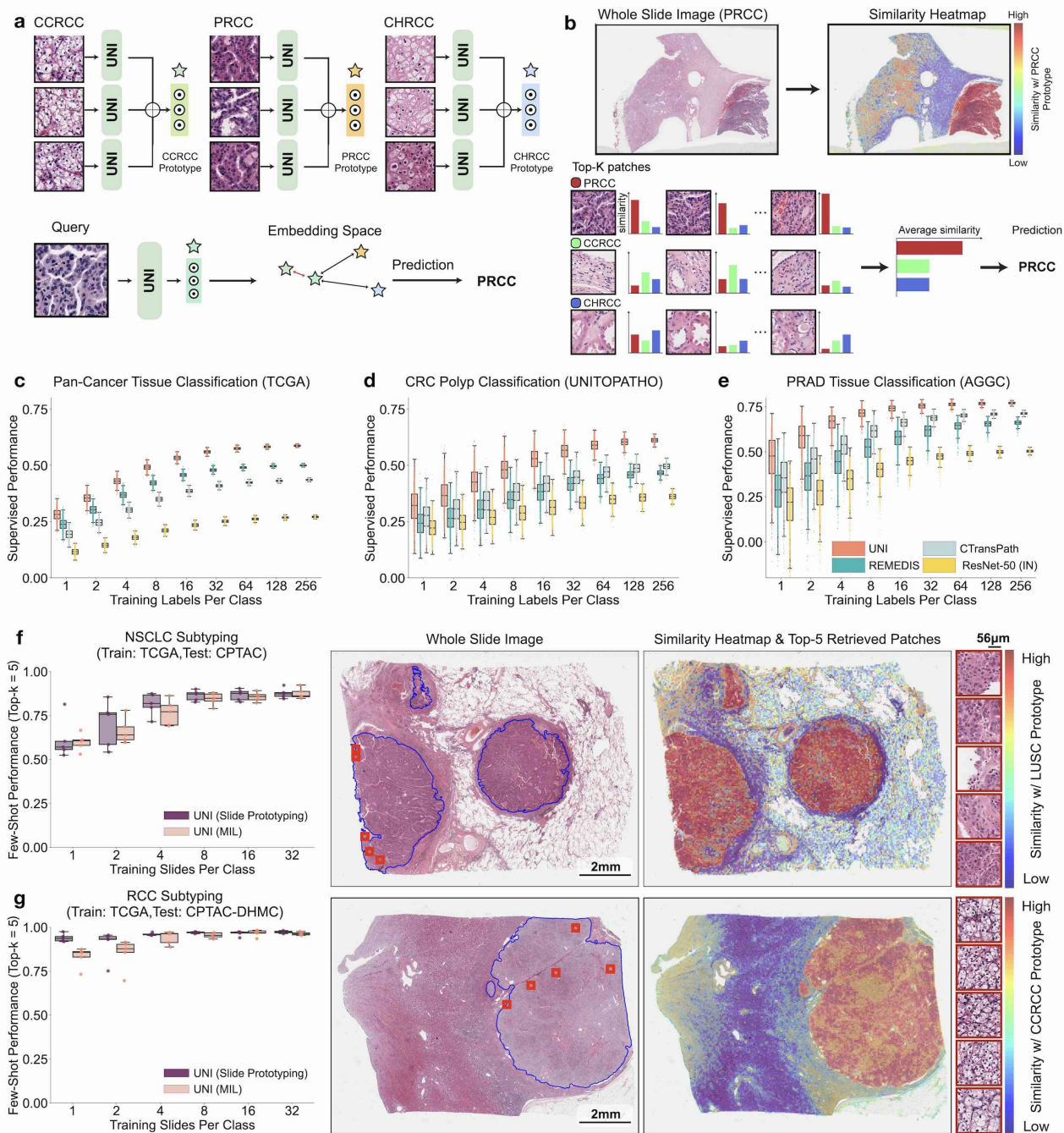


Figure 4: Few-shot ROI- and slide-level prototyping. **a.** Prototypical few-shot ROI classification via SimpleShot. A class prototype is constructed by averaging the extracted features from ROIs of the same class. For a test ROI, SimpleShot assigns the class of the most similar class prototype (smallest Euclidean distance) as the predicted ROI label. **b.** Prototypical few-shot slide classification via MI-SimpleShot. Using a precomputed set of ROI-level class prototypes (sharing the same class labels as the slide), MI-SimpleShot predicts the slide label using the class prototype with the highest average similarity of top K patches queried from the WSI. The similarity heatmap visualizes the similarity between the ground-truth class prototype and each patch in WSI. **c-e.** Few-shot ROI classification performance via SimpleShot on three tasks, with boxes indicating quartile values of model performance ($n = 1000$ runs) and whiskers extend to data points within $1.5\times$ the interquartile range. **f-g.** Few-shot slide classification performance and similarity heatmaps via MI-SimpleShot on NSCLC subtyping (**f**) and RCC subtyping (**g**). In both tasks, using pre-extracted features from UNI, we compare MI-SimpleShot in the same few-shot settings as ABMIL ($K \in \{1, 2, 4, 8, 16, 32\}$ slides per class, 5 runs), and visualize similarity heatmaps and the top-5 similar patches (indicated in red bounding boxes) for a LUSC (**f**) and CCRCC (**g**) slide, with further methodological details, comparisons, visualizations, interpretations provided in the **Online Methods** and **Extended Data Figure 7, 8, 9**.

for creating prototypes, and achieves similar performance to ABMIL when using more slides (**Figure 4f,g**). From visualization of similarity heatmaps, we also observe that retrieved patches of UNI (corresponding to the slide label) has strong agreement with pathologist annotations, as observed in the right-hand side of **Figure 4f,g** for LUSC and CCRCC slides. We believe that the effectiveness of MI-SimpleShot is due to a combination of: 1) no trainable parameters needed in MI-SimpleShot, whereas ABMIL models may still over- and underfit in few-shot settings, and 2) the strong representation quality of features extracted by UNI. Compared to other pretrained encoders, UNI demonstrates $8\times$ label efficiency on both NSCLC and RCC subtyping (**Extended Data Figure 8**). When using all training slides, UNI achieves balanced accuracy scores of 90.2% on NSCLC subtyping, outperforming the next best performing model (CTransPath) by +5.7% ($p < 0.001$). On RCC subtyping, UNI achieves comparable results to the best performing model, REMEDIS (95.2% vs. 95.7%, $p = 0.511$). Interestingly, we note that REMEDIS performance via MI-SimpleShot on RCC subtyping outperforms that of ABMIL (79%, $p < 0.001$), which demonstrates the general versatility of MI-SimpleShot when coupled with pretrained encoders. We observe similar trends when using top-50 average pooling, and performance for all MI-SimpleShot experiments (**Extended Data Figure 8, Extended Data Table 54, 55**). Lastly, while REMEDIS, CTransPath, and even ResNet-50_{IN} can also be used to create similarity heatmaps (**Extended Data Figure 9**), we observe instances of label mismatch in the slide prediction and retrieved patches, in which either: 1) retrieved patches of the class prototype (corresponding to the slide label) had poor agreement with the pathologist’s annotations, or 2) retrieved patches had strong agreement with the pathologist’s annotation but the slide was misclassified. Overall, our comprehensive evaluation of MI-SimpleShot reinforces the strong representation quality of UNI and its potential as a foundational model that can be used in routine clinical tasks.

Discussion

Given the large range of tasks performed in the practice of anatomic pathology and those enabled by computational pathology (CPath) techniques, transfer learning has been a cornerstone of rapid progress in the field. Many works in CPath have leveraged image encoders trained on a large database of natural images (such as ImageNet) or, more recently and showing better performance, those trained using large public repositories of histopathology data such as the TCGA^{46–48,66}. However, there is still room for improvement in the performance of these approaches and further, these studies have generally focused on relatively narrow tasks and disease morphologies, ignoring the full diversity seen in histopathology slides in practice.

In this study, we demonstrate the versatility of UNI, a general-purpose, self-supervised model pretrained on the largest histology slide collection (for self-supervised learning) to date in CPath. We curated Mass-100K, a large and diverse pretraining dataset containing over 100 million tissue patches from 100,426 whole-slide images (WSIs) across 20 major organ types including normal tissue, cancerous tissue, and other pathologies. The

size of our pretraining dataset, coupled with the DINOv2 self-supervised learning approach (demonstrated to scale well to large dataset sizes)²⁵, allow UNI to significantly outperform other histopathology image encoders across a range of 33 clinical tasks that include a variety of formulations of ROI-level classification, retrieval, segmentation, and slide classification. Additionally, we also demonstrate new capabilities of self-supervised models in CPath, which include resolution-agnostic feature extraction, few-shot slide classification using class prototypes, and disease subtyping generalization of up to 108 labels in the OncoTree classification task. Lastly, as UNI is also trained on mostly in-house histology slides, UNI can be used freely for further development and evaluation of AI models on many public clinical tasks in CPath such as those derived from TCGA.

Our study has several limitations. Based on the plain ViT-Large architecture, UNI lacks vision-specific inductive biases for solving dense prediction tasks in CPath such as cell segmentation, and note that observed performance increases in SegPath are not as drastic as in other tasks. Though UNI still outperforms the next best-performing model (REMEDIS), we envision further improvement as better recipes emerge for adapting plain ViT architectures¹⁴⁰. In addition, our study also does not evaluate the best-performing ViT-Giant architecture in DINOv2, an even larger model that would likely translate well in CPath but remains out of scope due to the enormous computational resources needed for pretraining. Though our study organizes the largest collection of clinical tasks for evaluating pretrained models in CPath (to our knowledge), other clinical tasks such as those in hematopathology are not represented in our analyses. Moreover, UNI is a unimodal model for CPath, with multimodal capabilities such as image captioning, cross-modal retrieval, and zero-shot classification remaining out-of-scope, which we explore in concurrent work²⁷. Due to these limitations and also following conventional nomenclature of self-supervised models in computer vision^{25,95}, though UNI demonstrates state-of-the-art results across many clinical applications, further development is needed before a “visual foundation model” is achieved that would serve all use cases in anatomic pathology.

Online Methods

Large-scale visual pretraining

In developing and evaluating self-supervised models in CPath, an important and relatively under-discussed challenge is the difficulty in developing large-scale models that can also be used for evaluation on public histology datasets. For natural images, IN-1K is an integral dataset for the model development and evaluation lifecycle of self-supervised learning methods. Specifically, models are first pretrained on the training set of IN-1K and then evaluated with finetuning and linear probe performance on the validation set (treated as the test set) reported as a community-accepted “goodness-of-fit”^{150,151}, with further evaluation of generalization performance via other downstream tasks such as fine-grained classification and activity video recognition. Though such off-the-shelf self-supervised learning methods can readily be adapted to CPath, we note that

there is considerably less public data for pretraining in CPath than natural images, and that pretraining on large, public collections of histology slides also restricts their adaptability for public CPath benchmarks. Specifically, development of many self-supervised pathology models have been limited to pretraining on TCGA⁴³, one of the largest and most diverse public histology datasets for CPath, with many models opting using the entire TCGA collection in order to realize data scaling benefits in self-supervised learning^{46,47,152}. However, their usability in evaluating on public CPath benchmarks may be restricted to transductive inference^{44,46,49,50,56,78,152}, as many popular clinical tasks in CPath are also derived from TCGA (*e.g.* - pan-cancer analyses^{3,19,20,22,83,87-94}) and thus limits extensive evaluation of out-of-domain, generalization performance. Though datasets such as CAMELYON^{9,10} and PANDA²¹ can be used in evaluating TCGA-pretrained models, we note that these datasets are limited to single tissue types with limited disease categories.

Dataset curation for Mass-100K. To overcome this limitation, we present *Mass-100K*, a large-scale and diverse pretraining dataset comprised of in-house histology slides from Massachusetts General Hospital (MGH) and Brigham & Women’s Hospital (BWH), and external histology slides from the Genotype-Tissue Expression (GTEx) consortium. Following natural image datasets, we also created three partitions of Mass-100K that vary in size in order to evaluate the data scaling laws, an empirical observation found in natural language and image foundation models that scaling dataset size would also increase model performance^{24,25,28,95}. Analogous to IN-22K and IN-1K, we developed the Mass-22K dataset, which contains 16,059,454 histology image patches sampled from 21,444 diagnostic formalin-fixed paraffin-embedded (FFPE) haematoxylin and eosin (H&E) WSIs across 20 major tissue types comprised of mostly cancer tissue, as well as its subset Mass-1K (1,064,615 images, 1,404 WSIs). All histology slides in Mass-22K and Mass-1K were collected from BWH, and scanned using an Aperio GT450 scanner or a Hamamatsu S210 scanner. To make the image dataset sizes roughly equivalent to that of IN-22K and IN-1K, we sample approximately 800 image patches from histology tissue regions of each WSI, with image resolutions of 256×256 pixels at $20\times$ magnification. For slide preprocessing, we adapted the WSI preprocessing in the CLAM toolbox¹⁰⁰, which performs: 1) tissue segmentation at a low resolution via binary thresholding of the saturation channel in RGB→HSV color space, 2) median blurring, morphological closing, and filtering contours below a minimum area to smooth tissue contours and remove artifacts, 3) patch coordinate extraction of non-overlapping 256×256 tissue patches in the segmented tissue regions of each WSI at $20\times$ magnification. The distribution of Mass-22K and Mass-1K are respectively reported in **Extended Data Table 2** and **Extended Data Table 3**.

Inspired by even larger natural image datasets such as LVD-142M²⁵ and JFT-300M³⁷, we developed Mass-100K, which combines Mass-22K with further in-house FFPE H&E histology slide collections (including renal and cardiac transplant tissue) and GTEx⁹⁶ which is comprised of 24,782 non-cancerous, human autopsy WSIs. Additional in-house slides were collected from both BWH and MGH, and scanned using an Aperio GT450 scanner or a Hamamatsu S210 scanner. We purposefully excluded using other public histology

slide collections such as TCGA, CPTAC, and PAIP for external evaluation of UNI. Altogether, Mass-100K includes 100,426 histology slides, with its distribution reported in **Extended Data Table 1**. Following the slide preprocessing protocol reported above, sampling approximately 800 histology tissue patches per WSI in Mass-100K yielded 75,832,905 images at 256×256 pixels at $20\times$. For high-resolution finetuning in DINOv2, we sampled an additional 24,297,995 images at 512×512 pixels at $20\times$, which altogether yielded 100,130,900 images for pretraining in Mass-100K.

Network architecture and pretraining protocol. For large-scale visual pretraining on Mass-100K, we used DINOv2²⁵, a state-of-the-art self-supervised learning method based on student-teacher knowledge distillation for pretraining large ViT architectures. DINOv2 is an extension of two previous methods (DINO³⁰ and iBOT⁹⁸) and uses two main loss objectives: self-distillation loss (*i.e.*, alignment loss in **Figure 1b**) and masked image modeling loss (*i.e.*, reconstruction loss in **Figure 1b**), which achieves state-of-the-art results in linear probe accuracy. DINOv2 also demonstrates capabilities in understanding the semantic layout of histopathology images when pretrained using knowledge distillation¹⁵². Self-distillation, introduced in BYOL³² for CNN pretraining and DINO³⁰ for ViT pretraining, minimizes the predictive categorical distributions from the teacher (**UNI Teacher** in **Figure 1b**) and student network (**UNI** in **Figure 1b**) obtained from two augmented views of the same image by minimizing their cross-entropy loss. The teacher is updated as an exponential moving average of previous iterations of the student. Masked image modeling using an online tokenizer, introduced in iBOT⁹⁸, involves strategically masking specific regions within an input image and training the model to predict the masked regions based on the remaining contextual information. This approach captures high-level visual features and context, inspired by masked language modeling in BERT¹⁵³. Specifically, we denote two augmented views of an input image x as u and v , which are subsequently randomly masked. The masked images of u and v are represented as \hat{u} and \hat{v} , respectively. While u and v are propagated through the teacher network, the student network receives \hat{u} and \hat{v} as inputs. For the self-distillation objective, we compute cross-entropy loss between the [CLS] token from the teacher network and the [CLS] token from the student network. For the masked image modeling objective, DINOv2 utilizes the output of the masked tokens from the student network to predict the patch tokens from the teacher network, where the teacher network can be regarded as an online tokenizer. We used DINOv2 as an important property for pretrained vision models in histopathology is linear probe performance, as these models are often used as frozen feature extractors for pre-extracting patch features in weakly-supervised slide-level tasks. Though other ViT-based self-supervised methods have demonstrated superior finetuning performance^{24,154}, their linear probe performance are not comparable and note that full-finetuning in ROI-level and slide-level tasks is not always feasible due to cost in collecting annotations.

Additionally, we note that DINOv2 is an extension of iBOT⁹⁸ which also uses the two loss objectives described above. Both methods are originally based on the original DINO framework³⁰ (which introduced student-teacher knowledge distillation for ViTs). Specifically, iBOT extends DINO by introducing an on-

line tokenizer component for masked image modeling, and DINOv2 extends iBOT by introducing additional modifications to improve training stability and efficiency for larger ViT architectures. The DINOv2 modifications can be summarized as the following: 1) untying the head weights between the above loss objectives⁹⁸, 2) Sinkhorn-Knopp centering instead of teacher softmax-centering⁹⁸, 3) KoLeo regularizer to improve token diversity¹⁵⁵, 4) high-resolution finetuning toward the end of pretraining¹⁵⁶, 5) an improved implementation of FLASHATTENTION¹⁵⁷, stochastic depth, and fully-sharded data parallel mechanisms, and 6) an improved pretraining recipe of the ViT-Large architecture on large-scale datasets. Of these modifications that DINOv2 proposes, we used the default configuration¹ which omits the modifications (1) and (2), as outlined in **Extended Data Table 8**. High-resolution finetuning was conducted on the last 12,500 iterations of pretraining (out of 125,000 iterations total).

Evaluation Setting

Comparisons & baselines. For slide- and ROI-level evaluation, we compare UNI against three pretrained encoders commonly used in the CPath community. As a comparison to models with ImageNet Transfer, we compare against a ResNet-50¹⁰³ pretrained on ImageNet³⁵ (truncated after the third residual block, 8,543,296 parameters), which is a commonly-used baseline in many slide-level tasks^{100,158}. As comparisons to the current state-of-the-art encoders, we compare against CTransPath⁴⁶, which is a Swin Transformer¹⁵⁹ using the "tiny" configuration with a window size of 14 (Swin-T/14, 28,289,038 parameters) pretrained mostly on the TCGA via MoCoV3²⁹, and REMEDIS⁴⁷, a ResNet-152×2 (232,230,016 parameters) initialized with the "Big Transfer"-medium protocol¹⁶⁰ on ImageNet-22K and then pretrained with SimCLR³¹. Regarding data distributions, CTransPath was pretrained using 29,753 WSIs across 25 anatomic sites in TCGA (including both FFPE and frozen tissue slides) and 2,457 WSIs from the Pathology AI Platform (PAIP)¹⁰⁴ across 6 anatomic sites, with 15,580,262 tissue patches and 32,120 WSIs used for pretraining altogether. REMEDIS was pretrained with a random sample of approximately ~ 50 million patches from 29,018 WSIs also across 25 anatomic sites in TCGA. For self-supervised learning, CTransPath was trained using the MoCoV3²⁹ algorithm for 100 epochs with approximately $\sim 1.56 \times 10^9$ (or 1.56 billion) images seen during pretraining, with REMEDIS trained using the SimCLR algorithm for a maximum of 1,000 epochs with upwards of $\sim 50 \times 10^9$ (or 50 billion) images seen during pretraining. In our implementation of these pretrained encoders, we use the truncated ResNet-50 implementation provided by CLAM¹⁰⁰, and used the official model checkpoints for CTransPath and REMEDIS. The image embeddings outputted by these models are 1024, 768, and 4096 respectively. Similar to ResNet-50 and other ResNet models in which the penultimate feature layer before the classification head is a grid-like feature map of $[1 \times 7 \times 7 \times 4096]$ -dimension, we apply a two-dimensional adaptive average pooling layer to output a single $[1 \times 4096]$ -dimensional image embedding. For all images used in ROI tasks and extracted patches for multiple instance learning (MIL) in slide tasks, across all models, all feature extraction

¹https://github.com/facebookresearch/dinov2/blob/main/dinov2/configs/ssl_default_config.yaml

operations are performed on resized 224×224 images, due to constraints in the Swin-T/14 architecture used by CTransPath which can only take image dimensions in which the length is divisible by 224. All pretrained encoders use ImageNet mean and standard deviation parameters for image normalization (including UNI).

Lastly, we note that while many slide and ROI tasks are created using annotated data using the TCGA, CTransPath and REMEDIS were also trained using almost all slides in the TCGA, which can result in information leakage that inflates the performance of these models on TCGA benchmarks. For all tasks, when possible, we report evaluation on external cohorts outside of TCGA. This may not be possible for all tasks, as the official train-validation-test folds may all be developed using TCGA.

Weakly-supervised slide classification. Training and evaluation for weakly-supervised slide classification tasks follows the conventional two-stage multiple instance learning (MIL) paradigm of: 1) pre-extracting ROI-level features as instances from non-overlapping tissue patches of segmented tissue regions of the WSI, 2) learning a trainable permutation-invariant pooling operator that aggregates patch-level (or instance) features into a single slide-level (or bag) feature. For slide preprocessing, we use the same WSI preprocessing pipeline as described in the dataset curation section which uses the CLAM toolbox¹⁰⁰, with additional patch feature extraction using a pretrained encoder performed on the patched coordinates. Images are resized down to 224×224 and normalized using ImageNet mean and standard deviation parameters. As quality control, we performed the additional following steps: 1) for slides with under- or over-segmented tissue masks, we adjust the segmentation parameters in CLAM (threshold value and downsample level) to segment only tissue regions, 2) removal of slides that were non-H&E and non-FFPE, and 3) for slides that did not have a downsample level equivalent to $20\times$ magnification in their WSI pyramidal format, we patched the tissue into non-overlapping 512×512 tissue patches at $40\times$ magnification and then later resized these images to 224×224 during feature extraction. Pre-extracted features for all pretrained encoders used the same set of patch coordinates for feature extraction of each WSI.

For comparison of pre-extracted features of pretrained encoders in weakly-supervised learning, we used the Attention-Based Multiple Instance Learning (ABMIL) algorithm¹⁰² across all tasks, which is a canonical weakly-supervised baseline in slide classification tasks. We use the two-layer gated variant of the ABMIL architecture with all input embeddings mapped to an embedding dimension of 512 in the first fully-connected (FC) layer, followed by hidden dimensions of 384 in the following intermediate layers. For regularization, we use dropout with $P = 0.10$ applied to the input embeddings and $P = 0.25$ after each intermediate layer in the network. Aside from the first FC layer which is dependent on the embedding dimension of the pre-extracted features, all comparisons used the same ABMIL model configuration. We trained all ABMIL models using the AdamW optimizer¹⁶¹ with a cosine learning rate scheduler, learning rate of $1e-4$, cross-entropy loss, and maximum 20 epochs. We additionally performed early stopping on the validation loss if a validation fold was

available. For all slide classification tasks, we case-stratified and label-stratified the slide dataset into train-validation-test folds, or used official folds if available. As CTransPath and REMEDIS were pretrained using all slides in TCGA, we considered TCGA slide tasks in which additional external evaluation was possible (e.g. - NSCLC subtyping was included due to availability of LUAD and LUSC slides in CPTAC, whereas BRCA subtyping was excluded). For glioma *IDH1* mutation prediction and histomolecular subtyping, train-validation-test folds were additionally site-stratified to mitigate potential batch effects.

Linear and K-nearest neighbors probe evaluation in ROI classification. For ROI-level classification tasks, we follow previous works that use logistic regression (linear) probing and K-nearest neighbors (KNN¹⁶²) probing for respectively evaluating discriminative transfer performance and representation quality of pre-extracted feature embeddings on downstream tasks²⁸. For linear probing, following the practice recommended by the self-supervised learning community, we fix the ℓ_2 regularization coefficient λ to $\frac{100}{MC}$, where M is the embedding dimension and C is the number of classes, and use the L-BFGS solver¹⁶³ with a maximum of 1000 iterations¹⁵⁰. KNN probing is an additional evaluation technique advocated by the self-supervised community for measuring representation quality of pre-extracted features^{30,164-168}. In comparison with linear probing, KNN probing is non-parametric (aside from the choice of K), as it classifies unseen test examples based on only their feature similarity with labeled training examples (e.g. similar examples in representation space should also be visually similar and share the same class label). We use the KNN implementation from Scikit-Learn¹⁶⁹ trained fitted using $K = 20$ and Euclidean distance as the distance metric, following observed stability of this evaluation setup of other self-supervised works³⁰. For all ROI tasks, we approximately case-stratified and label-stratified datasets into train-test folds, or used official folds if available.

For all tasks, we resize images to 224×224 (or 448×448 if available) and normalize using ImageNet mean and standard deviation parameters. Additionally, we note that many ROI datasets consist of images with high image resolutions, with image resizing to a fixed 224×224 or 448×448 resolution also changing the image magnification and microns per pixel (mpp). For example, resizing ROIs in the CRC polyp classification task in UniToPatho (ROIs having an original image resolution of 1812×1812 at 0.45 mpp) to 224×224 would change the magnification to 3.6 mpp. For CRC polyp classification as well as BRCA subtyping (BACH), we evaluate on resized image resolutions of $\{224^2, 448^2, 896^2, 1792^2\}$ and $\{224^2, 448^2, 896^2, 1344^2\}$, with multiples of 224 chosen due to constraints with CTransPath. To pre-extract features from high-resolution images, for ViTs such as the plain ViT-large architecture in UNI and the hierarchical Swin Transformer-T architecture in CTransPath, the forward passes of these architectures are not modified, interpolation of positional embeddings is performed to have the same sequence length as patch tokens in the ROI. To illustrate, in the patch embedding layer of our ViT-Large architecture in UNI that has a patch token size of 16×16 , a 224×224 image would be converted into a $[14 \times 14 \times D]$ -dimension 2D grid of patch embeddings using a 2D convolutional layer (kernel and stride size of 16, 3 incoming channels from RGB-input image inputs and

D -dim outgoing channels set as a hyper-parameter for feature embedding length), followed by flattening and transposing (now a $[196 \times D]$ -dimension sequence of patch embeddings), which can now be used in Transformer attention (called “patchifying”). For a 1792×1792 image in CRC polyp classification, patchifying this image using the same patch embedding layer would result in a $[112 \times 112 \times D] \rightarrow [12544 \times D]$ -dimension sequence of patch embeddings. Feeding this sequence into the forward pass of Transformer attention, though computationally expensive, is still tractable via memory-efficient implementations such as FLASHATTENTION or MEMEFFATTENTION². For positional embedding interpolation, we used the implementation provided in the DINO codebase³. For multi-head self-attention (MHSA) visualization, we visualize the weights from the last attention layer using the notebook implementation provided by the HIPT codebase^{152 4}, which we note is only applicable for plain ViT architectures.

ROI retrieval. To assess the quality of embeddings produced by different encoders for CBIR of histopathology images, we use ROI-level classification datasets, in which the goal is to retrieve similar images (*i.e.*, images with the same class label) to a given query image. For each benchmark, we first embed all images into a low-dimensional feature representation using the pretrained encoders. We treat each image in the test set as a query. Each query image is compared to each image from the ROI-level classification training set, which serves as a database of candidates (keys). Note that no supervised learning takes place in these experiments and the class labels are only used for evaluation purposes (*i.e.*, to assess whether retrieved images share the same class label as the query). We first center the database of keys by subtracting their Euclidean centroid from each embedding followed by ℓ_2 normalization of each key to unit length. For each new query, we apply the same shift and normalization steps, and then measure it against each key in the database via the ℓ_2 distance metric, where lower distance is interpreted as higher similarity. The retrieved images are sorted by their similarity scores and their corresponding class labels are used to evaluate the success of a given retrieval using Acc@K for $K \in 1, 3, 5$ and MVAcc@5, which are described in **Evaluation metrics**.

ROI-level cell type segmentation. For training and evaluation of ROI-level cell type segmentation tasks, we follow previous works in using Mask2Former, which is a flexible framework commonly used for evaluating off-the-shelf performance of pretrained vision encoders¹³⁶. In the case of the ViT architecture which is non-hierarchical, we additionally use the ViT-Adapter framework alongside the Mask2Former head¹⁴⁰. For both ViT-Adapter and Mask2Former, we use the same hyper-parameters used for ADE20k semantic segmentation. More specifically, we use the AdamW¹⁶¹ optimizer along with a step learning rate schedule. The initial learning rate was set to 0.0001, and a weight decay of 0.05 is applied. To adjust the learning rate specifically for the backbone, we apply a learning rate multiplier of 0.1. Additionally, we decay the learning rate by a factor of 10 at 0.9 and 0.95 fractions of the total number of training steps. For all backbones, we finetune the full model

²https://pytorch.org/docs/master/generated/torch.nn.functional.scaled_dot_product_attention.html

³https://github.com/facebookresearch/dino/blob/main/vision_transformer.py#L174

⁴https://github.com/mahmoodlab/HIPT/tree/master/HIPT_4K

for 50 epochs with a batch size of 16. The model’s performance on the validation set is evaluated every 5 epochs, and the optimal model based on validation performance is saved for testing. To augment the data, we use the large-scale jittering (LSJ) augmentation^{170,171}, with a random scale sampled from a range of 0.5 to 2.0, followed by a fixed size crop to 896×896 to accommodate the size constraints of CTransPath. At inference time, we resize the image dimensions to their nearest multiples of 224.

Few-shot ROI classification and prototype learning. For few-shot classification, we follow previous works that use the SimpleShot framework for evaluating the few-shot learning performance of prototypical representations of self-supervised models^{141,172}. Prototypical (or prototype) learning is a longstanding task in the few-shot learning community,^{142,173–176} and has been also posed (in many related forms) in CPath as well^{51,53,54,177,178}. In contrast with traditional few-shot learners based on meta learning, SimpleShot and related works demonstrate that strong feature representations combined with specific transformations and simple classifiers can reach state-of-the-art performance on few-shot tasks^{141,172,179}. SimpleShot is similar to nearest neighbors classification, in which the training set (called ”supports” in few-shot learning literature) is drawn from C classes (”ways”) with K examples per class (”shots”) for predicting unseen images in the test set (”queries”). Instead of nearest neighbors, SimpleShot uses a nearest-centroid approach based on ProtoNet¹⁴², in which the average feature vector (centroid) for each class is used as a prototypical ”one-shot” example for labeling the query set via distance similarity. As mentioned, these averaged feature vectors can also be viewed as ”class prototypes”, a set of one-shot exemplar examples that are unique in representing semantic information such as class labels (*e.g.*, LUAD versus LUSC morphologies). As SimpleShot is a simple and surprisingly strong baseline in the few-shot learning community and popularized in evaluating self-supervised models^{172,180–184}, we adopt this baseline in evaluating UNI and its comparisons in few-shot ROI classification tasks. We follow the recommendations in SimpleShot that suggest centering (subtracting the mean computed on the support set) and ℓ_2 normalizing the support set before computing the class prototypes, with the query set also transformed (also centered using the mean of the the support set) before nearest centroids classification.

Conventional few-shot learners on natural image classification tasks are evaluated by drawing 10,000 C -way, K -shot episodes from the training set with 15 query images per class as the test set. For equivalent comparison with metrics in linear and KNN probing, we instead draw 1000 C -way, K -shot episodes but use all images in the test set per episode. Due to the relatively larger number of training examples available in ROI tasks than that of slide tasks, we vary the number of labeled examples per class from $K \in \{1, 2, 4, 8, 16, 32, \dots, 256\}$ or the maximum number of labeled examples available for a given class. To compare with linear and KNN probing that use all training examples, we also evaluate SimpleShot by averaging all training examples per class, which we denote as ”1-NN” in **Extended Data Tables 28-46**.

Prompt-based slide classification using Multiple Instance (MI) SimpleShot. To evaluate the quality of ex-

tracted representations in serving as class prototype for slide classification tasks, we adapt class prototypes from SimpleShot (described above) as “prompts” (similar to usage of textual prompts in zero-shot classification⁷⁶, which we describe as Multiple Instance SimpleShot (MI-SimpleShot). As described in the main text, we use two slide-level datasets (NSCLC and RCC subtyping datasets) which have matching ROI training examples from datasets that can be used as the support set. Concretely, we use the annotated LUAD and LUSC ROIs from the TCGA Uniform Tumor dataset for NSCLC subtyping, and annotated CCRCC, PRCC, and CHRCC ROIs from the TCGA Uniform Tumor dataset for RCC subtyping. The TCGA Uniform Tumor dataset (described further in the **Online Methods**) consists of 271,170 256×256 ROIs at around 0.5 mpp of 32 cancer types annotated and extracted from 8,736 H&E FFPE diagnostic histopathology WSIs. We note that the number annotated ROIs per slide range from 10 to 70 examples in the TCGA-LUAD, -LUSC, -CCRCC, -PRCC, and -CHRCC cohorts. For each class, we first embed ROIs in the support set into a low-dimensional feature representation using the pretrained encoders, followed by average-pooling of all ROI features within the class. The average-pooled feature representations are considered as the class prototypes, which are used as “prompts” for labeling the top K ROIs for each slide in the query set via normalized Euclidean distance similarity. The slide-level prediction is then made by majority voting of the top K ROI predictions. For each benchmark, we evaluate MI-SimpleShot with both top-5 average pooling and top-50 average pooling and on $\{1, 2, 4, 8, 16, 32\}$ training slides per class similar to our evaluation in few-shot slide classification using the same 5 folds as the trained ABMIL models, with prototypes created from the annotated ROIs within the same training slides. We note little performance change in considering the average scores of the top-5 and top-50 patches per class prototype. To compare with the performance that uses all training slides with ROI annotations, we also evaluate MI-SimpleShot by averaging all training ROI feature representations per class, with results detailed in **Extended Data Table 54, 55**. To create similarity heatmaps, we visualize the normalized Euclidean distances of all patches within a slide with respect to the ground-truth class prototype.

Evaluation metrics. We report balanced accuracy, weighted F1 score, and AUROC for classification tasks. **Balanced accuracy** is computed by taking the unweighted average of the recall of each class, which takes into account class imbalance in the evaluation set. **Weighted F1 score** is computed by averaging the F1 score (the harmonic mean of precision and recall) of each class, weighted by the size of its respective support set. **AUROC** is the area under the receiver operating curve plotting true positive rate against the false positive rate as the classification threshold is varied. Additionally, we compute **quadratic weighted Cohen’s κ** (inter-annotator agreement between two sets of labels, *e.g.* - ground-truth and predictions) which we perform for ISUP grading (PANDA), and **top-K accuracy** for $K \in \{1, 3, 5\}$ (for a given test sample, a sample is scored correctly if the ground-truth label is among the top-K labels predicted) for OT-43 and OT-108. For retrieval, we consider **Acc@K** for $K \in \{1, 3, 5\}$, which represent the standard top-K accuracy scores in retrieving images with the same class label as the query. Specifically, a retrieval is considered successful if at least one image among the top-K retrieved images have the same class label as the query. We also report **MVAcc@5**, which

compared to Acc@5 more strictly enforces that the majority vote of the top 5 retrieved images must be the same class as the query for retrieval to be considered successful. For segmentation, we report the **Dice score** (same definition as the F1 score), the precision and recall, macro averaged across all images and classes.

Statistical analysis

For all semi- and fully-supervised experiments, we estimate 95% confidence intervals for the model performance with non-parametric bootstrapping using 1,000 bootstrap replicates. For statistical significance, we use a two-sided paired permutation test with 1,000 permutations to assess observed differences between the performance of two models. For all few-shot settings, we report results using box plots that indicate quartile values of model performance ($n = 5$ runs) with whiskers extending to data points within $1.5\times$ the interquartile range. For ROI-level few-shot classification, for each C -way, K -shot setting, we randomly sample K training examples per C classes with 1,000 repeated experiments (called “episodes” or “runs”) evaluated on the entire test set. For slide-level few-shot classification, we follow the same setting as above but with the number of runs limited to 5 due to small support sizes in rare disease categories.

Tasks and datasets

OncoTree Cancer Classification based on in-house BWH data (43 cancer types, 108 OncoTree codes) :

As described in the main text, OncoTree cancer classification is a large-scale hierarchical classification task for CPath that follows the OncoTree (OT) cancer classification system⁹⁷. This task was devised to assess generalization capabilities of pretrained models on classifying diverse disease categories and tissue types. Using in-house BWH slides, we defined a dataset that comprises 5,564 WSIs from 43 cancer types further subdivided into 108 OncoTree codes, with at least 20 WSIs per OncoTree code. The dataset forms the basis of two tasks that vary in diagnostic difficulty: 1) 43-class cancer type classification (OT-43) and 2) 108-class OncoTree code classification (OT-108). Due to small support sizes for several OncoTree codes in OT-108, all ABMIL models were trained using train-test folds and without early stopping. For training and evaluation, we approximately label-stratified the dataset into 71:29 train-test folds (3944:1620 slides) using the same folds for OT-43 and OT-108, with a 15 slides used per OncoTree code in the test set and a minimum of 5 slides used per OncoTree code in the training set. The hierarchical classification of the coarse- and fine-grained task is reported in **Extended Data Table 4**. We note that slides in the training fold of OT-43 and OT-108 were included in OP-1K and OP-22K pretraining, with the test set held out from these pretraining sources (following practices in ImageNet).

Due to storage limitations in repeatedly extracting features for all non-overlapping tissue patches per WSI for all pretrained models (including intermediate checkpoints), we sampled 200 representative patches per WSI for feature extraction. To select these patches, we first extracted ResNet-50_{IN} features followed by clustering¹⁸⁵,

employed previously in other works such as WSISA¹⁸⁶, DeepAttnMISL^{187,188}, and others¹⁸⁹. We note that these works are inspired by visual bag-of-words (vBOW)^{190,191}, which has been adapted to pathology for formulating high-resolution ROIs and WSIs as smaller but representative collections of tissue patches via clustering applied to deep features^{192,193}, with downstream applications such as MIL^{186–189} and retrieval^{89,133}. For all pretrained encoders, we extract features from the same sampled collection of patches. Though additional computational steps were taken to derive these sampled patches, we note that this does not fall under transductive inference, as the entire test set (all WSI samples) is never made visible to any learning component (clustering is fitted per WSI, with “samples” defined at the slide-level instead of the patch-level). To validate that this approach has comparable performance using features for all tissue patches per WSI, we compare the performance of sampled versus full features of UNI, CTransPath, REMEDIS, and ResNet-50_{IN}, which we also report in **Extended Data Table 10 and 12**. We observe not only marginal performance decrease when using sampled features (maximum decrease of -0.9% in top-1 accuracy, -0.007 in AUROC), but also performance increases for many models. For REMEDIS, we observe that the performance of ABMIL models collapses when using full features, with top-1 accuracy performances of 4.0% and 11.8% respectively on OT-43 and OT-108 (compared to 59.3% and 41.2% respectively with sampled features). We hypothesize that these performance increases are due to the difficult nature of OT-43 and OT-108, with patch sampling reducing the input data complexity for ABMIL (*e.g.* - instead of finding diagnostically-relevant features in a bag of 10,000+ patches, only 200 representative patches are considered).

Breast Metastasis Detection based on CAMELYON16 (2 classes)⁹: The breast metastasis detection task from the Cancer Metastases in Lymph Nodes Challenge 2016 (CAMELYON16) consists of 400 H&E FFPE histopathology WSIs of sentinel lymph node from Radboud University Medical Center and the University Medical Center Utrecht for metastasis detection. We removed 1 slide from the test set that was mislabeled, resulting in 399 slides (239 normal, 160 metastasis). For training and evaluation, we used the official train-test folds, and label-stratified the training set into 90:10 train-validation, resulting in 61:7:32 train-validation-test folds (243:27:129 slides).

NSCLC Subtyping based on TCGA and CPTAC (LUAD vs. LUSC, 2 classes)^{99,107,108}: The NSCLC subtyping task consists of non-small cell lung cancer (NSCLC) H&E FFPE diagnostic histopathology WSIs sourced from TCGA and CPTAC for classifying two subtypes: primary lung adenocarcinoma (LUAD) and lung squamous cell carcinoma (LUSC) cases. For quality control, in TCGA, we excluded slides with missing or incorrect metadata, which resulted in 1,041 slides (529 LUAD and 512 LUSC). In CPTAC, we excluded slides that were frozen tissue, non-tumor tissue or were not labeled as having acceptable tumor segments, which resulted in 1,091 slides (578 LUAD and 513 LUSC). For training and evaluation, we label-stratified the TCGA-NSCLC cohort into 80:10:10 train-validation-test folds (848:97:98 slides), with external evaluation using the held-out CPTAC cohort.

RCC Subtyping based on DHMC (CCRCC vs. PRCC vs. CHRCC vs. ROCY vs. Benign, 5 classes)¹¹³:

The RCC subtyping task consists of 563 renal cell carcinoma (RCC) H&E FFPE diagnostic histopathology WSIs (485 resections and 78 biopsies) from the Dartmouth-Hitchcock Medical Center (DHMC) for classifying five subtypes: primary clear cell renal cell carcinoma (CCRCC, 344 slides), papillary renal cell carcinoma (PRCC, 101 slides) and chromophobe renal cell carcinoma (CHRCC, 23 slides), renal oncocytomas (ROCY, 66 slides), and benign cases (29 slides). For training and evaluation of both tasks, we used a modified configuration of the train-validation-test folds with a 70:4:26 ratio (393:23:147 slides), with 8 CHRCC cases moved from the test to train fold due to CHRCC being absent in the train fold.

RCC Subtyping based on TCGA, DHMC, and CPTAC (CCRCC vs. PRCC vs. CHRCC, 3 classes)^{109–113}:

The RCC subtyping task consists of 1,794 renal cell carcinoma (RCC) H&E FFPE diagnostic histopathology WSIs from TCGA, DHMC, CPTAC for classifying three subtypes: primary clear cell renal cell carcinoma (CCRCC), papillary renal cell carcinoma (PRCC) and chromophobe renal cell carcinoma (CHRCC). For quality control, in TCGA, we excluded slides with missing low-resolution downsamples, which resulted in 922 slides (519 CCRCC, 294 PRCC and 109 CHRCC). In DHMC, we filtered out oncocytomas in the previously-described DHMC-Kidney cohort, which resulted in 468 slides (344 CCRCC, 101 PRCC and 23 CHRCC). In CPTAC, we excluded slides that were frozen tissue, non-tumor tissue or were not labeled as having acceptable tumor segments, which resulted in 404 slides (404 CCRCC). For training and evaluation, we label-stratified the TCGA-NSCLC cohort into 80:10:10 train-validation-test folds (736:89:97 slides), with external evaluation on the held-out DHMC and CPTAC cohorts. As CPTAC only includes CCRCC cases, we combined DHMC and CPTAC into a single evaluation cohort.

CRC Screening based on HunCRC (4 classes)¹²⁵: The CRC screening task consists of 200 H&E FFPE diagnostic histopathology WSIs of colorectal biopsies from the Hungarian Colorectal Cancer Screening (HunCRC) dataset from Semmelweis University. Within this dataset, we defined a 4-way coarse-grained subtyping task into the categories of negative (10 slides), non-neoplastic lesion (38 slides), CRC (46 slides), and adenoma (106 slides), in which the ground-truth label was set by the study’s pathologist. For training and evaluation, we label-stratified the HunCRC slide dataset into 50:25:25 train-validation-test folds (158:21:21 slides).

BRCA Coarse- and Fine-Grained Subtyping based on BRACS (3 and 7 classes)¹¹⁴: The BRCA coarse- and fine-grained subtyping tasks consists of 547 breast carcinoma H&E slides from 187 patients sourced from the Breast Carcinoma Subtyping (BRCA) task sourced from IRCCS Fondazione Pascale, The Institute for High Performance Computing and Networking (ICAR) of National Research Council (CNR), and IBM Research-Zurich. Within this dataset, we defined a 3-way coarse-grained subtyping task using the ”benign tumor”, ”atypical tumor”, and ”malignant tumor” labels. Furthermore, we define a 7-way fine-grained subtyping task that subtypes benign tumors further as ”normal”, ”pathological benign”, ”usual ductal hyperplasia”, atypical

tumors as "flat epithelial atypia" and "atypical ductal hyperplasia", and malignant tumors as "ductal carcinoma in situ" and "invasive carcinoma". The hierarchical classification of the coarse- and fine-grained tasks is reported in **Extended Data Table 5**. For training and evaluation of both tasks, we used the official train-validation-test folds with a 72:12:16 ratio (395:65:87 slides), using the same folds for both coarse- and fine-grained tasks.

Glioma *IDH1* Mutation Prediction and Histomolecular Subtyping based on TCGA and EBRAINS (2 and 5 classes)^{115-117,194}: The glioma *IDH1* mutation prediction and histomolecular subtyping tasks consists of 1,996 H&E FFPE diagnostic histopathology WSIs from glioblastoma, astrocytoma, and oligodendroglioma cases with molecular status from the TCGA and the EBRAINS Digital Tumor Atlas. We first defined a 5-way glioma histomolecular subtyping task with the following labels: *IDH1*-mutant Astrocytomas (257 slides), *IDH1*-mutant Glioblastomas (93 slides), *IDH1*-mutant and 1p/19q -codeleted Oligodendrogliomas (408 slides), *IDH1*-wildtype Glioblastomas (1094 slides), and *IDH1*-wildtype Astrocytomas (144 slides). Additionally, we defined a simpler 2-way task that only predicts *IDH1* status: *IDH1*-wildtype (1,238 slides) and *IDH1*-mutant (756 slides). The hierarchical classification of the coarse- and fine-grained tasks is reported in **Extended Data Table 6**. For training and evaluation of both tasks, we approximately label-stratified the TCGA-GBMLGG dataset into a train-validation-test fold with a 47:22:31 ratio (525:243:355 slides), with external evaluation using the held-out EBrains cohort (873 slides), using the same folds for both coarse- and fine-grained tasks.

Brain Tumor Coarse- and Fine-Grained Subtyping based on EBRAINS (12 and 30 classes)^{115,194}: The brain tumor coarse- and fine-grained subtyping tasks consists of 2,319 H&E FFPE diagnostic histopathology WSIs from the EBRAINS Digital Tumor Atlas sourced from the University of Vienna. With an original dataset size of 3,114 slides, we defined a 30-way fine-grained brain tumor subtyping task limited to diagnostic labels that have at least 30 slides: 1) *IDH1*-wildtype Glioblastoma (474 slides), 2) Pilocytic Astrocytoma (173 slides), 3) Meningothelial Meningioma (104 slides), 4) Pituitary Adenoma (99 slides), 5) *IDH1*-mutant and 1p/19q codeleted Anaplastic Oligodendroglioma (91 slides), 6) Ganglioglioma (88 slides), 7) Haemangioblastoma (88 slides), 8) Adamantinomatous Craniopharyngioma (85 slides), 9) *IDH1*-mutant and 1p/19q codeleted Oligodendroglioma (85 slides), 10) Atypical Meningioma (83 slides), 11) Schwannoma (81 slides), 12) *IDH1*-mutant Diffuse Astrocytoma (70 slides), 13) Transitional Meningioma (68 slides), 14) Diffuse Large B-Cell Lymphoma of the CNS (59 slides), 15) Gliosarcoma (59 slides), 16) Fibrous Meningioma (57 slides), 17) Anaplastic Ependymoma (50 slides), 18) *IDH1*-wildtype Anaplastic Astrocytoma (47 slides), 19) Metastatic Tumours (47 slides), 20) *IDH1*-mutant Anaplastic Astrocytoma (47 slides), 21) Ependymoma (46 slides), 22) Anaplastic Meningioma (46 slides), 23) Secretory Meningioma (41 slides), 24) Lipoma (38 slides), 25) Haemangiopericytoma (34 slides), 26) *IDH1*-mutant Glioblastoma (34 slides), 27) Non-WNT/Non-SHH Medulloblastoma (32 slides), 28) Langerhans Cell Histiocytosis (32 slides), 29) Angiomatous Meningioma (31 slides), and 30) Haemangioma (30 slides). From the same 2,319 slide dataset in the fine-grained task, we also defined a 12-

way coarse-grained brain tumor subtyping task that groups the above labels into the following categories: 1) Adult-Type Diffuse Gliomas (837 slides), 2) Meningiomas (430 slides), 3) Mesenchymal, Non-Meningothelial Tumours Involving The CNS (190 slides), 4) Tumours Of The Sellar Region (184 slides), 5) Circumscribed Astrocytic Gliomas (173 slides), 6) Ependymal Tumours (96 slides), 7) Haematolymphoid Tumours Involving The CNS (91 slides), 8) Glioneuronal And Neuronal Tumours (88 slides), 9) Cranial And Paraspinal Nerve Tumours (81 slides), 10) Paediatric-Type Diffuse Low-Grade Gliomas (70 slides), 11) Metastatic Tumours (47 slides) and 12) Embryonal Tumors (32 slides). The hierarchical classification of the coarse- and fine-grained tasks is reported in **Extended Data Table 7**. For training and evaluation of both tasks, we approximately label-stratified the dataset into a train-validation-test fold with a 50:25:25 ratio (1,151:595:573 slides), using the same folds for both coarse- and fine-grained tasks.

ISUP Grading based on PANDA (6 classes)^{12,21}: The ISUP grading task is derived from the Prostate Cancer Grade Assessment (PANDA) challenge, which comprises 10,616 prostate cancer core needle biopsies of prostate cancer sourced from the Radboud University Medical Center and the Karolinska Institute. Each slide is assigned an ISUP score that defines prostate cancer grade (6-class grading task). For quality control, we follow prior work¹⁹⁵ in excluding slides which were erroneously annotated⁵ or had noisy labels⁶, which resulted in 9,555 slides (2,603 G0, 2,399 G1, 1,209 G2, 1,118 G3, 1,124 G4, 1,102 G5). For training and evaluation, we label-stratified PANDA into 80:10:10 train-validation-test folds (7,647:954:954 slides).

Endomyocardial Assessment based on in-house BWH data (2 classes)¹⁰⁵: BWH-EMB dataset consists of 5,021 H&E FFPE histopathology WSIs from 1,688 in-house endomyocardial biopsies (EMB) collected from Brigham & Women’s Hospital for cellular-mediated allograft rejection (ACR) (2,444 ACR, 2,577 others). For training and evaluation, we case- and label-stratified the dataset into 70:10:20 train-validation-test folds (3,547:484:900 slides).

CRC Tissue Classification based on CRC-100K (9 classes)^{124,196}: The CRC tissue classification task is based on the CRC-100K dataset, which consists of 107,180 224×224 ROIs at 0.5 mpp annotated and extracted from H&E FFPE diagnostic histopathology WSIs of 136 colorectal adenocarcinoma samples from the National Center for Tumor Diseases (NCT) biobank and the University Medical Center Mannheim (UMM) pathology archive. ROIs were labeled with the following 9 classes: adipose (11,745 ROIs), background (11,413 ROIs), debris (11,851 ROIs), lymphocyte (12,191 ROIs), mucus (9,931 ROIs), smooth muscle (14,128 ROIs), normal colon mucosa (9,504 ROIs), cancer-associated stroma (10,867 ROIs) and colorectal adenocarcinoma epithelium (15,550 ROIs). For training and evaluation, we used the official case-stratified train-test folds (100,000:7,180 ROIs), with the training fold constructed from 100,000 ROIs (86 WSIs) from the NCT biobank and UMM pathology archive (referred to as “NCT-CRC-HE-100K”), and test fold constructed from

⁵www.kaggle.com/competitions/prostate-cancer-grade-assessment/discussion/169230

⁶www.kaggle.com/competitions/prostate-cancer-grade-assessment/discussion/169230

7,180 ROIs (50 WSIs) from the NCT biobank (referred to as “CRC-VAL-HE-7K”). Additionally, we use the version of NCT-CRC-HE-100K without stain normalization. We use the same folds for linear probe, KNN, and SimpleShot evaluation. We evaluate this dataset on ROIs of 224×224 image resolution at 0.5 mpp.

CRC Tissue Classification based on HunCRC (9 classes)¹²⁵: The CRC tissue classification task is based on the HunCRC dataset, which consists of 101,398 512×512 ROIs at 0.48 mpp, annotated and extracted from the same 200 H&E FFPE diagnostic histopathology WSIs of colorectal biopsies also described in the slide-level task. ROIs were labeled with the following 9 classes: adenocarcinoma (4,315 ROIs), high-grade dysplasia (2,281 ROIs), low-grade dysplasia (55,787 ROIs), inflammation (763 ROIs), tumor necrosis (365 ROIs), suspicious For invasion (570 ROIs), resection edge (534 ROIs), technical artifacts (3,470 ROIs) and normal (31,323 ROIs). For training and evaluation, we case-stratified and approximately label-stratified the dataset into train-test folds (151:49 cases, 76,753:22,655 ROIs), which was used in linear probe, KNN, and SimpleShot evaluation. We evaluate this dataset on resized ROIs of 448×448 image resolution at 0.55 mpp.

BRCA Subtyping based on BACH (4 classes)¹²⁹: The BRCA subtyping task is based on the Breast Carcinoma Subtyping (BACH) dataset, which consists of 400 2048×1536 image ROIs at 0.42 mpp, annotated and extracted from H&E FFPE diagnostic histopathology WSIs of breast carcinoma samples from the ICIAR 2018 grand challenge on breast cancer histology images. ROIs were labeled with the following 4 classes: normal (100 ROIs), benign (100 ROIs), *in situ* carcinoma (100 ROIs) and invasive carcinoma (100 ROIs). For training and evaluation, we label-stratified the dataset into train-test folds (320:80 ROIs), which was used in linear probe, KNN, and SimpleShot evaluation. Additionally, we evaluate this dataset across the following center-cropped and resized image resolutions: 224×224 at 2.88 mpp, 448×448 at 1.44 mpp, 896×896 at 0.72 mpp, and 1344×1344 at 0.48 mpp.

CCRCC Tissue Classification based on TCGA and HEL (3 classes)^{127,197}: The CCRCC tissue classification task consists of 52,713 256×256 and 300×300 ROIs at approximately 0.25 mpp, annotated and extracted from H&E FFPE diagnostic histopathology WSIs of clear cell renal cell carcinoma (CCRCC) samples from TCGA (502 samples) and Helsinki University Hospital (HEL) (64 samples). ROIs were labeled with the following 6 classes: cancer (13,057 ROIs), normal (8,652 ROIs), stroma (5,460 ROIs), red blood cells (996 ROIs), empty background (16,026 ROIs), and other textures (8,522 ROIs). For this task, we considered only the cancer, normal, and stroma labels due to label imbalance when stratifying by data source and ambiguities of the “other” category. We used ROIs from TCGA (21,095 ROIs) and Helsinki (6,074 ROIs) as train and test cohorts respectively (train-test fold with 21,095:6,074 ratio), which we used for linear probe, KNN, and SimpleShot evaluation. We evaluate this dataset on resized ROIs of 224×224 image resolution at approximately 0.29 mpp.

PRAD Tissue Classification based on AGGC (5 classes)¹²⁸: The PRAD tissue classification task is based on

the Automated Gleason Grading Challenge 2022 (AGGC) from the National University Hospital and Agency of Science, Technology and Research (A*STAR) in Singapore. It comprises 221 WSIs obtained from prostatectomies (105 training, 45 testing) and biopsies (37 training, 16 testing) digitized using an Akoya Biosciences scanner at $20\times$ magnification at 0.5 mpp. Each slide includes partial pixel-level annotations delineating different Gleason patterns and stromal regions. From the original WSIs and annotations, we built a ROI dataset consisting of 1,125,640 non-overlapping 256×256 pixel ROIs (train-test fold with 780,619:345,021 ratio), which we used for linear probe, KNN, and SimpleShot evaluation. ROIs with more than one Gleason pattern were assigned the most aggressive grade. We evaluate this dataset on resized ROIs of 224×224 image resolution at approximately 0.57 mpp.

ESCA Tissue Classification based on UKK, WNS, TCGA, and CHA (11 classes)^{130,198}: The ESCA tissue classification task consists of 367,229 256×256 ROIs at 0.78 mpp, annotated and extracted from 320 H&E FFPE diagnostic histopathology WSIs of oesophageal adenocarcinoma and adenocarcinoma of the oesophago-gastric junction from four sources: University Hospital Cologne (UKK, 22 slides), Landesklinikum Wiener Neustadt (WNS, 62 slides), TCGA (22 slides), and the University Hospital Berlin—Charité (CHA, 214 slides). ROIs were labeled with the following 11 classes: adventitia (71,131 ROIs), lamina propria mucosae (2,173 ROIs), muscularis mucosae (2,951 ROIs), muscularis propria (83,358 ROIs), regression tissue (56,490 ROIs), mucosa gastric (44,416 ROIs), mucosa oesophagus (18,561 ROIs), submucosa (22,117 ROIs), submucosal glands (1,516 ROIs), tumor (63,863 ROIs) and ulceration (753 ROIs). For training and evaluation, we combined UKK, WNS and TCGA into a combined training cohort (189,142 ROIs) and used CHA as a test cohort (178,187 ROIs) with a train-test fold ratio of 51:49, which we then used for linear probe, KNN, and SimpleShot evaluation. We evaluate this dataset on resized ROIs of 224×224 image resolution at approximately 0.89 mpp.

CRC Polyp Classification based on UniToPatho (6 classes)^{126,199}: The CRC polyp classification task is based on the UniToPatho dataset, which consists of 9,536 1812×1812 image ROIs at 0.44 mpp, annotated and extracted from 292 H&E FFPE diagnostic histopathology WSIs of colorectal polyp samples from University of Turin. ROIs were labeled with the following 6 classes: normal (950 ROIs), hyperplastic polyp (545 ROIs), tubular adenoma with high-grade dysplasia (454 ROIs), tubular adenoma with low-grade dysplasia (3,618 ROIs), tubulo-villous adenoma with high-grade dysplasia (916 ROIs), and tubulo-villous adenoma with low-grade dysplasia (2,186 ROIs). For training and evaluation, we used the official train-test folds (6,270:2,399 ROIs). We evaluate this dataset across the following resized image resolutions: 224×224 at 3.60 mpp, 448×448 at 1.80 mpp, 896×896 at 0.90 mpp, and 1792×1792 at 0.45 mpp.

CRC MSI prediction based on TCGA CRC-MSI^{3,200}: The CRC MSI prediction task is based on the “TCGA CRC-MSI” dataset, which consists of 51,918 512×512 ROIs at approximately 0.5 mpp, extracted from H&E FFPE diagnostic histopathology WSIs of colorectal adenocarcinoma samples annotated and extracted from

TCGA. ROIs were labeled with the following 2 classes according to the patient-level label of the sample: microsatellite instable (15,002 ROIs) and microsatellite stable (36,916 ROIs). For training and evaluation, we used the official train-test folds (19,557:32,361 ROIs), which was used in linear probe, KNN, and SimpleShot evaluation. We evaluate this dataset on resized ROIs of 448×448 image resolution at 0.57 mpp. To mitigate potential biases from site-specific H&E staining variability in TCGA, we used Macenko normalization¹³² to normalize all ROIs.

Pan-Cancer Tissue Classification based on TCGA Uniform Tumor (32 classes)^{88,201}: The pan-cancer tissue classification task is based on the “TCGA Uniform Tumor” dataset, which consists of 271,170 256×256 ROIs at around 0.5 mpp of 32 cancer types annotated and extracted from 8,736 H&E FFPE diagnostic histopathology WSIs in TCGA. Images were labeled with the following 32 classes: 1) Adrenocortical Carcinoma (4,980 ROIs), 2) Bladder Urothelial Carcinoma (9,990 ROIs), 3) Brain Lower Grade Glioma (23,530 ROIs), 4) Breast Invasive Carcinoma (23,690 ROIs), 5) Cervical Squamous Cell Carcinoma And Endocervical Adenocarcinoma (6,270 ROIs), 6) Cholangiocarcinoma (900 ROIs), 7) Colon Adenocarcinoma (8,150 ROIs), 8) Esophageal Carcinoma (3,380 ROIs), 9) Glioblastoma Multiforme (23,740 ROIs), 10) Head And Neck Squamous Cell Carcinoma (11,790 ROIs), 11) Kidney Chromophobe (2,460 ROIs), 12) Kidney Renal Clear Cell Carcinoma (11650 ROIs), 13) Kidney Renal Papillary Cell Carcinoma (6,790 ROIs), 14) Liver Hepatocellular Carcinoma (8,370 ROIs), 15) Lung Adenocarcinoma (16,460 ROIs), 16) Lung Squamous Cell Carcinoma (16,560 ROIs), 17) Lymphoid Neoplasm Diffuse Large B-Cell Lymphoma (840 ROIs), 18) Mesothelioma (2,090 ROIs), 19) Ovarian Serous Cystadenocarcinoma (2,520 ROIs), 20) Pancreatic Adenocarcinoma (4090 ROIs), 21) Pheochromocytoma and Paraganglioma (1,350 ROIs), 22) Prostate Adenocarcinoma (9810 ROIs), 23) Rectum Adenocarcinoma (1,880 ROIs), 24) Sarcoma (13,480 ROIs), 25) Skin Cutaneous Melanoma (10,060 ROIs), 26) Stomach Adenocarcinoma (9,670 ROIs), 27) Testicular Germ Cell Tumors (6,010 ROIs), 28) Thymoma (3,600 ROIs), 29) Thyroid Carcinoma (11,360 ROIs), 30) Uterine Carcinosarcoma (2,120 ROIs), 31) Uterine Corpus Endometrial Carcinoma (12,480 ROIs), and 32) Uveal Melanoma (1,640 ROIs). For training and evaluation, we case-stratified and approximately label-stratified the dataset into train-test folds (216,350:55,360 ROIs), which was used in linear probe, KNN, and SimpleShot evaluation. We evaluate this dataset on resized ROIs of 224×224 image resolution at approximately 0.57 mpp. To mitigate potential biases from site-specific H&E staining variability in TCGA¹³¹, we used Macenko normalization¹³² to normalize all ROIs.

Pan-Cancer Tumor-Immune Lymphocyte (TIL) Detection based on TCGA-TILS (2 classes)^{83,87,202,203}: The TIL detection task is based on the “TCGA-TILS” dataset, which consists of 304,097 100×100 pixels histopathology ROIs at approximately 0.5 mpp, annotated and extracted from H&E FFPE diagnostic histopathology WSIs in TCGA. ROIs were labeled with the following 2 classes: TIL-positive (if there are at least two TILs present in the image, 54,910 ROIs) and TIL-negative (249,187 ROIs). For training and evalu-

ation, we used the official train-validation-test folds (209,221:38,601:56,275 ROIs) and combine the train and validation folds into a single training fold. We bilinearly upsampled all images to 224×224 at 0.20 mpp for equivalent comparisons with CTransPath. To mitigate potential biases from site-specific H&E staining variability in TCGA, we used Macenko normalization¹³² to normalize all ROIs.

Pan-Cancer Cell Type Segmentation based on SegPath (8 cell types treated as individual tasks¹³⁵: The cell type segmentation tasks are derived from the SegPath dataset, which consists of 158,687 984×984 ROIs at 0.22 mpp, annotated and extracted from H&E FFPE diagnostic histopathology WSIs of eight major cell types in cancer tissue from University of Tokyo Hospital. Immunofluorescence and DAPI nuclear staining was performed on ROIs and used as image masks for the following classes: endothelium (10,647 ROIs), epithelium (26,509 ROIs), leukocyte (24,805 ROIs), lymphocyte (12,273 ROIs), myeloid cell (14,135 ROIs), plasma cell (13,231 ROIs), red blood cell (25,909 ROIs), and smooth muscle (31,178 ROIs). Each cell type in the dataset forms an independent tissue segmentation task with two classes, tissue/cell region and non-tissue/cell region. For training and evaluation, we used the official train-validation-test split with an approximate 80:10:10 ratio.

Computing hardware and software

We used Python (version 3.8.13) and PyTorch²⁰⁴ (version 2.0.0, CUDA 11.7) (pytorch.org) for all experiments and analyses in the study (unless specified), which can be replicated using open-source libraries as outlined below. To train UNI via DINOv2, we modify the vision transformer implementation maintained by the open-source Timm library (version 0.9.2) from Hugging Face (huggingface.co) for the encoder backbone and use the original DINOv2 self-supervised learning algorithm (github.com/facebookresearch/dinov2) for pretraining, which utilized 4×8 80GB NVIDIA A100 GPU nodes configured for multi-GPU, multi-node training using distributed data-parallel (DDP). All other computation for downstream experiments were conducted on single 24GB NVIDIA 3090 GPUs. All WSI processing was supported by OpenSlide (version 4.3.1), openslide-python (version 1.2.0), and CLAM (github.com/mahmoodlab/CLAM). We use Scikit-learn¹⁶⁹ (version 1.2.1) for its implementation of K-Nearest Neighbors, and the logistic regression implementation and SimpleShot implementation provided by the LGSSL codebase (github.com/mbanani/lgssl). Implementations of other visual pretrained encoders benchmarked in the study are found at the following links: ResNet-50 with ImageNet Transfer (github.com/mahmoodlab/CLAM), CTransPath (github.com/Xiyue-Wang/TransPath), and REMEDIS (github.com/google-research/medical-ai-research-foundations). We note that REMEDIS requires fulfillment of a data use agreement, which can be accessed and submitted at the PhysioNet website (physionet.org/content/medical-ai-research-foundation)^{205,206}. For multi-head attention visualization, we used the visualisation tools provided by the HIPT codebase (github.com/mahmoodlab/HIPT). For training weakly-supervised ABMIL models, we adapted the training scaffold code from the CLAM codebase (github.com/mahmoodlab/CLAM). For training semantic segmentation, we use the original Mask2Former implementation (github.com/facebookresearch/Mask2Former) which is based on detectron2²⁰⁷ (version 0.6), and required the

following older packages for compatibility: Python (version 3.8) and PyTorch (version 1.9.0, CUDA 11.1). For adding ViT-Adapter to UNI, we adapt its original implementation (github.com/czczup/ViT-Adapter) in detectron2 to train it using Mask2Former. Pillow (version 9.3.0) and OpenCV-python were used to perform basic image processing tasks. Matplotlib (version 3.7.1) and Seaborn (version 0.12.2) were used to create plots and figures. Usage of other miscellaneous Python libraries is listed in the **Reporting Summary**.

Data availability

TCGA and CPTAC data consisting of whole slide images and labels can be accessed through the NIH genomic data commons⁷ and proteomics data commons⁸ respectively. GTEx data added to the pretraining dataset can be accessed through the GTEx portal⁹. CPTAC data consisting of All publicly-available datasets analyzed in this work can be accessed in their respective data portals: CRC-100K¹⁰, HunCRC patches¹¹, HunCRC slides¹², BACH¹³, TCGA CRC-MSI¹⁴, CCRCC Tissue Classification¹⁵, TCGA-TILs¹⁶, TCGA Uniform¹⁷, UniToPatho¹⁸, ESCA¹⁹, EBRAINS²⁰, DHMC Kidney²¹, BRACS²², PANDA²³, SegPath²⁴, and AGGC²⁵. TCGA, CPTAC, HunCRC, TCGA-TILs can also be accessed using the The Cancer Imaging Archive²⁰⁸. We note that data from AGGC was obtained from a public grand challenge (of the same name²⁶) with a pending publication¹²⁸, with permission granted to present results on this dataset from the challenge organizers. Works that use AGGC should also obtain permission from the challenge organizers, and acknowledge the pending publication of the grand challenge. Image patches used for pretraining and BWH-EMB WSIs were curated with in-house data. Following institution policies, all requests for data collected or curated in-house will be evaluated accordingly on a case-by-case basis to determine whether the data requested and the use case is compliant with intellectual property or patient privacy obligations.

Code availability

The authors will release code for performing downstream evaluation using the pretrained encoder of this work

⁷portal.gdc.cancer.gov

⁸proteomic.datacommons.cancer.gov

⁹gtexportal.org

¹⁰zenodo.org/record/1214456

¹¹doi.org/10.6084/m9.figshare.c.5927795.v1

¹²doi.org/10.7937/tcia.9cjh-0127

¹³iciar2018-challenge.grand-challenge.org/Dataset/

¹⁴zenodo.org/record/3832231

¹⁵zenodo.org/record/7898308

¹⁶zenodo.org/record/6604094

¹⁷zenodo.org/record/5889558

¹⁸zenodo.org/record/4643645

¹⁹zenodo.org/record/7548828

²⁰doi.org/10.25493/WQ48-ZGX

²¹bmirids.github.io/KidneyCancer/

²²bracs.icar.cnr.it/

²³panda.grand-challenge.org/data/

²⁴zenodo.org/record/7412731

²⁵zenodo.org/record/6460100

²⁶<https://aggc22.grand-challenge.org>

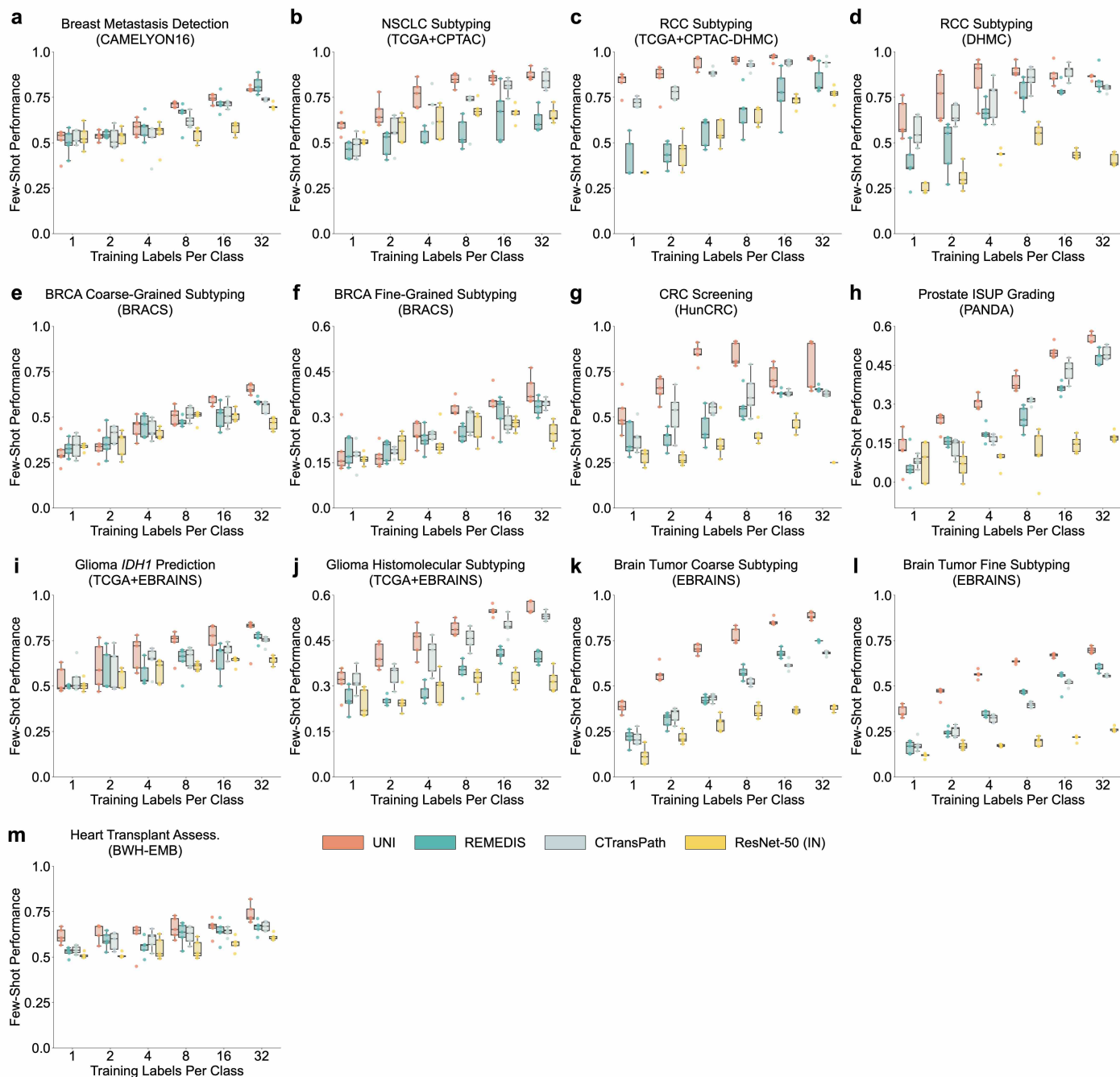
upon publication. Since our model utilizes proprietary patient data for pretraining, the model weights may be requested and granted institutional permission for access on a case-by-case basis. All methods and software packages used in the study have been documented and explained in ways accessible to the broader scientific audience.

Author contributions

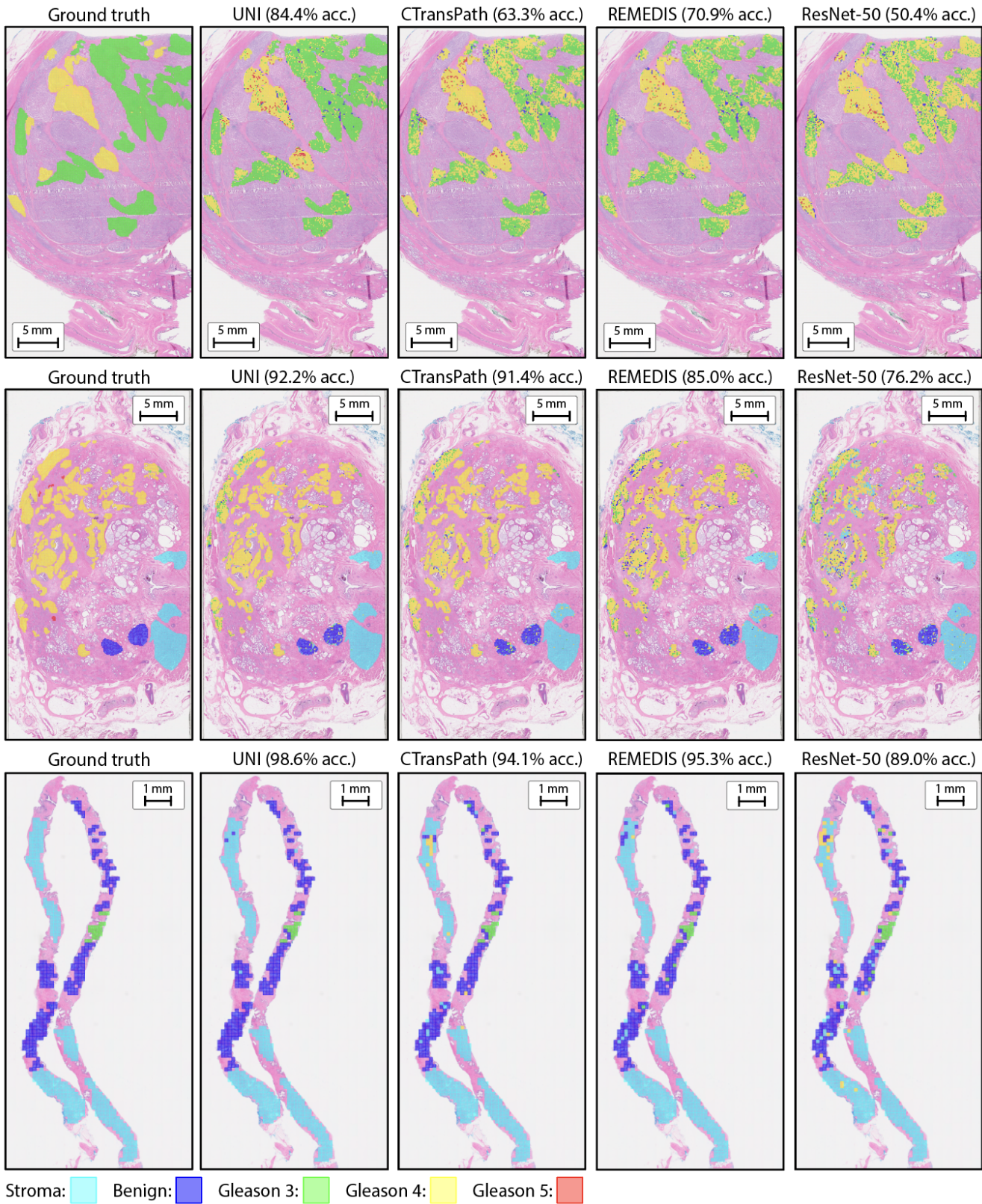
R.J.C., F.M., T.D., M.Y.L., D.F.K.W. conceived the study and designed the experiments. R.J.C., L.P.L., D.F.K.W., J.J.W., T.D., M.Y.L., G.J., A.V., A.H.S., B.C., A.Z., D.S., M.S., L.O., S.S. collected the data for self-supervised learning. R.J.C., T.D., M.Y.L. performed model development for self-supervised learning. R.J.C., M.Y.L., T.D., B.C., G.J. organized the datasets and codebases for all downstream tasks regarding ROI classification, ROI segmentation, and slide classification. R.J.C., M.Y.L., G.J. performed experimental analysis regarding ROI classification. T.D., M.Y.L., R.J.C., L.W., W.W. performed experimental analysis regarding ROI segmentation. R.J.C., T.D., B.C., D.S., M.S., M.W., A.Z., L.W. performed experimental analysis regarding slide classification. R.J.C., T.D., M.Y.L., D.F.K.W., G.J., A.H.S., L.P.L., G.G., F.M. interpreted the experimental results and provided feedback on the study. R.J.C., T.D., M.Y.L., D.F.K.W., F.M. prepared the manuscript with input from all co-authors. F.M. supervised the research.

Acknowledgements

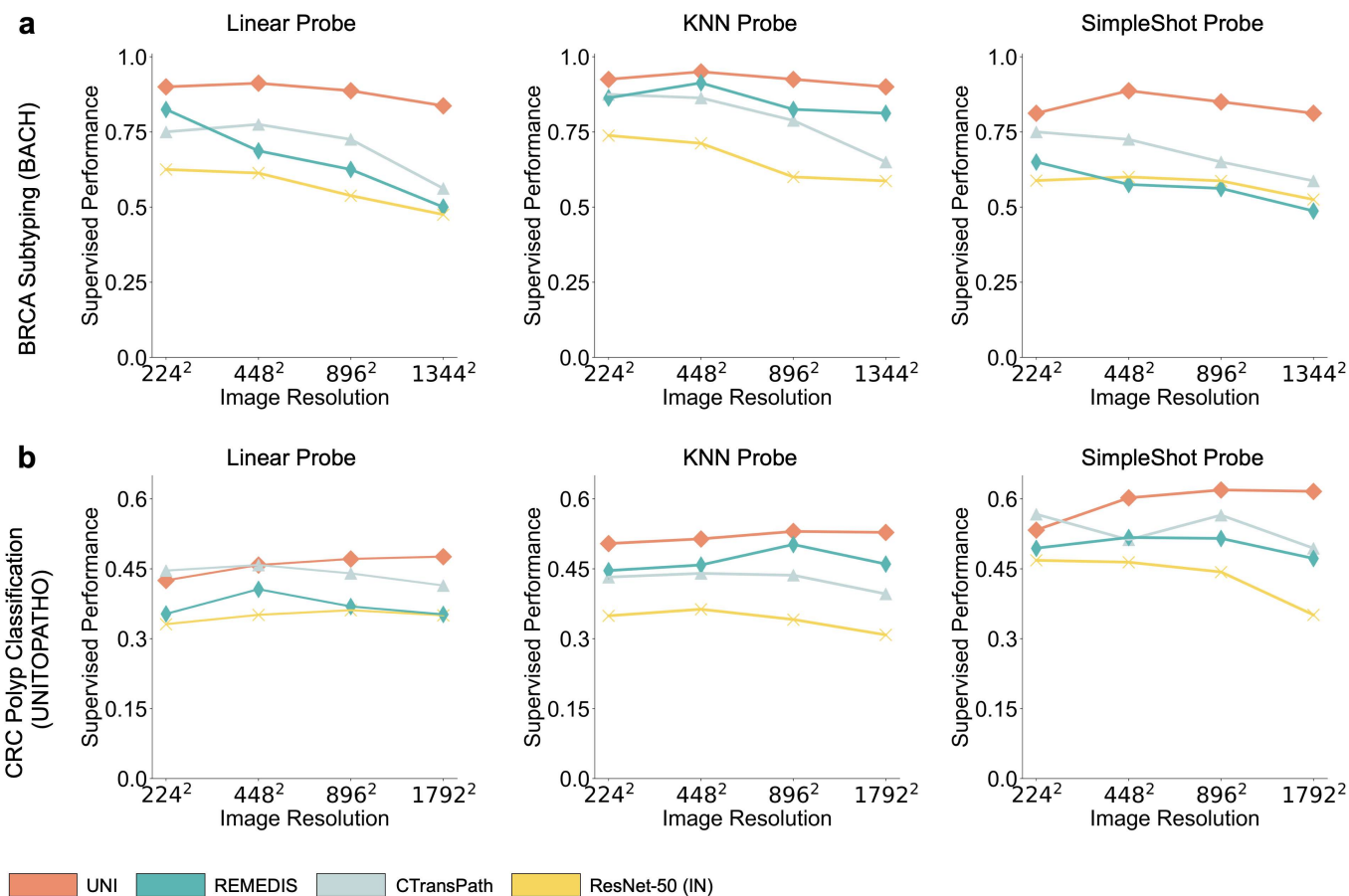
This work was supported in part by the BWH & MGH Pathology, BWH president's fund, Massachusetts Life Sciences Center, NIGMS R35GM138216 (F.M.), and the BWH President's Scholar fund (G.G.). M.Y.L. was also supported by the Siebel Scholars program. R.J.C., D.S., and S.S. were also supported by the NSF Graduate Fellowship. L.O. was also supported by the German Academic Exchange (DAAD) Fellowship. We thank Timothy Janicki at BWH, and Richard Kenny and the system administration staff at the MGB Enterprise Research Infrastructure & Services (ERIS) Research Computing Core, for their dedicated support in providing and maintaining access to NVIDIA A100 computing resources. We thank the Computational Digital Pathology Lab and Bioinformatics Institute at the Agency of Science, Technology and Research (A*STAR) and the AGGC 2022 challenge committee for making the AGGC dataset available for research prior to the official challenge paper being published. We thank Negin Vatanian, Mathangi Thiagarajan, Brenda Fevrier-Sullivan and Justin Kirby at the National Institutes of Health (NIH) for navigating access to whole-slide imaging data in CPTAC.



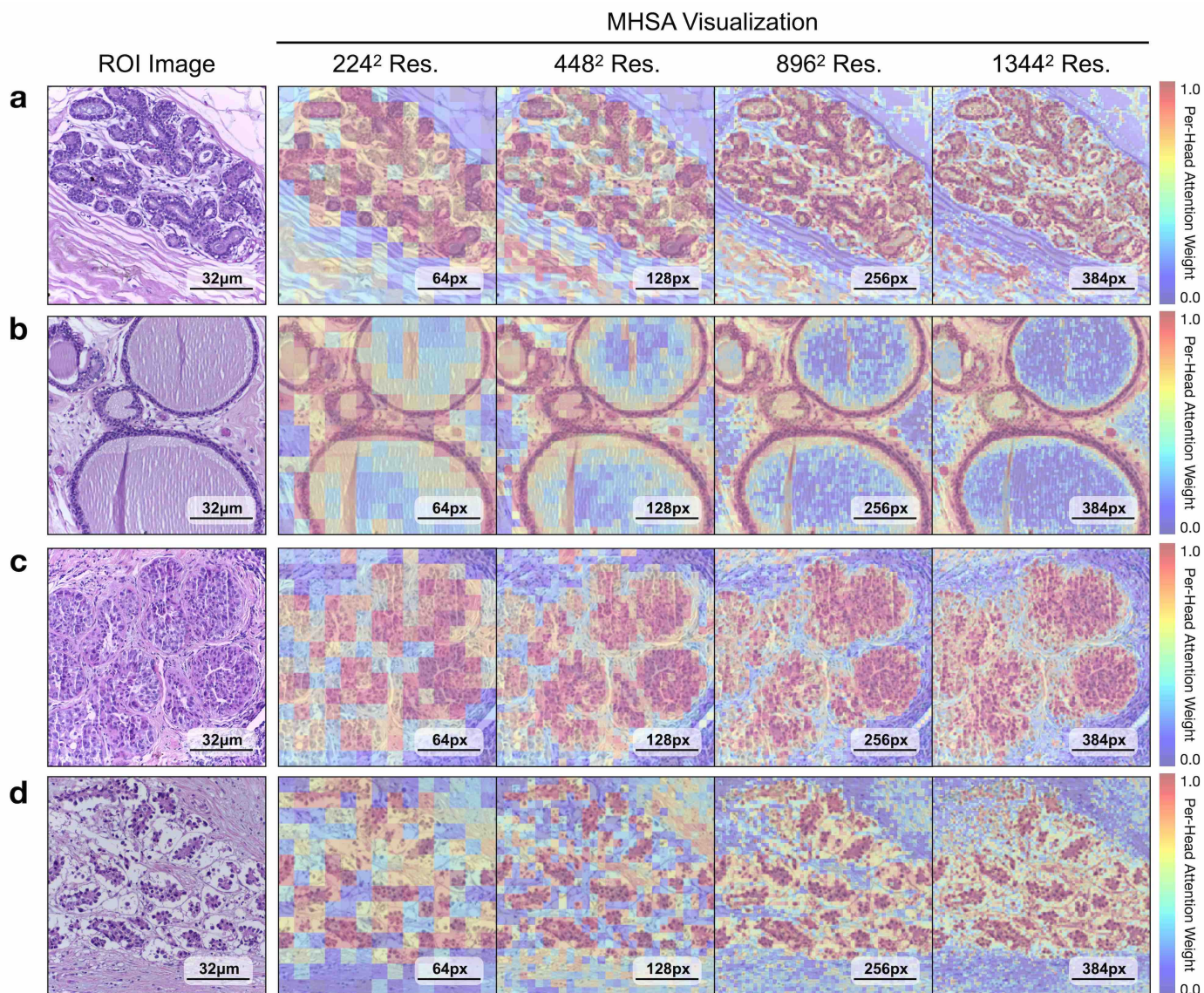
Extended Data Figure 1: **Few-Shot slide classification.** To study the label efficiency of UNI in slide classification, we compare UNI with other pretrained encoders on: **a.** breast metastasis detection in CAMELYON16, **b.** NSCLC subtyping in CPTAC (trained on TCGA) **c.** RCC subtyping in CPTAC-DHMC (trained on TCGA), **d.** RCC subtyping in DHMC, **e.** BRCA coarse-grained subtyping in BRACS, **f.** BRCA fine-grained subtyping in BRACS, **g.** CRC screening in HunCRC, **h.** Prostate ISUP Grading in PANDA, **i.** glioma IDH1 prediction in EBRAINS (trained on TCGA), **j.** glioma histomolecular subtyping in EBRAINS (trained on TCGA), **k.** brain tumor coarse-grained subtyping in EBRAINS, **l.** brain tumor fine-grained subtyping in EBRAINS, and **m.** heart transplant assessment in BWH-EMB. The performance is measured across different few-shot settings with $K \in \{1, 2, 4, 8, 16, 32\}$ training examples used per class. Boxes indicate quartile values of model performance ($n = 5$ runs) and whiskers extend to data points within $1.5 \times$ the interquartile range. Overall, we observe that UNI consistently demonstrates superior label efficiency over other baselines.



Extended Data Figure 2: **Comparing supervised performance on PRAD tissue classification in AGCC.** Qualitative illustrations comparing UNI to CTransPath, REMEDIS, and ResNet-50 (IN) via KNN probing on PRAD tissue classification in AGCC. UNI achieves better accuracy (acc.) on all three examples. The reported results are based on partial annotations (left-most panel) provided by pathologists.

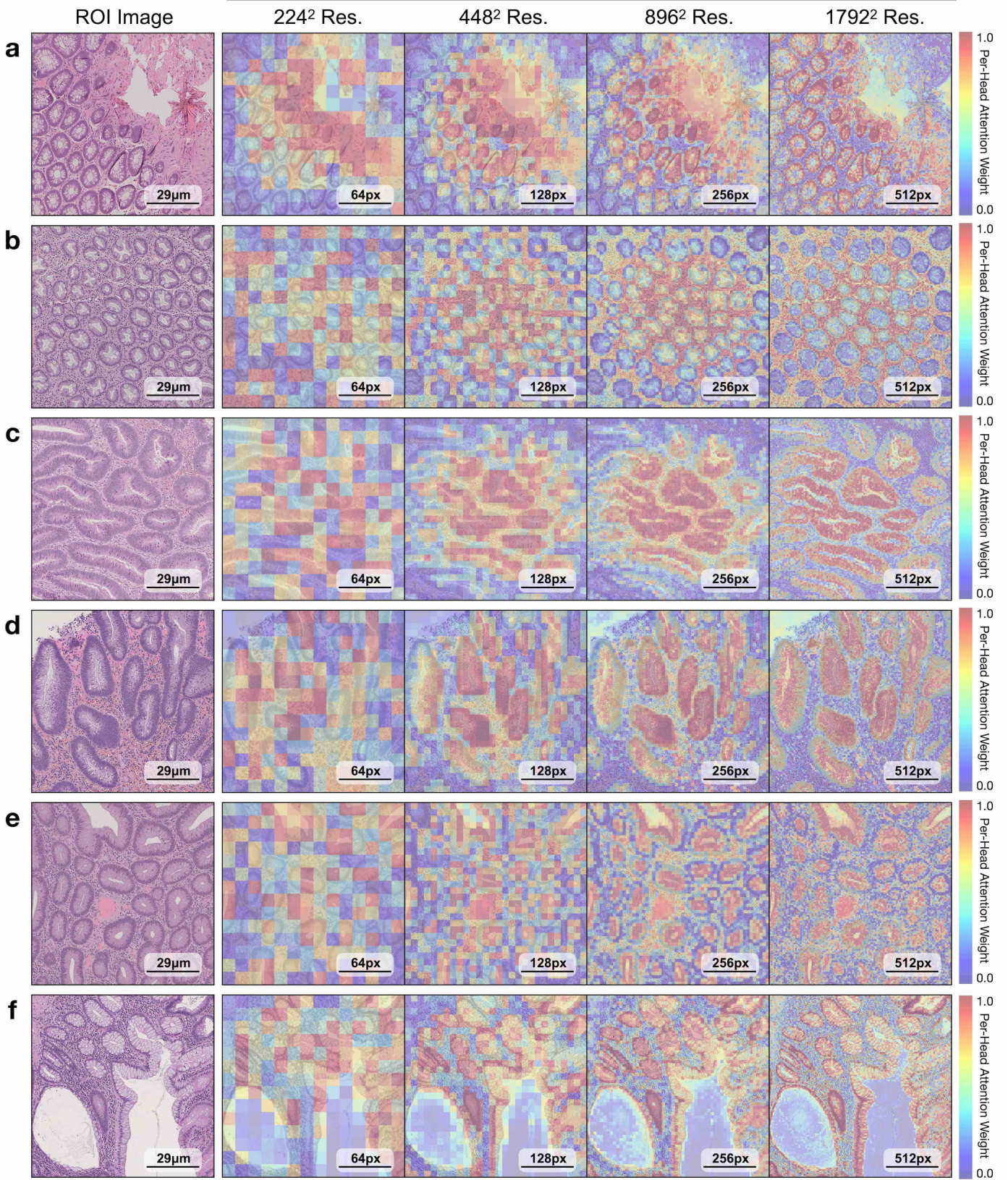


Extended Data Figure 3: **ROI classification across different image resolutions.** To assess how image resolution affects performance, we compare UNI and other baselines on various resized and center-cropped ROIs for **a.** BRCA subtyping and **b.** CRC polyp classification tasks. The original image size is 2048×1536 and 1812×1812 pixels, respectively. All models are evaluated on linear, SimpleShot (1-NN), and KNN (20-NN) probe settings. UNI consistently outperforms all baselines across all resolutions. The performance metrics are further provided in **Extended Data Table 31, 32, 37, 38.**

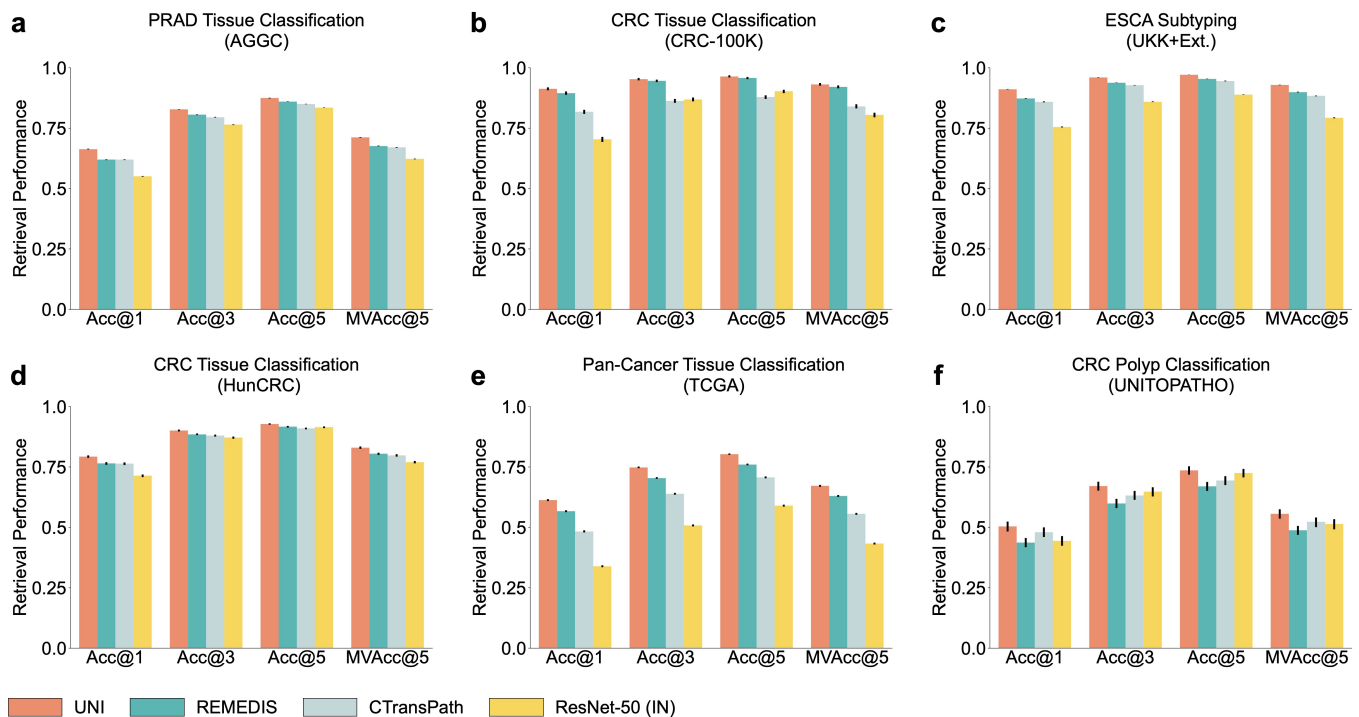


Extended Data Figure 4: **Multi-head self-attention (MHSA) heatmap visualization of UNI across different image resolutions in BRCA Subtyping in BACH.** Each colored square represents a 16×16 patch token encoded by UNI, with heatmap color corresponding to the attention weight of that patch token to the global [CLS] token of the penultimate layer in UNI. We show MHSA visualizations for resized and center-cropped ROIs at 224^2 , 448^2 , 896^2 , 1344^2 resolutions for the normal (a), benign (b), in situ (c), and invasive (d) classes in BACH. In each, the leftmost image is the original H&E ROI and the right four images are the MHSA visualizations. For comparative purposes, we resize all images within the figure to have the same dimension, but note that at higher resolutions, each colored square has an original image resolution of 16×16 pixels at 0.42 mpp. As the resolution increases, the heatmaps demonstrate increasing and increasingly fine-grained attention focused on epithelial structures, with relatively lower attention on stroma or other background, neither of which are contributory to the diagnoses in these ROIs.

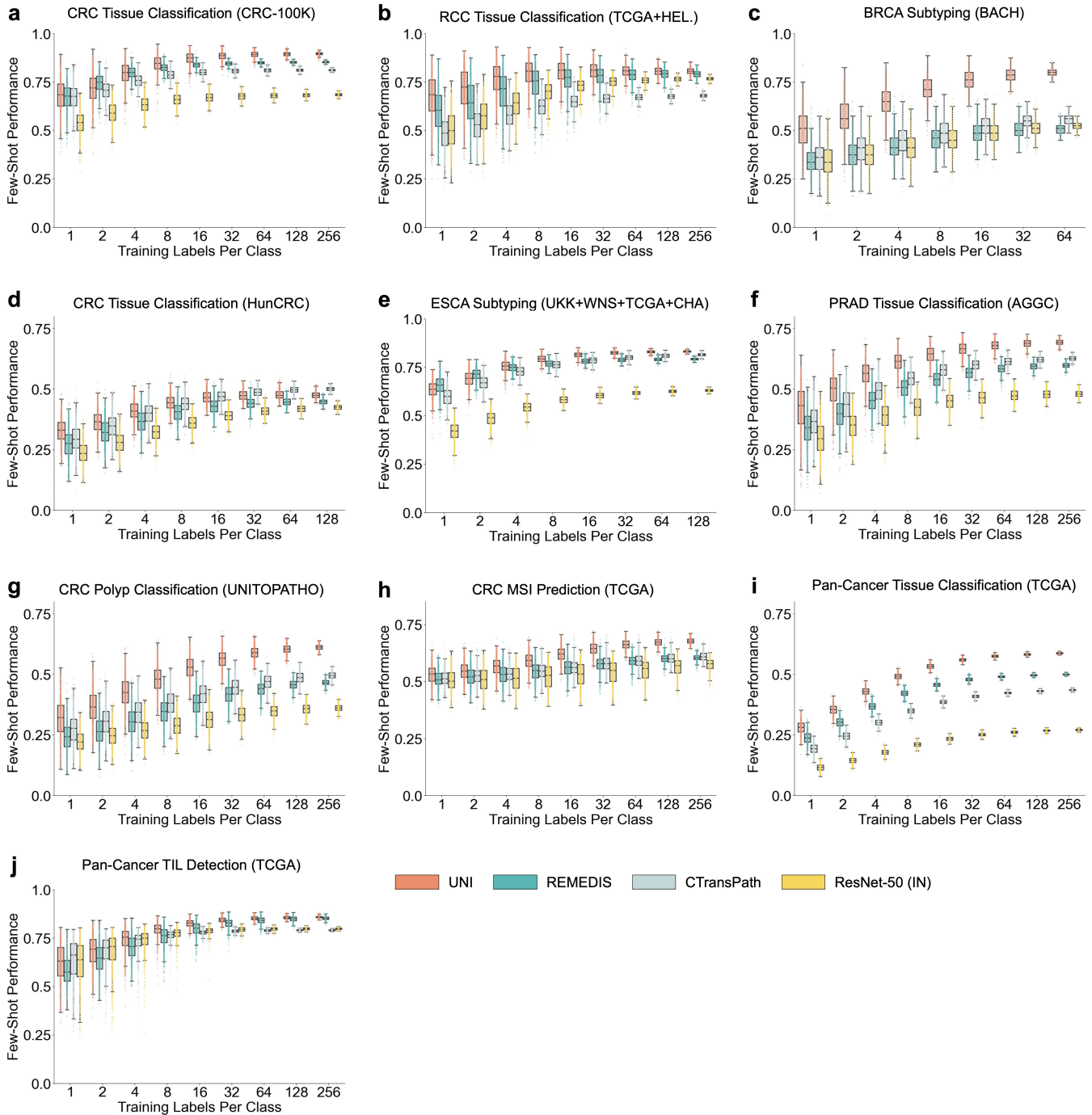
MHSA Visualization



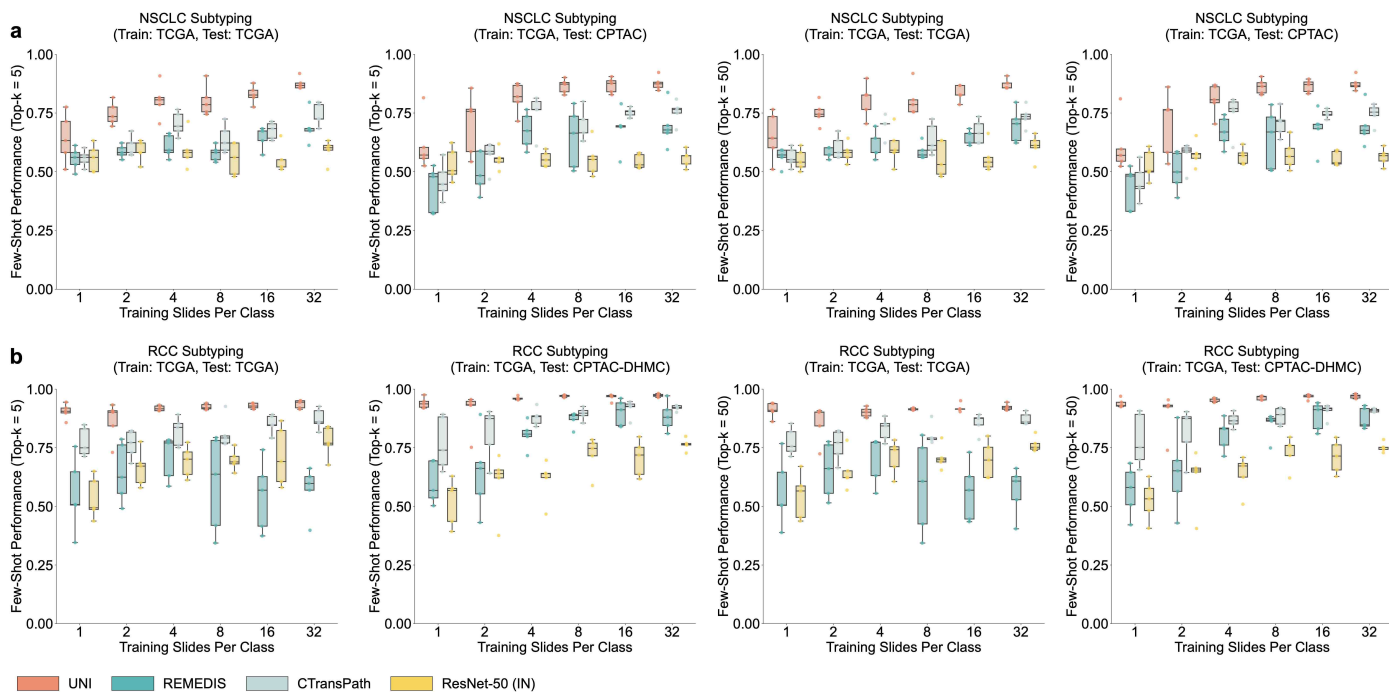
Extended Data Figure 5: **Multi-head self-attention (MHSA) heatmap visualization of UNI across different image resolutions for CRC polyp classification in UniToPatho.** Each colored square represents a 16×16 patch token encoded by UNI, with heatmap color corresponding to the attention weight of that patch token to the global [CLS] token of the penultimate layer in UNI. We show MHSA visualizations for resized and center-cropped ROIs at 224^2 , 448^2 , 896^2 , 1792^2 resolutions for normal tissue (**a**), a hyperplastic polyp (**b**), a tubular adenoma with low-grade dysplasia (**c**), a tubular adenoma with high-grade dysplasia (**d**), a tubulovillous adenoma with high-grade dysplasia (**e**), and a tubulovillous adenoma with low-grade dysplasia (**f**). In each, the leftmost image is the original H&E ROI and the right four images are the MHSA visualizations. For comparative purposes, we resize all images within the figure to have the same dimension, but note that at higher resolutions, each colored square has an original image resolution of 16×16 pixels at 0.48 mpp. As resolution increases, the heatmaps demonstrate increasing and increasingly fine-grained attention focused on the crypts, in all cases except the hyperplastic polyp in **b**, focusing on areas a pathologist would use to make the diagnosis. The high attention on the stroma in the case of the hyperplastic polyp in **b** is interesting and may be evidence that hyperplastic polyps can have a different character of stroma than other colorectal polyps.



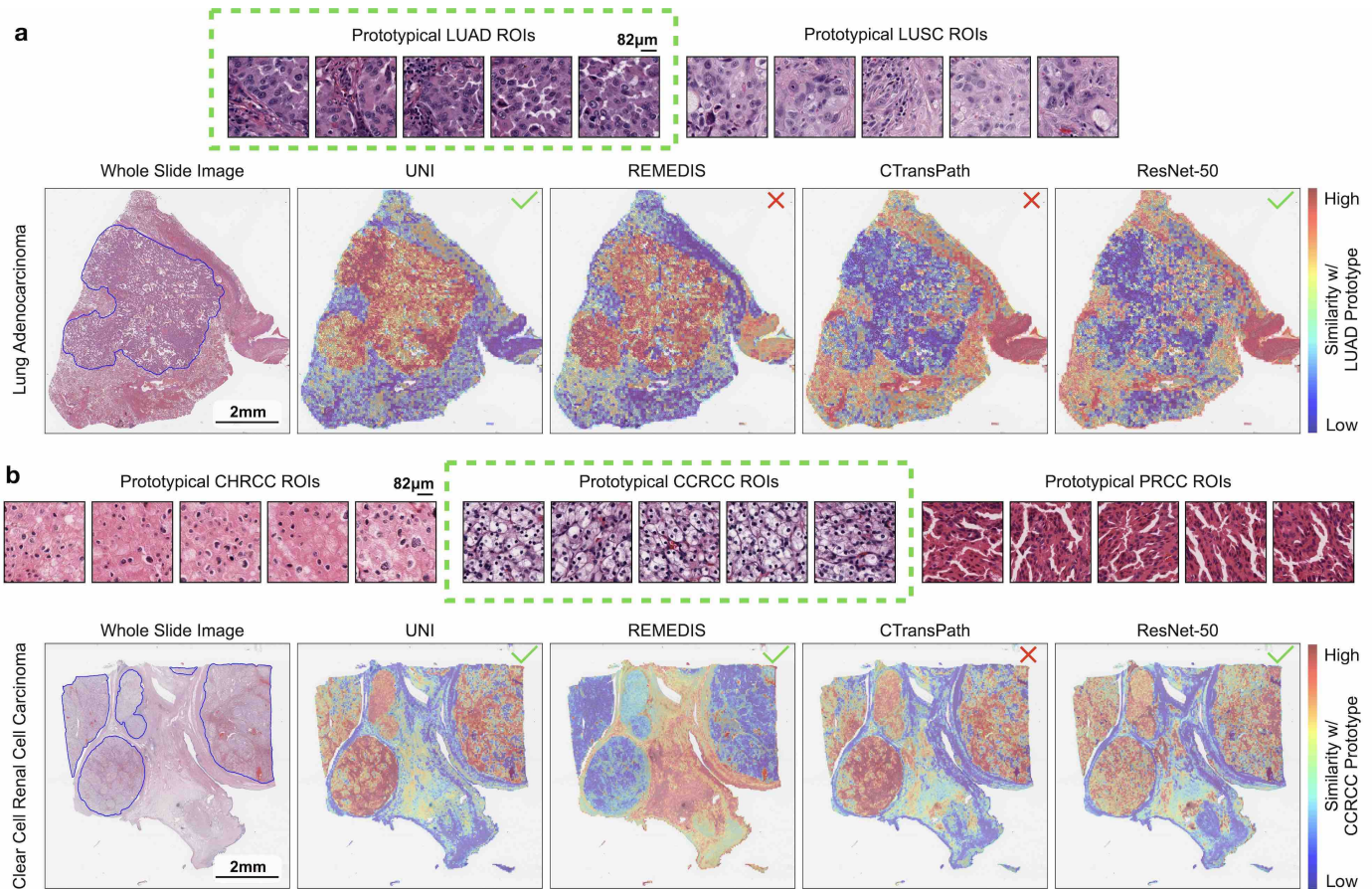
Extended Data Figure 6: **ROI retrieval.** We evaluate content-based image retrieval for ROI-level classes with at least 5 classes, for **a.** PRAD tissue classification in AGGC, **b.** CRC tissue classification in CRC-100K, **c.** ESCA subtyping on CHA (trained on UKK, WNS and TCGA), **d.** CRC tissue classification in HunCRC, **e.** pan-cancer tissue classification in TCGA, and **f.** CRC polyp classification in UniToPatho. UNI consistently outperforming all pretrained encoders. Detailed performance metrics are further provided in **Extended Data Table 47-52.**



Extended Data Figure 7: **Few-shot ROI classification using class prototypes.** Similar to slide-level classification, we also assess the label-efficiency of UNI on ROI-level tasks, and observe superior label efficiency of UNI on most tasks except CRC tissue classification on HunCRC. We evaluate all pretrained encoders using the non-parametric SimpleShot framework for **a**. CRC tissue classification in CRC-100K, **b**. RCC tissue classification on HEL (trained on TCGA), **c**. BRCA subtyping in BACH, **d**. CRC tissue classification in HunCRC, **e**. ESCA subtyping on CHA (UKK+WNS+TCGA), **f**. PRAD tissue classification in AGGC, **g**. CRC polyp classification in UniToPatho, **h**. CRC MSI prediction in TCGA, **i**. pan-cancer tissue classification in TCGA, and **j**. pan-cancer TIL detection in TCGA.



Extended Data Figure 8: **Few-shot slide classification using class prototypes.** We adapt the SimpleShot framework for slide-level classification, called “MI-SimpleShot”. ROI class prototypes are constructed by averaging the pre-extracted ROI features for each class using the “TCGA Uniform Tumor” dataset, which we use as “prompts” for assigning the slide-level label. We assess and compare the few-shot performance of all pretrained encoders on NSCLC subtyping (**a**) and RCC subtyping task (**b**), using the same runs ($n=5$) in the few-shot setting for ABMIL for $K \in \{1, 2, 4, 8, 16, 32\}$ training examples used per class. We compare performance of top-5 and top-50 pooling of nearest patches in the test set, as well as show performance on both the internal test fold in TCGA and external cohort. Boxes indicate quartile values of model performance ($n = 5$ runs) and whiskers extend to data points within $1.5 \times$ the interquartile range. We also compare. Overall, we observe that the formed prototypes by UNI can be used to classify slides based on the MI-SimpleShot framework. **a.** On NSCLC subtyping, we observe that 2-shot and 4-shot performance from UNI outperforms the 32-shot performance of all other models. **b.** On RCC subtyping, 1-shot performance of UNI also outperforms the 32-shot performance of other models. We also observe that MI-SimpleShot can be combined with other pretrained encoders as well, but generally require more annotated ROIs for creating prototypes.



Extended Data Figure 9: **Comparing 1-shot similarity heatmaps of pretrained encoders with class prototype.** We compare the similarity heatmaps of all pretrained encoders using annotated ROIs from a single slide per class for forming class prototypes in MI-SimpleShot (with top-5 pooling) on NSCLC subtyping (**a**) and RCC subtyping task (**b**), with **top** visualizing example ROIs used for each class, and **bottom** showing similarity heatmaps. Outlined in blue are pathologist annotations of ROIs that match the label of the histology slide. Similarity heatmaps are created with respect to the class prototype of the correct slide label (indicated in green), with a \checkmark indicating a correct prediction and \times indicating incorrect prediction. Note that since the visualizations are created with respect to the ground truth label, the model may retrieve correct patches that match pathologist annotations but still misclassify the slide. **a.** On a LUAD slide, we observe strong agreement of the pathologist’s annotations with retrieved LUAD patches by UNI. Though retrieved patches by REMEDIS also have strong agreement with the pathologist’s annotations, we note that slide was misclassified as LUSC, indicating that the top-5 retrieved patches of the LUSC prototype was higher than that of the LUAD prototype. Vice versa, ResNet-50_{IN} classifies the slide correctly but incorrectly retrieves the correct patches that agree with the pathologist’s annotations, indicating that non-LUAD patches in the slide were more LUAD-like than the pathologist-annotated LUAD patches with respect to the LUAD prototype. The similarity heatmap for CTransPath both misclassified the slide and retrieved incorrect patches. **b.** On a example CCRCC slide, we observe strong agreement of the pathologist’s annotations with retrieved CCRCC patches by UNI. We observe similar mismatch in predicted class label and retrieved patches, in which REMEDIS classifies the slide correctly but retrieves the incorrect patches, and CTransPath misclassifies the slide but retrieves the correct patches.

Major Tissue Type	Num. Slides
Heart	10427
Lung	9846
Kidney	8388
Bowel / Lower GI	8303
Soft Tissue	7863
Brain	7412
Esophagogastric	6705
Endocrine	6138
Female Genital Tract	5796
Lymphatic System	4957
Liver Biliary Tract	4677
Male Genital Tract	4017
Skin	3653
Breast	3364
Bone	2667
Pancreas	2328
Head & Neck	1555
Peritoneum	1210
Bladder	1059
Eye	61
Total	100426

Extended Data Table 1: **Major Tissue Type Distribution of Mass-100K.** Mass-100K is a pretraining dataset that consists of 100,130,900 tissue patches from 100,426 diagnostic whole-slide images (WSIs) across 20 major tissue types collected from the Massachusetts General Hospital (MGH), Brigham & Women’s Hospital (BWH) and the Genotype-Tissue Expression (GTEx) consortium.

Major Tissue Type	Num. Slides
Heart	4
Lung	3044
Kidney	435
Bowel / Lower GI	2002
Soft Tissue	1275
Brain	1607
Esophagogastric	882
Endocrine	549
Female Genital Tract	1834
Lymphatic System	1342
Liver Biliary Tract	1403
Male Genital Tract	587
Skin	627
Breast	1366
Bone	301
Pancreas	543
Head & Neck	532
Peritoneum	389
Bladder	568
Eye	21
Total	21444

Extended Data Table 2: **Major Tissue Type Distribution of Mass-22K.** Mass-22K is a subset of Mass-100K, which contains 16,059,454 histology image patches sampled from 21,444 WSIs across 20 major tissue types with cancerous tissue collected from Massachusetts General Hospital (MGH) and Brigham & Women’s Hospital (BWH).

Major Tissue Type	Num. Slides
Heart	3
Lung	136
Kidney	43
Bowel / Lower GI	55
Soft Tissue	176
Brain	219
Esophagogastric	32
Endocrine	34
Female Genital Tract	187
Lymphatic System	134
Liver Biliary Tract	75
Male Genital Tract	33
Skin	43
Breast	42
Bone	32
Pancreas	28
Head & Neck	61
Peritoneum	34
Bladder	30
Eye	7
Total	1404

Extended Data Table 3: **Major Tissue Type Distribution of Mass-1K.** Mass-1K is a subset of Mass-22K, which contains 1,064,615 histology image patches sampled from 1,404 WSIs across 20 major tissue types with cancerous tissue collected from Massachusetts General Hospital (MGH) and Brigham & Women’s Hospital (BWH).

Cancer Type	OncoTree Code	Num. Slides
Adrenocortical Carcinoma	ACC	51 (31:20)
Ampullary Cancer	AMPCA	42 (16:26)
Anal Cancer	ANSC	65 (51:14)
Appendiceal Cancer	MAAP	40 (23:17)
Bladder Cancer	BLAD	28 (8:20)
	BLCA	65 (20:45)
	UTUC	65 (22:43)
Bone Cancer	CHS	32 (10:22)
	ES	48 (17:31)
	OS	54 (26:28)
Breast Cancer	IDC	65 (56:9)
	ILC	65 (65:0)
	MDLC	65 (62:3)
CNS Cancer	ATM	20 (7:13)
	MNG	65 (47:18)
Cervical Cancer	CESC	60 (60:0)
	ECAD	42 (42:0)
Colorectal Cancer	COAD	65 (35:30)
	MACR	35 (14:21)
	READ	65 (31:34)
Embryonal Tumor	MBL	62 (23:39)
Endometrial Cancer	UCCC	23 (23:0)
	UCS	65 (65:0)
	UEC	65 (65:0)
	UMEC	25 (25:0)
	USC	65 (65:0)
Esophagogastric Cancer	ESCA	64 (19:45)
	ESCC	65 (31:34)
	GEJ	65 (17:48)
	SSRCC	28 (15:13)
	STAD	65 (31:34)
Gastroint. Neuroend. Tumor	GINET	65 (33:32)
Gastroint. Stromal Tumor	GIST	65 (33:32)
Germ Cell Tumor	MGCT	36 (0:36)
	SEM	63 (0:63)

Cancer Type (Cont.)	OncoTree Code	Num. Slides
Glioma	AASTR	54 (20:34)
	AODG	31 (17:14)
	ASTR	65 (30:35)
	EPM	38 (13:25)
	GBM	65 (33:32)
	HGGNOS	65 (26:39)
	LGGNOS	63 (24:39)
	ODG	58 (28:30)
PAST	35 (18:17)	
Head and Neck Cancer	HNSC	65 (19:46)
Hepatobiliary Cancer	CHOL	65 (26:39)
	GBC	65 (47:18)
	HCC	65 (25:40)
Mature B-Cell Neoplasms	CLLSLL	26 (13:13)
	DLBCLNOS	65 (23:42)
	FL	54 (28:26)
Mature T and NK Neoplasms	MYCF	37 (15:22)
Melanoma	MEL	65 (28:37)
Mesothelioma	PLBMESO	63 (6:57)
	PLEMESO	65 (20:45)
Misc. Neuroepithelial Tumor	PGNG	24 (13:11)
Nerve Sheath Tumor	MPNST	40 (17:23)
	SCHW	38 (23:15)
Non-Small Cell Lung Cancer	ALUCA	30 (20:10)
	LUAD	64 (37:27)
	LUAS	32 (19:13)
	LUCA	64 (52:12)
	LUNE	33 (20:13)
	LUSC	65 (30:35)
	NSCLCPD	65 (30:35)
Ovarian Cancer	CCOV	65 (65:0)
	EOV	65 (65:0)
	HGSOC	65 (65:0)
	LGSOC	62 (62:0)
	MOV	33 (33:0)
	MXOV	49 (49:0)
	OCS	42 (42:0)
	SBOV	28 (28:0)
Pancreatic Cancer	PAAD	64 (26:38)
	PANET	65 (31:34)
Peripheral Nervous System	NBL	65 (27:38)
Prostate Cancer	PRAD	65 (0:65)

Cancer Type (Cont.)	OncoTree Code	Num. Slides
Renal Cell Carcinoma	CCRCC	65 (26:39)
	CHRCC	65 (28:37)
	PRCC	65 (22:43)
	ROCY	20 (6:14)
Salivary Gland Cancer	ACYC	33 (21:12)
Sellar Tumor	PTAD	65 (41:24)
Sex Cord Stromal Tumor	GRCT	33 (33:0)
Skin Cancer, Non-Melanoma	CSCC	65 (15:50)
	MCC	65 (23:42)
Small Bowel Cancer	SBC	53 (18:35)
Small Cell Lung Cancer	SCLC	65 (36:29)
Soft Tissue Sarcoma	ANGS	50 (28:22)
	DDL5	65 (28:37)
	DES	41 (27:14)
	ERMS	20 (9:11)
	HEMA	65 (31:34)
	LMS	65 (50:15)
	MFH	60 (24:36)
	MFS	30 (15:15)
	PECOMA	21 (18:3)
	SFT	45 (21:24)
	SYNS	43 (18:25)
WDLS	23 (12:11)	
Thymic Tumor	THYM	24 (14:10)
Thyroid Cancer	THAP	30 (19:11)
	THFO	28 (15:13)
	THME	34 (15:19)
	THPA	65 (39:26)
Uterine Sarcoma	ULMS	51 (51:0)
Vaginal Cancer	VSC	47 (47:0)
Wilms Tumor	WT	63 (29:34)

Extended Data Table 4: **Hierarchical label distribution of the coarse and fine-grained tasks in OncoTree (OT) code cancer classification.** The OT-43 and OT-108 tasks is developed from a dataset comprising 5,564 WSIs from 43 cancer types collected from in-house BWH slides, which are further subdivided into 108 OncoTree codes, with at least 20 WSIs per OncoTree code. The OT-43 task is developed using the first level of the hierarchy (“Cancer Type” column), and the OT-108 task is developed using the second level of the hierarchy (“OncoTree Code” column), with both tasks using the same train-test folds. Gender ratio (female:male) is reported for each OncoTree code.

Cancer Subtype	Cancer Diagnosis	Num. Slides
Benign	Normal	44
	Pathological Benign	147
	Usual Ductal Hyperplasia	74
Atypical	Atypical Ductal Hyperplasia	48
	Flat Epithelial Atypia	41
Malignant	Ductal Carcinoma in Situ	61
	Invasive Carcinoma	132

Extended Data Table 5: **Hierarchical label distribution of BRCA Coarse- and Fine-Grained Subtyping based on BRACS.** The coarse-grained BRCA subtyping task is developed using the first level of the hierarchy (“Cancer Subtype” column), and the fine-grained BRCA subtyping task is developed using the second level of the hierarchy (“Cancer Diagnosis” column), with both tasks using the official train-validation-test folds of the BRACS dataset.

<i>IDH1</i> status	Histomolecular Subtype	Num. Slides
<i>IDH1</i> -mutant	Astrocytoma, <i>IDH1</i> -mutant	257
	Glioblastoma, <i>IDH1</i> -mutant	93
	Oligodendroglioma, <i>IDH1</i> -mutant & 1p/19q codeleted	408
<i>IDH1</i> -wildtype	Astrocytoma, <i>IDH1</i> -wildtype	144
	Glioblastoma, <i>IDH1</i> -wildtype	1094

Extended Data Table 6: **Hierarchical label distribution of Glioma *IDH1* Mutation Prediction and Histomolecular Subtyping based on TCGA and EBRAINS.** The glioma *IDH1* mutation prediction task is developed using the first level of the hierarchy (“*IDH1* status” column), and the glioma histomolecular subtyping task is developed using the second level of the hierarchy (“Histomolecular Subtype” column), with both tasks using same train-validation-test folds created using the TCGA, with external evaluation on the EBRAINS Digital Tumor Atlas.

Cancer Subtype	Cancer Diagnosis	Num. Slides
Adult-type diffuse gliomas	Anaplastic astrocytoma, <i>IDH1</i> -mutant	47
	Anaplastic astrocytoma, <i>IDH1</i> -wildtype	47
	Anaplastic oligodendroglioma, <i>IDH1</i> -mutant & 1p/19q codeleted	91
	Glioblastoma, <i>IDH1</i> -mutant	34
	Glioblastoma, <i>IDH1</i> -wildtype	474
	Gliosarcoma	59
	Oligodendroglioma, <i>IDH1</i> -mutant & 1p/19q codeleted	85
Circumscribed astrocytic gliomas	Pilocytic astrocytoma	173
Cranial and paraspinal nerve tumours	Schwannoma	81
Embryonal Tumors	Medulloblastoma, non-WNT/non-SHH	32
Ependymal Tumours	Anaplastic ependymoma	50
	Ependymoma	46
Glioneuronal and neuronal tumours	Ganglioglioma	88
Haematolymphoid tumours involving the CNS	Diffuse large B-cell lymphoma of the CNS	59
	Langerhans cell histiocytosis	32
Meningiomas	Anaplastic meningioma	46
	Angiomatous meningioma	31
	Atypical meningioma	83
	Fibrous meningioma	57
	Meningothelial meningioma	104
	Secretory meningioma	41
	Transitional meningioma	68
Mesenchymal, non-meningothelial tumours involving the CNS	Haemangioblastoma	88
	Haemangioma	30
	Haemangiopericytoma	34
	Lipoma	38
Metastatic tumours	Metastatic tumours	47
Paediatric-type diffuse low-grade gliomas	Diffuse astrocytoma, <i>IDH1</i> -mutant	70
Tumours of the sellar region	Adamantinomatous craniopharyngioma	85
	Pituitary adenoma	99

Extended Data Table 7: **Hierarchical label distribution of brain tumor coarse- and fine-grained subtyping based on EBRAINS.** The coarse-grained brain tumor subtyping task is developed using the first level of the hierarchy (“Cancer Subtype” column), and the fine-grained brain tumor subtyping task is developed using the second level of the hierarchy (“Cancer Diagnosis” column), with both tasks using same train-validation-test folds created using the EBRAINS Digital Tumor Atlas.

Hyper-parameter	Value
Layers	24
Heads	16
Patch size	16
FFN layer	MLP
Head activation	GELU
Embedding dimension	1024
Stochastic dropout rate	0.1
Global crop scale	0.48, 1.0
Global crop number & size	2, 224
Local crop scale	0.16, 0.48
Local crop number & size	8, 96
Max masking ratio	0.5
Min masking ratio	0.1
Gradient clipping max norm	3.0
Normalize last layer	✓
Shared head	✗
AdamW β	(0.9, 0.999)
Batch size	3072
Freeze last layer iterations	1250
Warmup iterations	12500
Warmup teacher temperature iterations	37500
High-resolution finetuning iterations	12500
Max Iterations	125000
Learning rate schedule	Cosine
Learning rate (start)	0
Learning rate (post warmup)	2e-3
Learning rate (final)	1e-6
Teacher temperature (start)	0.04
Teacher temperature (final)	0.4
Teacher momentum (start)	0.992
Teacher momentum (final)	1.000
Weight decay (start)	0.04
Weight decay (end)	0.4
Automatic mixed precision	FP16

Extended Data Table 8: **DINOv2 hyperparameters used in UNI pretraining.** $4 \times 80\text{GB}$ NVIDIA A100 GPUs were used for training. Batch size refers to the total batch size across GPUs.

Hyperparameter	Value
Batch size	1
Weight decay	1e-5
AdamW β	(0.9, 0.999)
Peak learning rate	1e-4
Learning rate schedule	Cosine
Epochs	20

Extended Data Table 9: **Hyperparameters used in slide-level supervised classification.** Single 24GB NVIDIA GeForce RTX 3090 GPUs were used for each ABMIL model using weakly-supervised learning and slide-level labels.

Encoder	Full?	Top-1 ACC	Top-3 ACC	Top-5 ACC	Weighted F1	AUROC
ResNet-50 _{IN}	✓	0.336 (0.312-0.359)	0.557 (0.531-0.581)	0.674 (0.651-0.697)	0.274 (0.251-0.297)	0.869 (0.858-0.879)
CTransPath	✓	0.578 (0.554-0.602)	0.796 (0.777-0.815)	0.876 (0.859-0.891)	0.562 (0.536-0.586)	0.957 (0.950-0.963)
REMEDIS	✓	0.040 (0.030-0.049)	0.157 (0.138-0.175)	0.204 (0.185-0.224)	0.012 (0.007-0.019)	0.727 (0.716-0.736)
UNI	✓	0.720 (0.698-0.741)	0.890 (0.874-0.906)	0.935 (0.924-0.947)	0.719 (0.695-0.741)	0.976 (0.972-0.981)
ResNet-50 _{IN}	✗	0.327 (0.304-0.349)	0.552 (0.527-0.576)	0.657 (0.633-0.680)	0.258 (0.236-0.280)	0.862 (0.850-0.873)
CTransPath	✗	0.569 (0.546-0.592)	0.793 (0.773-0.812)	0.874 (0.858-0.890)	0.555 (0.530-0.578)	0.956 (0.949-0.962)
REMEDIS	✗	0.593 (0.570-0.617)	0.802 (0.783-0.822)	0.875 (0.859-0.890)	0.592 (0.567-0.615)	0.954 (0.946-0.961)
UNI	✗	0.731 (0.709-0.752)	0.894 (0.879-0.910)	0.938 (0.926-0.949)	0.729 (0.706-0.750)	0.976 (0.971-0.981)

Extended Data Table 10: **Weakly-supervised 43-class cancer type classification (OT-43) based on in-house BWH data (43 classes).** Pre-extracted patch features of each encoder with ABMIL were trained and evaluated on curated train-test folds (3944:1620), with test performance ($n = 1620$ slides) reported using top-1, top-3, and top-5 accuracy, weighted F1 score, and AUROC. We report results for both extracted features using all tissue patches per WSI, as well as extracted features from 200 representative tissue patches per WSI (described in **Online Methods**). Best performing model for each metric is bolded. 95% CI is included in parentheses.

Data	Iter.	Top-1 ACC	Top-3 ACC	Top-5 ACC	Weighted F1	AUROC
Mass-1K	50K	0.640 (0.616-0.662)	0.843 (0.825-0.860)	0.908 (0.894-0.922)	0.638 (0.612-0.659)	0.968 (0.962-0.973)
Mass-1K	75K	0.646 (0.622-0.669)	0.838 (0.820-0.856)	0.898 (0.883-0.912)	0.644 (0.619-0.667)	0.965 (0.959-0.971)
Mass-1K	100K	0.649 (0.625-0.672)	0.847 (0.829-0.863)	0.905 (0.890-0.919)	0.649 (0.624-0.671)	0.964 (0.957-0.970)
Mass-1K	125K	0.652 (0.628-0.676)	0.835 (0.816-0.852)	0.895 (0.880-0.910)	0.653 (0.627-0.676)	0.962 (0.955-0.968)
Mass-22K	50K	0.707 (0.685-0.730)	0.887 (0.870-0.902)	0.930 (0.918-0.943)	0.704 (0.680-0.728)	0.974 (0.968-0.979)
Mass-22K	75K	0.708 (0.684-0.730)	0.881 (0.865-0.896)	0.930 (0.917-0.941)	0.707 (0.682-0.728)	0.972 (0.967-0.977)
Mass-22K	100K	0.708 (0.686-0.730)	0.888 (0.873-0.904)	0.938 (0.925-0.949)	0.705 (0.682-0.726)	0.973 (0.967-0.978)
Mass-22K	125K	0.694 (0.673-0.716)	0.891 (0.875-0.905)	0.931 (0.918-0.943)	0.692 (0.670-0.714)	0.969 (0.963-0.975)
Mass-100K	50K	0.694 (0.672-0.716)	0.871 (0.855-0.888)	0.927 (0.913-0.939)	0.694 (0.669-0.715)	0.974 (0.968-0.978)
Mass-100K	75K	0.704 (0.682-0.725)	0.889 (0.873-0.904)	0.935 (0.923-0.948)	0.703 (0.679-0.724)	0.977 (0.972-0.981)
Mass-100K	100K	0.720 (0.699-0.742)	0.886 (0.871-0.901)	0.931 (0.919-0.943)	0.719 (0.697-0.741)	0.977 (0.972-0.981)
Mass-100K	125K	0.731 (0.709-0.752)	0.894 (0.879-0.910)	0.938 (0.926-0.949)	0.729 (0.706-0.750)	0.976 (0.972-0.981)

Extended Data Table 11: **Assessing pretraining length of UNI (pretrained on Mass-1K, Mass-22K, and Mass-100K) on OT-43 performance.** Comparisons of weakly-supervised performance on OT-43 of UNI pre-trained on different data sizes (Mass-1K, Mass-22K, Mass-100K), across different training iterations ranging from 50K to 125K. Pre-extracted patch features of each encoder with ABMIL were trained and evaluated on curated train-test folds (3944:1620), with test performance ($n = 1620$ slides) reported using top-1, top-3, and top-5 accuracy, weighted F1 score, and AUROC. Best performing model for each metric is bolded. 95% CI is included in parentheses.

Encoder	Full?	Top-1 ACC	Top-3 ACC	Top-5 ACC	Weighted F1	AUROC
ResNet-50 _{IN}	✓	0.156 (0.138-0.173)	0.309 (0.287-0.333)	0.391 (0.368-0.416)	0.115 (0.101-0.132)	0.874 (0.866-0.882)
CTransPath	✓	0.391 (0.366-0.415)	0.620 (0.597-0.645)	0.715 (0.694-0.736)	0.358 (0.333-0.383)	0.958 (0.954-0.963)
REMEDIS	✓	0.118 (0.102-0.133)	0.225 (0.205-0.244)	0.293 (0.270-0.314)	0.074 (0.060-0.087)	0.857 (0.849-0.867)
UNI	✓	0.525 (0.501-0.549)	0.751 (0.728-0.772)	0.829 (0.812-0.847)	0.509 (0.483-0.534)	0.971 (0.967-0.975)
ResNet-50 _{IN}	✗	0.148 (0.130-0.164)	0.299 (0.277-0.322)	0.378 (0.354-0.403)	0.105 (0.091-0.121)	0.869 (0.860-0.877)
CTransPath	✗	0.399 (0.375-0.423)	0.625 (0.602-0.649)	0.723 (0.702-0.746)	0.365 (0.342-0.389)	0.959 (0.955-0.963)
REMEDIS	✗	0.412 (0.387-0.435)	0.654 (0.630-0.678)	0.735 (0.713-0.757)	0.398 (0.372-0.421)	0.952 (0.946-0.956)
UNI	✗	0.538 (0.514-0.562)	0.759 (0.738-0.781)	0.843 (0.826-0.860)	0.522 (0.498-0.548)	0.972 (0.968-0.976)

Extended Data Table 12: **Weakly-supervised 108-class OncoTree code cancer classification (OT-108) based on in-house BWH data (108 classes).** Pre-extracted patch features of each encoder with ABMIL were trained and evaluated on curated train-test folds (3944:1620), with test performance ($n = 1620$ slides) reported using top-1, top-3, and top-5 accuracy, weighted F1 score, and AUROC. We report results for both extracted features using all tissue patches per WSI, as well as extracted features from 200 representative tissue patches per WSI (described in **Online Methods**). Best performing model for each metric is bolded. 95% CI is included in parentheses. We

Data Size	Iter	Top-1 ACC	Top-3 ACC	Top-5 ACC	Weighted F1	AUROC
Mass-1K	50K	0.459 (0.435-0.486)	0.679 (0.657-0.702)	0.767 (0.748-0.787)	0.436 (0.411-0.462)	0.968 (0.964-0.971)
Mass-1K	75K	0.464 (0.440-0.488)	0.681 (0.660-0.706)	0.757 (0.736-0.778)	0.440 (0.416-0.466)	0.967 (0.963-0.971)
Mass-1K	100K	0.458 (0.434-0.482)	0.675 (0.654-0.699)	0.760 (0.740-0.781)	0.436 (0.412-0.461)	0.964 (0.960-0.968)
Mass-1K	125K	0.473 (0.449-0.499)	0.673 (0.652-0.698)	0.757 (0.738-0.780)	0.455 (0.430-0.482)	0.961 (0.956-0.965)
Mass-22K	50K	0.511 (0.487-0.536)	0.752 (0.732-0.775)	0.830 (0.812-0.848)	0.493 (0.467-0.519)	0.976 (0.972-0.979)
Mass-22K	75K	0.522 (0.498-0.549)	0.748 (0.727-0.770)	0.840 (0.821-0.857)	0.498 (0.474-0.524)	0.976 (0.972-0.979)
Mass-22K	100K	0.512 (0.489-0.538)	0.747 (0.726-0.770)	0.830 (0.811-0.848)	0.491 (0.465-0.517)	0.974 (0.971-0.977)
Mass-22K	125K	0.508 (0.485-0.531)	0.740 (0.719-0.761)	0.825 (0.807-0.842)	0.486 (0.461-0.510)	0.972 (0.968-0.975)
Mass-100K	50K	0.511 (0.486-0.536)	0.741 (0.720-0.764)	0.827 (0.809-0.846)	0.491 (0.465-0.516)	0.974 (0.971-0.977)
Mass-100K	75K	0.523 (0.499-0.548)	0.762 (0.741-0.782)	0.837 (0.820-0.854)	0.507 (0.481-0.533)	0.975 (0.972-0.979)
Mass-100K	100K	0.533 (0.508-0.559)	0.768 (0.748-0.788)	0.841 (0.823-0.859)	0.516 (0.491-0.542)	0.975 (0.971-0.978)
Mass-100K	125K	0.538 (0.514-0.562)	0.759 (0.738-0.781)	0.843 (0.826-0.860)	0.522 (0.498-0.548)	0.972 (0.968-0.976)

Extended Data Table 13: **Assessing pretraining length of UNI (pretrained on Mass-1K, Mass-22K, and Mass-100K) on OT-108 performance.** Comparisons of weakly-supervised performance on OT-108 of UNI pretrained on different data sizes (Mass-1K, Mass-22K, Mass-100K), across different training iterations ranging from 50K to 125K. Pre-extracted patch features of each encoder with ABMIL were trained and evaluated on curated train-test folds (3944:1620), with test performance ($n = 1620$ slides) reported using top-1, top-3, and top-5 accuracy, weighted F1 score, and AUROC. Best performing model for each metric is bolded. 95% CI is included in parentheses.

Encoder	Balanced ACC	Weighted F1	AUROC
ResNet-50 _{IN}	0.726 (0.652-0.797)	0.765 (0.678-0.837)	0.752 (0.659-0.842)
CTransPath	0.897 (0.836-0.948)	0.907 (0.851-0.953)	0.930 (0.864-0.985)
REMEDIS	0.930 (0.884-0.969)	0.923 (0.877-0.962)	0.981 (0.947-1.000)
UNI	0.957 (0.911-0.991)	0.961 (0.922-0.992)	0.975 (0.937-1.000)

Extended Data Table 14: **Weakly-supervised breast metastasis detection based on CAMELYON16 (2 classes).** Pre-extracted patch features of each encoder with ABMIL were trained a custom train-validation split (90:10 ratio) of the official train set (270 slides) and tested on the official test set, with test performance ($n = 129$) reported using balanced accuracy, weighted F1 score, and AUROC. Best performing model for each metric is bolded. 95% CI is included in parentheses.

Encoder	Cohort	Balanced ACC	Weighted F1	AUROC
ResNet-50 _{IN}	TCGA	0.857 (0.787-0.929)	0.857 (0.786-0.929)	0.939 (0.893-0.978)
CTransPath	TCGA	0.949 (0.901-0.990)	0.949 (0.898-0.990)	0.993 (0.982-1.000)
REMEDIS	TCGA	0.949 (0.902-0.990)	0.949 (0.898-0.990)	0.985 (0.953-1.000)
UNI	TCGA	0.969 (0.932-1.000)	0.969 (0.929-1.000)	0.997 (0.989-1.000)
ResNet-50 _{IN}	CPTAC	0.852 (0.831-0.871)	0.849 (0.829-0.869)	0.924 (0.907-0.939)
CTransPath	CPTAC	0.884 (0.866-0.903)	0.881 (0.862-0.900)	0.953 (0.942-0.963)
REMEDIS	CPTAC	0.854 (0.833-0.873)	0.849 (0.828-0.869)	0.951 (0.938-0.962)
UNI	CPTAC	0.889 (0.870-0.908)	0.891 (0.872-0.909)	0.958 (0.946-0.969)

Extended Data Table 15: **Weakly-supervised NSCLC subtyping based on TCGA and CPTAC (2 classes).** Pre-extracted patch features of each encoder with ABMIL were trained and evaluated on the TCGA-NSCLC cohort (label-stratified into train-validation-test folds with 80:10:10 ratio, 848:97:98 slides), with external evaluation on slides ($n = 1091$) sourced from CPTAC-LUAD ($n = 578$) and CPTAC-LUSC ($n = 513$). Test performance was reported using balanced accuracy, weighted F1 score, and AUROC. Best performing model for each metric is bolded. 95% CI is included in parentheses.

Encoder	Cohort	Balanced ACC	Weighted F1	AUROC
ResNet-50 _{IN}	TCGA	0.849 (0.734-0.940)	0.877 (0.814-0.938)	0.977 (0.954-0.993)
CTransPath	TCGA	0.892 (0.800-0.969)	0.907 (0.847-0.959)	0.987 (0.970-0.998)
REMEDIS	TCGA	0.973 (0.937-1.000)	0.969 (0.927-1.000)	0.997 (0.992-1.000)
UNI	TCGA	0.947 (0.875-0.994)	0.959 (0.918-0.990)	0.994 (0.984-1.000)
ResNet-50 _{IN}	CPTAC-DHMC	0.824 (0.751-0.894)	0.903 (0.886-0.921)	0.972 (0.957-0.984)
CTransPath	CPTAC-DHMC	0.939 (0.888-0.984)	0.968 (0.957-0.979)	0.996 (0.993-0.998)
REMEDIS	CPTAC-DHMC	0.790 (0.725-0.858)	0.934 (0.919-0.949)	0.988 (0.982-0.993)
UNI	CPTAC-DHMC	0.963 (0.930-0.987)	0.971 (0.960-0.981)	0.993 (0.985-0.998)

Extended Data Table 16: **Weakly-supervised RCC subtyping based on TCGA and CPTAC-DHMC (3 classes)**. Pre-extracted patch features of each encoder with ABMIL were trained and evaluated on the TCGA-RCC cohort (label-stratified into train-validation-test folds with 80:10:10 ratio, 736:89:97 slides), with external evaluation on slides ($n = 872$) sourced from CPTAC-CCRCC ($n = 404$) and DHMC-Kidney ($n = 468$) (CCRCC, CHRCC, and PRCC cases only). Test performance was reported using balanced accuracy, weighted F1 score, and AUROC. Best performing model for each metric is bolded. 95% CI is included in parentheses.

Encoder	Balanced ACC	Weighted F1	AUROC
ResNet-50 _{IN}	0.346 (0.306-0.386)	0.478 (0.383-0.565)	0.818 (0.785-0.850)
CTransPath	0.804 (0.743-0.879)	0.883 (0.823-0.937)	0.987 (0.976-0.995)
REMEDIS	0.865 (0.789-0.929)	0.877 (0.818-0.929)	0.973 (0.953-0.988)
UNI	0.919 (0.852-0.968)	0.926 (0.882-0.966)	0.993 (0.983-0.999)

Extended Data Table 17: **Weakly-supervised RCC subtyping based on DHMC (5 classes)**. Pre-extracted patch features of each encoder with ABMIL were trained and evaluated on a modified configuration of the official train-validation-test folds (70:4:26 ratio, 393:23:147 slides), with test performance ($n = 147$ slides) reported using balanced accuracy, weighted F1 score, and AUROC. Since no CHRCC slides were included in the validation fold, 8 CHRCC slides from the training fold was moved to the validation fold. The test fold was unmodified. Best performing model for each metric is bolded. 95% CI is included in parentheses.

Encoder	Balanced ACC	Weighted F1	AUROC
ResNet-50 _{IN}	0.250 (0.250-0.250)	0.356 (0.209-0.525)	0.671 (0.594-0.754)
CTransPath	0.556 (0.454-0.651)	0.728 (0.603-0.841)	0.845 (0.779-0.898)
REMEDIS	0.604 (0.499-0.696)	0.787 (0.670-0.889)	0.888 (0.814-0.960)
UNI	0.643 (0.549-0.725)	0.824 (0.706-0.931)	0.957 (0.908-0.987)

Extended Data Table 18: **Weakly-supervised CRC screening based on HunCRC (4 classes)**. Pre-extracted patch features of each encoder with ABMIL were trained and evaluated on the HunCRC cohort (label-stratified into train-validation-test folds with 50:25:25 ratio, 100:50:50 slides). Test performance was reported using balanced accuracy, weighted F1 score, and AUROC. Best performing model for each metric is bolded. 95% CI is included in parentheses.

Encoder	Balanced ACC	Weighted F1	AUROC
ResNet-50 _{IN}	0.552 (0.490-0.607)	0.516 (0.396-0.629)	0.748 (0.675-0.816)
CTransPath	0.639 (0.554-0.728)	0.648 (0.536-0.763)	0.840 (0.776-0.903)
REMEDI5	0.676 (0.578-0.770)	0.696 (0.591-0.796)	0.864 (0.805-0.915)
UNI	0.687 (0.617-0.760)	0.691 (0.562-0.800)	0.887 (0.833-0.936)

Extended Data Table 19: **Weakly-supervised BRCA coarse-grained subtyping based on BRACS (3 classes)**. Pre-extracted patch features of each encoder with ABMIL were trained and evaluated on the official train-validation-test folds (72:12:16 ratio, 395:65:87 slides), with test performance ($n = 87$ slides) reported using balanced accuracy, weighted F1 score, and AUROC. Best performing model for each metric is bolded. 95% CI is included in parentheses.

Encoder	Balanced ACC	Weighted F1	AUROC
ResNet-50 _{IN}	0.248 (0.214-0.276)	0.216 (0.132-0.311)	0.701 (0.645-0.754)
CTransPath	0.360 (0.284-0.440)	0.377 (0.280-0.485)	0.761 (0.706-0.809)
REMEDI5	0.398 (0.307-0.483)	0.428 (0.320-0.530)	0.749 (0.689-0.804)
UNI	0.468 (0.393-0.550)	0.486 (0.366-0.592)	0.837 (0.794-0.879)

Extended Data Table 20: **Weakly-supervised BRCA fine-grained subtyping based on BRACS (7 classes)**. Pre-extracted patch features of each encoder with ABMIL were trained and evaluated on the official train-validation-test (72:12:16 ratio, 395:65:87 slides), with test performance ($n = 87$ slides) reported using balanced accuracy, weighted F1 score, and AUROC. Best performing model for each metric is bolded. 95% CI is included in parentheses.

Encoder	Cohort	Balanced ACC	Weighted F1	AUROC
ResNet-50 _{IN}	TCGA	0.768 (0.710-0.821)	0.810 (0.767-0.850)	0.864 (0.825-0.901)
CTransPath	TCGA	0.891 (0.859-0.920)	0.862 (0.828-0.894)	0.958 (0.938-0.975)
REMEDI5	TCGA	0.819 (0.770-0.869)	0.860 (0.824-0.897)	0.933 (0.907-0.956)
UNI	TCGA	0.808 (0.760-0.855)	0.831 (0.794-0.867)	0.925 (0.898-0.949)
ResNet-50 _{IN}	EBRAINS	0.759 (0.731-0.786)	0.777 (0.749-0.804)	0.822 (0.794-0.849)
CTransPath	EBRAINS	0.836 (0.814-0.861)	0.819 (0.795-0.846)	0.924 (0.905-0.941)
REMEDI5	EBRAINS	0.792 (0.765-0.818)	0.822 (0.795-0.850)	0.895 (0.873-0.916)
UNI	EBRAINS	0.856 (0.836-0.878)	0.841 (0.820-0.864)	0.941 (0.925-0.955)

Extended Data Table 21: **Weakly-supervised GBMLGG *IDH1* mutation prediction based on TCGA and EBRAINS (2 classes)**. Pre-extracted patch features of each encoder with ABMIL were trained and evaluated on the TCGA-GBMLGG cohort (site-stratified into train-validation-test folds with 47:22:33 ratio, 525:243:355 slides), with external evaluation on slides ($n = 873$) sourced from the EBRAINS Digital Tumor Atlas (using slides with available *IDH1* status). Test performance was reported using balanced accuracy, weighted F1 score, and AUROC. Best performing model for each metric is bolded. 95% CI is included in parentheses.

Encoder	Cohort	Balanced ACC	Weighted F1	AUROC
ResNet-50 _{IN}	TCGA	0.412 (0.362-0.462)	0.660 (0.611-0.715)	0.814 (0.783-0.847)
CTransPath	TCGA	0.487 (0.437-0.543)	0.718 (0.671-0.769)	0.866 (0.831-0.905)
REMEDIS	TCGA	0.415 (0.382-0.448)	0.675 (0.628-0.727)	0.837 (0.811-0.864)
UNI	TCGA	0.673 (0.616-0.732)	0.794 (0.751-0.838)	0.910 (0.880-0.939)
ResNet-50 _{IN}	EBRAINS	0.402 (0.379-0.423)	0.615 (0.581-0.648)	0.684 (0.654-0.713)
CTransPath	EBRAINS	0.498 (0.472-0.523)	0.705 (0.674-0.735)	0.823 (0.798-0.845)
REMEDIS	EBRAINS	0.337 (0.320-0.354)	0.551 (0.517-0.586)	0.751 (0.723-0.777)
UNI	EBRAINS	0.562 (0.535-0.594)	0.728 (0.702-0.755)	0.868 (0.848-0.887)

Extended Data Table 22: **Weakly-supervised GBMLGG histomolecular subtyping based on TCGA and EBRAINS (5 classes)**. Pre-extracted patch features of each encoder with ABMIL were trained and evaluated on the TCGA-GBMLGG cohort (site-stratified into train-validation-test folds with 47:22:33 ratio, 525:243:355 slides), with external evaluation on slides ($n = 873$) sourced from the EBRAINS Digital Tumor Atlas (using slides with available *IDH1* status). Test performance was reported using balanced accuracy, weighted F1 score, and AUROC. Best performing model for each metric is bolded. 95% CI is included in parentheses.

Encoder	Balanced ACC	Weighted F1	AUROC
ResNet-50 _{IN}	0.302 (0.273-0.334)	0.556 (0.509-0.600)	0.878 (0.860-0.896)
CTransPath	0.666 (0.608-0.722)	0.795 (0.758-0.829)	0.968 (0.957-0.978)
REMEDIS	0.687 (0.638-0.734)	0.789 (0.753-0.824)	0.967 (0.952-0.979)
UNI	0.883 (0.838-0.924)	0.926 (0.902-0.947)	0.996 (0.994-0.998)

Extended Data Table 23: **Weakly-supervised brain tumor subtyping based on EBRAINS (12 classes)**. Pre-extracted patch features of each encoder with ABMIL were trained and evaluated on the EBRAINS Digital Tumor Atlas (label-stratified into train-validation-test folds with 50:25:25 ratio, 1151:595:573 slides), with test performance reported using balanced accuracy, weighted F1 score, and AUROC. Best performing model for each metric is bolded. 95% CI is included in parentheses.

Encoder	Balanced ACC	Weighted F1	AUROC
ResNet-50 _{IN}	0.219 (0.195-0.241)	0.300 (0.259-0.339)	0.893 (0.879-0.907)
CTransPath	0.514 (0.473-0.559)	0.597 (0.548-0.638)	0.959 (0.950-0.967)
REMEDIS	0.382 (0.346-0.415)	0.471 (0.428-0.512)	0.917 (0.901-0.931)
UNI	0.675 (0.633-0.715)	0.746 (0.704-0.783)	0.976 (0.969-0.982)

Extended Data Table 24: **Weakly-supervised brain tumor subtyping based on EBRAINS (30 classes)**. Pre-extracted patch features of each encoder with ABMIL were trained and evaluated on the EBRAINS Digital Tumor Atlas (label-stratified into train-validation-test folds with 50:25:25 ratio, 1151:595:573 slides), with test performance reported using balanced accuracy, weighted F1 score, and AUROC. Best performing model for each metric is bolded. 95% CI is included in parentheses.

Encoder	Balanced ACC	Quad. Weighted κ	Weighted F1	AUROC
ResNet-50 _{IN}	0.574 (0.544-0.603)	0.831 (0.799-0.859)	0.631 (0.599-0.661)	0.885 (0.873-0.897)
CTransPath	0.691 (0.658-0.723)	0.927 (0.912-0.940)	0.752 (0.723-0.779)	0.938 (0.929-0.947)
REMEDIS	0.711 (0.679-0.742)	0.932 (0.918-0.945)	0.766 (0.737-0.794)	0.941 (0.931-0.949)
UNI	0.757 (0.726-0.785)	0.946 (0.933-0.957)	0.809 (0.783-0.834)	0.956 (0.947-0.963)

Extended Data Table 25: **Weakly-supervised ISUP grading based on PANDA (6 classes)**. Pre-extracted patch features of each encoder with ABMIL were trained and evaluated on label-stratified train-validation-test folds (80:10:10 ratio, 7647:954:954 slides), with test performance (954 slides) reported using balanced accuracy, Cohen’s quadratic weighted κ , weighted F1 core, and ROC AUC. Best performing model for each metric is bolded. 95% CI is included in parentheses.

Encoder	Balanced ACC	Weighted F1	AUROC
ResNet-50 _{IN}	0.861 (0.822-0.898)	0.861 (0.822-0.898)	0.930 (0.903-0.955)
CTransPath	0.882 (0.847-0.916)	0.882 (0.846-0.916)	0.937 (0.909-0.961)
REMEDIS	0.861 (0.823-0.895)	0.861 (0.822-0.895)	0.933 (0.908-0.958)
UNI	0.896 (0.864-0.927)	0.894 (0.862-0.925)	0.962 (0.944-0.979)

Extended Data Table 26: **Weakly-supervised cellular-mediated allograft rejection of endomyocardial biopsies based on in-house BWH data (2 classes)**. Pre-extracted patch features of each encoder with ABMIL were trained and evaluated on case- and label-stratified train-validation-test folds (70:10:20 ratio, 3547:484:900 slides), with test performance (900 slides) reported using balanced accuracy, weighted F1 core, and ROC AUC. Best performing model for each metric is bolded. 95% CI is included in parentheses.

Encoder	Balanced ACC	Weighted F1	AUROC
ResNet-50 _{IN}	0.715 (0.705-0.724)	0.771 (0.761-0.781)	0.958 (0.954-0.961)
CTransPath	0.845 (0.836-0.853)	0.867 (0.859-0.875)	0.991 (0.990-0.992)
REMEDIS	0.787 (0.776-0.796)	0.802 (0.793-0.811)	0.980 (0.979-0.982)
UNI	0.874 (0.866-0.881)	0.875 (0.868-0.882)	0.990 (0.988-0.991)

Extended Data Table 27: **Linear probe evaluation for CRC tissue classification based on CRC-100K (9 classes)**. Pre-extracted patch features of each encoder with logistic regression were evaluated on the official train-test folds (100,000:7,180), with test performance (n=7,180 ROIs) reported using balanced accuracy, weighted F1 score, and AUROC. Best performing model for each metric is bolded. 95% CI is included in parentheses.

Encoder	1-NN Balanced ACC	1-NN Weighted F1	20-NN Balanced ACC	20-NN Weighted F1
ResNet-50 _{IN}	0.686 (0.676-0.696)	0.698 (0.686-0.708)	0.797 (0.787-0.806)	0.833 (0.825-0.841)
CTransPath	0.815 (0.806-0.824)	0.845 (0.836-0.854)	0.836 (0.828-0.843)	0.848 (0.840-0.857)
REMEDIS	0.855 (0.848-0.863)	0.881 (0.873-0.888)	0.908 (0.901-0.915)	0.924 (0.918-0.931)
UNI	0.899 (0.892-0.905)	0.912 (0.906-0.919)	0.924 (0.917-0.931)	0.945 (0.940-0.950)

Extended Data Table 28: **Few-shot and KNN evaluation for CRC tissue classification based on CRC-100K (9 classes)**. Pre-extracted patch features of each encoder with SimpleShot ($K=1$) and Nearest Neighbors ($K=20$) were evaluated on the official train-test folds (100,000:7,180 ROIs), with test performance (n=7,180 ROIs) reported using balanced accuracy and weighted F1 score. Best performing model for each metric is bolded. 95% CI is included in parentheses.

Encoder	Balanced ACC	Weighted F1	AUROC
ResNet-50 _{IN}	0.770 (0.761-0.779)	0.733 (0.722-0.745)	0.937 (0.932-0.941)
CTransPath	0.802 (0.791-0.812)	0.783 (0.773-0.793)	0.939 (0.934-0.943)
REMEDIS	0.729 (0.717-0.740)	0.744 (0.733-0.754)	0.906 (0.899-0.912)
UNI	0.890 (0.883-0.898)	0.880 (0.871-0.888)	0.979 (0.977-0.981)

Extended Data Table 29: **Linear probe evaluation for CCRCC tissue classification based on TCGA and HEL (3 classes)**. Pre-extracted patch features of each encoder with logistic regression were evaluated on the TCGA cohort as the train fold and HEL cohort as the test fold (89:11 ratio, 24,201:2,968 ROIs), with test performance (n=2,968 ROIs) reported using balanced accuracy, weighted F1 score, and AUROC. Best performing model for each metric is bolded. 95% CI is included in parentheses.

Encoder	1-NN Balanced ACC	1-NN Weighted F1	20-NN Balanced ACC	20-NN Weighted F1
ResNet-50 _{IN}	0.765 (0.755-0.775)	0.741 (0.730-0.751)	0.680 (0.670-0.690)	0.641 (0.629-0.653)
CTransPath	0.679 (0.667-0.691)	0.653 (0.639-0.665)	0.697 (0.686-0.708)	0.679 (0.668-0.690)
REMEDIS	0.785 (0.775-0.795)	0.788 (0.778-0.798)	0.833 (0.823-0.843)	0.827 (0.816-0.836)
UNI	0.801 (0.790-0.810)	0.801 (0.791-0.811)	0.866 (0.857-0.875)	0.860 (0.851-0.868)

Extended Data Table 30: **Few-shot and KNN evaluation for CCRCC tissue classification based on TCGA and HEL (3 classes)**. Pre-extracted patch features of each encoder with SimpleShot ($K=1$) and Nearest Neighbors ($K=20$) were evaluated on the TCGA cohort as the train fold and HEL cohort as the test fold (89:11 ratio, 24,201:2,968 ROIs), with test performance (n=2,968 ROIs) reported using balanced accuracy and weighted F1 score. Best performing model for each metric is bolded. 95% CI is included in parentheses.

Encoder	Img Res.	Balanced ACC	Weighted F1	AUROC
ResNet-50 _{IN}	224	0.738 (0.634-0.824)	0.733 (0.630-0.828)	0.911 (0.854-0.954)
CTransPath	224	0.875 (0.804-0.939)	0.872 (0.796-0.937)	0.982 (0.967-0.994)
REMEDIS	224	0.863 (0.782-0.933)	0.864 (0.786-0.937)	0.981 (0.959-0.997)
UNI	224	0.925 (0.856-0.976)	0.926 (0.866-0.975)	0.994 (0.983-1.000)
ResNet-50 _{IN}	448	0.712 (0.610-0.810)	0.714 (0.610-0.815)	0.901 (0.841-0.951)
CTransPath	448	0.863 (0.785-0.933)	0.864 (0.790-0.937)	0.973 (0.946-0.992)
REMEDIS	448	0.913 (0.845-0.970)	0.913 (0.842-0.964)	0.997 (0.990-1.000)
UNI	448	0.950 (0.898-0.989)	0.950 (0.901-0.988)	0.998 (0.995-1.000)
ResNet-50 _{IN}	896	0.600 (0.484-0.704)	0.607 (0.496-0.711)	0.848 (0.777-0.909)
CTransPath	896	0.788 (0.688-0.868)	0.791 (0.695-0.866)	0.949 (0.909-0.978)
REMEDIS	896	0.825 (0.741-0.900)	0.830 (0.748-0.902)	0.960 (0.926-0.984)
UNI	896	0.925 (0.858-0.976)	0.926 (0.862-0.975)	0.996 (0.990-1.000)
ResNet-50 _{IN}	1344	0.587 (0.464-0.697)	0.593 (0.478-0.697)	0.829 (0.754-0.894)
CTransPath	1344	0.650 (0.547-0.749)	0.656 (0.554-0.753)	0.879 (0.817-0.929)
REMEDIS	1344	0.812 (0.721-0.886)	0.821 (0.728-0.891)	0.966 (0.936-0.987)
UNI	1344	0.900 (0.829-0.960)	0.901 (0.829-0.962)	0.987 (0.970-0.997)

Extended Data Table 31: **Linear probe evaluation for BRCA subtyping based on BACH (4 classes)**. Pre-extracted patch features of each encoder with logistic regression were evaluated on label-stratified train-test folds (80:20 ratio, 320:80 ROIs) across multiple image resolutions (without stain normalization), with test performance (n=80 ROIs) reported using balanced accuracy, weighted F1 score, and AUROC. Best performing model for each metric is bolded. 95% CI is included in parentheses.

Encoder	Img Res.	1-NN Balanced ACC	1-NN Weighted F1	20-NN Balanced ACC	20-NN Weighted F1
ResNet-50 _{IN}	224	0.588 (0.484-0.688)	0.579 (0.455-0.685)	0.625 (0.516-0.723)	0.618 (0.504-0.723)
CTransPath	224	0.750 (0.662-0.834)	0.739 (0.635-0.834)	0.750 (0.656-0.837)	0.745 (0.640-0.838)
REMEDIS	224	0.650 (0.550-0.742)	0.628 (0.506-0.741)	0.825 (0.741-0.904)	0.823 (0.735-0.901)
UNI	224	0.812 (0.725-0.896)	0.813 (0.723-0.897)	0.900 (0.825-0.962)	0.902 (0.830-0.962)
ResNet-50 _{IN}	448	0.600 (0.497-0.697)	0.585 (0.471-0.703)	0.613 (0.506-0.717)	0.601 (0.483-0.716)
CTransPath	448	0.725 (0.630-0.814)	0.713 (0.599-0.819)	0.775 (0.682-0.863)	0.771 (0.671-0.862)
REMEDIS	448	0.575 (0.460-0.680)	0.569 (0.452-0.680)	0.687 (0.578-0.784)	0.688 (0.583-0.782)
UNI	448	0.887 (0.812-0.948)	0.888 (0.813-0.950)	0.912 (0.841-0.965)	0.912 (0.838-0.963)
ResNet-50 _{IN}	896	0.587 (0.486-0.688)	0.565 (0.448-0.691)	0.538 (0.429-0.636)	0.520 (0.399-0.638)
CTransPath	896	0.650 (0.545-0.742)	0.641 (0.531-0.745)	0.725 (0.622-0.811)	0.728 (0.624-0.817)
REMEDIS	896	0.562 (0.451-0.667)	0.568 (0.452-0.673)	0.625 (0.514-0.726)	0.638 (0.530-0.732)
UNI	896	0.850 (0.768-0.925)	0.849 (0.766-0.925)	0.887 (0.813-0.950)	0.885 (0.806-0.950)
ResNet-50 _{IN}	1344	0.525 (0.422-0.619)	0.507 (0.390-0.621)	0.475 (0.365-0.574)	0.474 (0.363-0.577)
CTransPath	1344	0.587 (0.478-0.691)	0.591 (0.478-0.701)	0.562 (0.444-0.663)	0.571 (0.460-0.674)
REMEDIS	1344	0.487 (0.371-0.594)	0.503 (0.386-0.613)	0.500 (0.389-0.610)	0.512 (0.398-0.616)
UNI	1344	0.812 (0.722-0.892)	0.808 (0.710-0.889)	0.837 (0.749-0.914)	0.836 (0.750-0.913)

Extended Data Table 32: **Few-shot and KNN evaluation for BRCA subtyping based on BACH (4 classes)**. Pre-extracted patch features of each encoder with SimpleShot ($K=1$) and Nearest Neighbors ($K=20$) were evaluated on label-stratified train-test folds (80:20 ratio, 320:80 ROIs) across multiple image resolutions (without stain normalization), with test performance (n=80 ROIs) reported using balanced accuracy and weighted F1 score. Best performing model for each metric is bolded. 95% CI is included in parentheses.

Encoder	Balanced ACC	Weighted F1	AUROC
ResNet-50 _{IN}	0.265 (0.259-0.271)	0.787 (0.781-0.793)	0.830 (0.822-0.839)
CTransPath	0.422 (0.409-0.435)	0.828 (0.823-0.833)	0.881 (0.874-0.889)
REMEDIS	0.410 (0.395-0.424)	0.816 (0.811-0.821)	0.836 (0.827-0.845)
UNI	0.465 (0.449-0.481)	0.844 (0.838-0.848)	0.888 (0.879-0.896)

Extended Data Table 33: **Linear probe evaluation for CRC tissue classification based on HunCRC (9 classes)**. Pre-extracted patch features of each encoder with logistic regression were evaluated on case-stratified train-test folds (77:23 ratio, 76,753:22,655 ROIs), with test performance (n=22,655 ROIs) reported using balanced accuracy, weighted F1 score, and AUROC. Best performing model for each metric is bolded. 95% CI is included in parentheses.

Encoder	1-NN Balanced ACC	1-NN Weighted F1	20-NN Balanced ACC	20-NN Weighted F1
ResNet-50 _{IN}	0.421 (0.398-0.446)	0.570 (0.563-0.576)	0.379 (0.363-0.393)	0.775 (0.769-0.781)
CTransPath	0.496 (0.475-0.517)	0.695 (0.690-0.701)	0.437 (0.425-0.453)	0.806 (0.800-0.811)
REMEDIS	0.445 (0.426-0.467)	0.681 (0.675-0.687)	0.400 (0.385-0.414)	0.805 (0.800-0.810)
UNI	0.470 (0.451-0.492)	0.747 (0.741-0.752)	0.448 (0.434-0.461)	0.831 (0.826-0.836)

Extended Data Table 34: **Few-shot and KNN evaluation for CRC tissue classification based on HunCRC (9 classes)**. Pre-extracted patch features of each encoder with SimpleShot ($K=1$) and Nearest Neighbors ($K=20$) were evaluated on case-stratified train-test folds (77:23 ratio, 76,753:22,655 ROIs), with test performance (n=22,655 ROIs) reported using balanced accuracy and weighted F1 score. Best performing model for each metric is bolded. 95% CI is included in parentheses.

Encoder	Balanced ACC	Weighted F1	AUROC
ResNet-50 _{IN}	0.576 (0.573-0.579)	0.853 (0.852-0.855)	0.938 (0.936-0.940)
CTransPath	0.728 (0.723-0.734)	0.925 (0.924-0.926)	0.964 (0.963-0.966)
REMEDIS	0.774 (0.768-0.779)	0.879 (0.878-0.881)	0.969 (0.967-0.970)
UNI	0.829 (0.823-0.834)	0.942 (0.941-0.943)	0.971 (0.970-0.973)

Extended Data Table 35: **Linear probe evaluation for ESCA subtyping based on UKK, WNS, TCGA and CHA (11 classes)**. Pre-extracted patch features of each encoder with logistic regression were evaluated using the UKK, WNS and TCGA cohorts as the train fold and the CHA cohort as the test fold (189,142:178,187), with test performance (n=178,187 ROIs) reported using balanced accuracy, weighted F1 score, and AUROC. Best performing model for each metric is bolded. 95% CI is included in parentheses.

Encoder	1-NN Balanced ACC	1-NN Weighted F1	20-NN Balanced ACC	20-NN Weighted F1
ResNet-50 _{IN}	0.641 (0.635-0.646)	0.720 (0.718-0.722)	0.631 (0.626-0.636)	0.837 (0.836-0.839)
CTransPath4	0.821 (0.817-0.826)	0.856 (0.855-0.858)	0.785 (0.780-0.789)	0.918 (0.916-0.919)
REMEDIS	0.793 (0.789-0.798)	0.867 (0.865-0.868)	0.777 (0.773-0.781)	0.918 (0.917-0.919)
UNI	0.835 (0.830-0.840)	0.904 (0.903-0.905)	0.836 (0.832-0.840)	0.947 (0.946-0.948)

Extended Data Table 36: **Few-shot and KNN evaluation for ESCA subtyping based on UKK, WNS, TCGA and CHA (11 classes)**. Pre-extracted patch features of each encoder with SimpleShot ($K=1$) and Nearest Neighbors ($K=20$) were evaluated using the UKK, WNS and TCGA cohorts as the train fold and the CHA cohort as the test fold (189,142:178,187 ROIs), with test performance (n=189,142 ROIs) reported using balanced accuracy and weighted F1 score. Best performing model for each metric is bolded. 95% CI is included in parentheses.

Encoder	Img Res.	Balanced ACC	Weighted F1	AUROC
ResNet-50 _{IN}	224	0.349 (0.327-0.370)	0.436 (0.412-0.457)	0.830 (0.819-0.840)
CTransPath	224	0.432 (0.410-0.453)	0.481 (0.459-0.505)	0.843 (0.833-0.851)
REMEDIS	224	0.446 (0.422-0.472)	0.473 (0.452-0.494)	0.801 (0.786-0.813)
UNI	224	0.504 (0.483-0.526)	0.533 (0.511-0.554)	0.825 (0.814-0.835)
ResNet-50 _{IN}	448	0.363 (0.343-0.383)	0.438 (0.416-0.460)	0.832 (0.821-0.841)
CTransPath	448	0.440 (0.419-0.460)	0.497 (0.475-0.519)	0.840 (0.829-0.849)
REMEDIS	448	0.458 (0.435-0.481)	0.534 (0.513-0.555)	0.816 (0.805-0.828)
UNI	448	0.514 (0.491-0.535)	0.565 (0.543-0.588)	0.836 (0.824-0.847)
ResNet-50 _{IN}	896	0.341 (0.322-0.361)	0.438 (0.415-0.461)	0.816 (0.806-0.826)
CTransPath	896	0.436 (0.418-0.456)	0.507 (0.486-0.530)	0.831 (0.820-0.841)
REMEDIS	896	0.502 (0.478-0.525)	0.553 (0.532-0.573)	0.830 (0.819-0.841)
UNI	896	0.530 (0.507-0.552)	0.589 (0.568-0.609)	0.853 (0.842-0.863)
ResNet-50 _{IN}	1792	0.308 (0.288-0.328)	0.435 (0.414-0.458)	0.780 (0.770-0.790)
CTransPath	1792	0.396 (0.376-0.414)	0.474 (0.453-0.496)	0.805 (0.795-0.816)
REMEDIS	1792	0.460 (0.436-0.485)	0.561 (0.542-0.583)	0.819 (0.808-0.830)
UNI	1792	0.528 (0.507-0.549)	0.572 (0.550-0.591)	0.856 (0.845-0.866)

Extended Data Table 37: **Linear probe evaluation for CRC polyp classification based on UniToPatho (6 classes)**. Pre-extracted patch features of each encoder with logistic regression were evaluated on the official train-test folds (72:28 ratio, 6,270:2,399 ROIs) across multiple image resolutions, with test performance (n=2,399 ROIs) reported using balanced accuracy, weighted F1 score, and AUROC. Best performing model for each metric is bolded. 95% CI is included in parentheses.

Encoder	Img Res.	1-NN Balanced ACC	1-NN Weighted F1	20-NN Balanced ACC	20-NN Weighted F1
ResNet-50 _{IN}	224	0.468 (0.440-0.493)	0.397 (0.375-0.417)	0.331 (0.309-0.353)	0.432 (0.408-0.453)
CTransPath	224	0.567 (0.544-0.589)	0.488 (0.467-0.510)	0.446 (0.425-0.468)	0.502 (0.481-0.525)
REMEDIS	224	0.494 (0.470-0.517)	0.420 (0.400-0.441)	0.353 (0.330-0.377)	0.466 (0.444-0.488)
UNI	224	0.533 (0.508-0.554)	0.429 (0.408-0.451)	0.425 (0.405-0.445)	0.476 (0.455-0.497)
ResNet-50 _{IN}	448	0.464 (0.437-0.489)	0.387 (0.364-0.408)	0.351 (0.330-0.373)	0.443 (0.421-0.465)
CTransPath	448	0.592 (0.569-0.614)	0.507 (0.486-0.527)	0.458 (0.436-0.480)	0.514 (0.494-0.535)
REMEDIS	448	0.517 (0.495-0.540)	0.398 (0.378-0.418)	0.406 (0.383-0.430)	0.464 (0.443-0.487)
UNI	448	0.602 (0.577-0.627)	0.550 (0.530-0.571)	0.458 (0.438-0.480)	0.503 (0.482-0.523)
ResNet-50 _{IN}	896	0.443 (0.420-0.469)	0.393 (0.372-0.413)	0.361 (0.341-0.384)	0.456 (0.436-0.479)
CTransPath	896	0.565 (0.540-0.587)	0.497 (0.477-0.517)	0.440 (0.417-0.462)	0.502 (0.482-0.524)
REMEDIS	896	0.515 (0.490-0.538)	0.426 (0.405-0.446)	0.369 (0.348-0.389)	0.442 (0.420-0.463)
UNI	896	0.619 (0.597-0.641)	0.543 (0.523-0.565)	0.471 (0.451-0.491)	0.508 (0.486-0.529)
ResNet-50 _{IN}	1792	0.351 (0.326-0.376)	0.323 (0.303-0.343)	0.350 (0.328-0.371)	0.469 (0.448-0.491)
CTransPath	1792	0.494 (0.471-0.516)	0.474 (0.456-0.494)	0.414 (0.394-0.436)	0.494 (0.473-0.517)
REMEDIS	1792	0.472 (0.446-0.495)	0.413 (0.393-0.433)	0.352 (0.330-0.376)	0.464 (0.443-0.484)
UNI	1792	0.616 (0.594-0.639)	0.568 (0.549-0.587)	0.476 (0.456-0.498)	0.529 (0.506-0.549)

Extended Data Table 38: **Few-shot and KNN evaluation for CRC polyp classification based on UniToPatho (6 classes)**. Pre-extracted patch features of each encoder with SimpleShot ($K=1$) and Nearest Neighbors ($K=20$) were evaluated on the official train-test folds (72:28 ratio, 6,270:2,399 ROIs) across multiple image resolutions, with test performance (n=2,399 ROIs) reported using balanced accuracy and weighted F1 score. Best performing model for each metric is bolded. 95% CI is included in parentheses.

Encoder	Balanced ACC	Quad. Weighted κ	Weighted F1	AUROC
ResNet-50 _{IN}	0.506 (0.504-0.507)	0.592 (0.589-0.594)	0.612 (0.610-0.614)	0.862 (0.861-0.862)
CTransPath	0.630 (0.629-0.632)	0.779 (0.777-0.781)	0.723 (0.722-0.725)	0.915 (0.914-0.915)
REMEDIS	0.630 (0.629-0.632)	0.761 (0.759-0.764)	0.716 (0.714-0.717)	0.906 (0.905-0.906)
UNI	0.658 (0.656-0.660)	0.797 (0.796-0.799)	0.743 (0.741-0.744)	0.922 (0.922-0.923)

Extended Data Table 39: **Linear probe evaluation for PRAD tissue classification based on AGGC (5 classes)**. Pre-extracted patch features of each encoder with logistic regression were evaluated on the label stratified train-test folds (69:31 ratio, 780,619:345,021 ROIs) and test performance (n=345,021 ROIs) reported using balanced accuracy, Cohen’s quadratic weighted κ , weighted F1 score, and AUROC. Best performing model for each metric is bolded. 95% CI is included in parentheses.

Encoder	1-NN Balanced ACC	1-NN Weighted F1	20-NN Balanced ACC	20-NN Weighted F1
ResNet-50 _{IN}	0.562 (0.560-0.564)	0.482 (0.481-0.484)	0.527 (0.526-0.529)	0.605 (0.603-0.606)
CTransPath	0.691 (0.690-0.693)	0.630 (0.628-0.631)	0.599 (0.597-0.600)	0.666 (0.664-0.668)
REMEDIS	0.655 (0.653-0.657)	0.600 (0.598-0.602)	0.617 (0.615-0.619)	0.674 (0.672-0.675)
UNI	0.738 (0.736-0.740)	0.697 (0.696-0.699)	0.655 (0.653-0.656)	0.714 (0.712-0.715)

Extended Data Table 40: **Few-shot and KNN evaluation for PRAD tissue classification based on AGGC (5 classes)**. Pre-extracted patch features of each encoder with SimpleShot ($K=1$) and Nearest Neighbors ($K=20$) were evaluated on label stratified train-test folds (69:31 ratio, 780,619:345,021 ROIs) and test performance (n=345,021 ROIs) reported using balanced accuracy and weighted F1 score. Best performing model for each metric is bolded. 95% CI is included in parentheses.

Encoder	SN	Balanced ACC	Weighted F1	AUROC
ResNet-50 _{IN}	✗	0.606 (0.598-0.614)	0.686 (0.681-0.691)	0.623 (0.615-0.633)
CTransPath	✗	0.714 (0.707-0.720)	0.772 (0.768-0.776)	0.782 (0.776-0.789)
REMEDIIS	✗	0.649 (0.642-0.656)	0.792 (0.788-0.797)	0.740 (0.733-0.747)
UNI	✗	0.716 (0.708-0.723)	0.813 (0.809-0.817)	0.797 (0.791-0.804)
ResNet-50 _{IN}	✓	0.606 (0.599-0.614)	0.678 (0.673-0.683)	0.629 (0.620-0.639)
CTransPath	✓	0.710 (0.703-0.717)	0.763 (0.759-0.767)	0.777 (0.770-0.784)
REMEDIIS	✓	0.631 (0.625-0.639)	0.777 (0.773-0.781)	0.696 (0.688-0.703)
UNI	✓	0.715 (0.708-0.722)	0.805 (0.801-0.809)	0.794 (0.788-0.801)

Extended Data Table 41: **Linear probe evaluation for CRC MSI prediction based on TCGA (2 classes)**. Pre-extracted patch features of each encoder with logistic regression were evaluated on official train-test folds (38:62 ratio, 19,557:32,361 ROIs), with test performance (n=32,361 ROIs) reported using balanced accuracy, weighted F1 score, and AUROC with and without stain normalization (SN). Best performing model for each metric is bolded. 95% CI is included in parentheses.

Encoder	SN	1-NN Balanced ACC	1-NN Weighted F1	20-NN Balanced ACC	20-NN Weighted F1
ResNet-50 _{IN}	✗	0.595 (0.587-0.602)	0.663 (0.658-0.668)	0.596 (0.590-0.604)	0.672 (0.667-0.676)
CTransPath	✗	0.614 (0.608-0.622)	0.669 (0.665-0.674)	0.630 (0.624-0.638)	0.736 (0.732-0.741)
REMEDIIS	✗	0.583 (0.576-0.590)	0.669 (0.664-0.673)	0.603 (0.595-0.610)	0.737 (0.733-0.742)
UNI	✗	0.682 (0.675-0.688)	0.726 (0.722-0.731)	0.694 (0.687-0.700)	0.769 (0.765-0.773)
ResNet-50 _{IN}	✓	0.592 (0.584-0.600)	0.656 (0.651-0.661)	0.596 (0.590-0.604)	0.671 (0.666-0.676)
CTransPath	✓	0.616 (0.608-0.623)	0.658 (0.653-0.663)	0.634 (0.627-0.641)	0.730 (0.726-0.735)
REMEDIIS	✓	0.610 (0.603-0.617)	0.658 (0.654-0.663)	0.617 (0.610-0.624)	0.724 (0.720-0.728)
UNI	✓	0.683 (0.676-0.690)	0.723 (0.718-0.727)	0.683 (0.676-0.690)	0.755 (0.751-0.759)

Extended Data Table 42: **Few-shot and KNN evaluation for CRC MSI prediction based on TCGA (2 classes)**. Pre-extracted patch features of each encoder with SimpleShot ($K=1$) and Nearest Neighbors ($K=20$) were evaluated on official train-test folds (38:62 ratio, 19,557:32,361 ROIs), with test performance (n=32,361 ROIs) reported using balanced accuracy and weighted F1 score with and without stain normalization (SN). Best performing model for each metric is bolded. 95% CI is included in parentheses.

Encoder	SN	Balanced ACC	Weighted F1	AUROC
ResNet-50 _{IN}	✗	0.439 (0.434-0.444)	0.525 (0.521-0.529)	0.926 (0.924-0.927)
CTransPath	✗	0.604 (0.599-0.610)	0.678 (0.674-0.682)	0.967 (0.966-0.968)
REMEDIIS	✗	0.650 (0.646-0.655)	0.709 (0.705-0.713)	0.959 (0.958-0.961)
UNI	✗	0.685 (0.680-0.690)	0.744 (0.741-0.748)	0.978 (0.978-0.979)
ResNet-50 _{IN}	✓	0.413 (0.408-0.418)	0.498 (0.493-0.502)	0.916 (0.914-0.918)
CTransPath	✓	0.561 (0.555-0.566)	0.637 (0.633-0.641)	0.960 (0.959-0.961)
REMEDIIS	✓	0.610 (0.605-0.615)	0.678 (0.674-0.682)	0.958 (0.956-0.959)
UNI	✓	0.657 (0.652-0.662)	0.718 (0.714-0.721)	0.975 (0.974-0.976)

Extended Data Table 43: **Linear probe evaluation for pan-cancer tissue classification based on TCGA (32 classes)**. Pre-extracted patch features of each encoder with logistic regression were evaluated on label-stratified train-test folds (216,350:55,360 ROIs), with test performance (n=55,360 ROIs) reported using balanced accuracy, weighted F1 score, and AUROC. Best performing model for each metric is bolded. 95% CI is included in parentheses.

Encoder	SN	1-NN Balanced ACC	1-NN Weighted F1	20-NN Balanced ACC	20-NN Weighted F1
ResNet-50 _{IN}	✗	0.287 (0.282-0.292)	0.269 (0.265-0.272)	0.347 (0.342-0.351)	0.415 (0.410-0.419)
CTransPath	✗	0.460 (0.454-0.465)	0.468 (0.464-0.472)	0.495 (0.490-0.499)	0.564 (0.560-0.568)
REMEDIS	✗	0.553 (0.548-0.558)	0.594 (0.590-0.598)	0.608 (0.603-0.612)	0.669 (0.665-0.673)
UNI	✗	0.641 (0.636-0.646)	0.675 (0.671-0.679)	0.645 (0.640-0.649)	0.707 (0.703-0.711)
ResNet-50 _{IN}	✓	0.275 (0.270-0.280)	0.254 (0.249-0.257)	0.318 (0.314-0.323)	0.382 (0.378-0.386)
CTransPath	✓	0.442 (0.436-0.447)	0.438 (0.434-0.442)	0.463 (0.459-0.468)	0.534 (0.529-0.538)
REMEDIS	✓	0.504 (0.499-0.510)	0.529 (0.525-0.533)	0.541 (0.537-0.546)	0.618 (0.614-0.622)
UNI	✓	0.591 (0.586-0.597)	0.611 (0.607-0.615)	0.595 (0.590-0.600)	0.663 (0.660-0.667)

Extended Data Table 44: **Few-shot and KNN evaluation for pan-cancer tissue classification based on TCGA (32 classes)**. Pre-extracted patch features of each encoder with SimpleShot ($K=1$) and Nearest Neighbors ($K=20$) were evaluated on label-stratified train-test folds (216,350:55,360 ROIs), with test performance (n=55,360 ROIs) reported using balanced accuracy and weighted F1 score with and without stain normalization (SN). Best performing model for each metric is bolded. 95% CI is included in parentheses.

Encoder	SN	Balanced ACC	Weighted F1	AUROC
ResNet-50 _{IN}	✗	0.667 (0.662-0.671)	0.845 (0.842-0.849)	0.919 (0.916-0.922)
CTransPath	✗	0.760 (0.756-0.765)	0.893 (0.891-0.896)	0.944 (0.942-0.946)
REMEDIS	✗	0.891 (0.886-0.894)	0.937 (0.935-0.939)	0.975 (0.973-0.976)
UNI	✗	0.887 (0.883-0.891)	0.944 (0.942-0.946)	0.979 (0.977-0.980)
ResNet-50 _{IN}	✓	0.651 (0.646-0.655)	0.836 (0.833-0.840)	0.915 (0.911-0.917)
CTransPath	✓	0.758 (0.753-0.762)	0.891 (0.889-0.894)	0.930 (0.928-0.933)
REMEDIS	✓	0.894 (0.890-0.898)	0.944 (0.942-0.946)	0.978 (0.977-0.979)
UNI	✓	0.870 (0.865-0.874)	0.938 (0.936-0.940)	0.975 (0.974-0.977)

Extended Data Table 45: **Linear probe evaluation for pan-cancer TIL detection based on TCGA (2 classes)**. Pre-extracted patch features of each encoder with logistic regression were evaluated on official train-validation-test folds (69:13:19 ratio, 209,221:38,601:56,275 ROIs, train-validation combined during training) and test performance (n=56,275 ROIs) reported using balanced accuracy, weighted F1 score, and AUROC with and without stain normalization (SN). Best performing model for each metric is bolded. 95% CI is included in parentheses.

Encoder	SN	1-NN Balanced ACC	1-NN Weighted F1	20-NN Balanced ACC	20-NN Weighted F1
ResNet-50 _{IN}	✗	0.811 (0.806-0.815)	0.842 (0.839-0.845)	0.821 (0.816-0.826)	0.908 (0.905-0.910)
CTransPath	✗	0.806 (0.802-0.811)	0.827 (0.824-0.829)	0.840 (0.836-0.845)	0.919 (0.916-0.921)
REMEDIS	✗	0.804 (0.800-0.808)	0.847 (0.844-0.849)	0.836 (0.832-0.841)	0.905 (0.903-0.908)
UNI	✗	0.886 (0.883-0.890)	0.931 (0.929-0.933)	0.865 (0.861-0.870)	0.935 (0.933-0.937)
ResNet-50 _{IN}	✓	0.812 (0.807-0.816)	0.848 (0.845-0.850)	0.806 (0.801-0.811)	0.900 (0.898-0.903)
CTransPath	✓	0.795 (0.790-0.799)	0.813 (0.810-0.816)	0.831 (0.827-0.836)	0.914 (0.911-0.916)
REMEDIS	✓	0.856 (0.852-0.860)	0.885 (0.883-0.888)	0.861 (0.857-0.865)	0.930 (0.928-0.932)
UNI	✓	0.865 (0.861-0.868)	0.907 (0.904-0.909)	0.855 (0.851-0.859)	0.931 (0.928-0.933)

Extended Data Table 46: **Few-shot and KNN evaluation for pan-cancer TIL detection based on TCGA (2 classes)**. Pre-extracted patch features of each encoder with SimpleShot ($K=1$) and Nearest Neighbors ($K=20$) were evaluated on official train-validation-test folds (69:13:19 ratio, 209,221:38,601:56,275 ROIs, train-validation combined during training) with test performance (n=56,275 ROIs) reported using balanced accuracy and weighted F1 score with and without stain normalization (SN). Best performing model for each metric is bolded. 95% CI is included in parentheses.

Encoder	Acc@1	Acc@3	Acc@5	MVAcc@5
ResNet-50 _{IN}	0.551 (0.549, 0.552)	0.765 (0.763, 0.766)	0.835 (0.834, 0.836)	0.623 (0.621, 0.624)
CTransPath	0.620 (0.618, 0.621)	0.795 (0.794, 0.797)	0.850 (0.849, 0.851)	0.671 (0.669, 0.672)
REMEDIS	0.620 (0.618, 0.621)	0.806 (0.804, 0.807)	0.860 (0.859, 0.861)	0.676 (0.675, 0.678)
UNI	0.663 (0.662, 0.665)	0.828 (0.827, 0.829)	0.875 (0.873, 0.876)	0.712 (0.710, 0.713)

Extended Data Table 47: **Image retrieval for PRAD tissue classification based on AGGC (5 classes)**. Pre-extracted patch features of each encoder with retrieval were evaluated on case-stratified train-test folds (780,619:345,021), with test performance (n=345,021 patches) reported using Acc@K for $K \in 1, 3, 5$ and MVAcc@5. Best performing model for each model is bolded. 95% CI is included in parentheses.

Encoder	Acc@1	Acc@3	Acc@5	MVAcc@5
ResNet-50 _{IN}	0.704 (0.693, 0.714)	0.869 (0.861, 0.877)	0.903 (0.895, 0.909)	0.805 (0.795, 0.814)
CTransPath	0.818 (0.809, 0.826)	0.863 (0.855, 0.871)	0.879 (0.871, 0.886)	0.840 (0.832, 0.849)
REMEDIS	0.895 (0.888, 0.902)	0.946 (0.941, 0.951)	0.958 (0.953, 0.962)	0.921 (0.915, 0.927)
UNI	0.913 (0.907, 0.919)	0.953 (0.948, 0.958)	0.964 (0.960, 0.969)	0.931 (0.926, 0.937)

Extended Data Table 48: **Image retrieval for CRC tissue classification based on CRC-100K (9 classes)**. Pre-extracted patch features of each encoder with retrieval were evaluated on the official train-test folds (100,000:7,180), with test performance (n=7,180 patches) reported using Acc@K for $K \in 1, 3, 5$ and MVAcc@5. Best performing model for each model is bolded. 95% CI is included in parentheses.

Encoder	Acc@1	Acc@3	Acc@5	MVAcc@5
ResNet-50 _{IN}	0.755 (0.753, 0.757)	0.859 (0.858, 0.861)	0.889 (0.888, 0.890)	0.793 (0.791, 0.795)
CTransPath	0.859 (0.857, 0.861)	0.928 (0.927, 0.929)	0.945 (0.944, 0.947)	0.884 (0.882, 0.885)
REMEDIS	0.873 (0.871, 0.874)	0.938 (0.937, 0.939)	0.954 (0.953, 0.955)	0.899 (0.898, 0.901)
UNI	0.911 (0.910, 0.912)	0.960 (0.959, 0.961)	0.971 (0.971, 0.972)	0.929 (0.928, 0.930)

Extended Data Table 49: **Image retrieval for ESCA subtyping based on UKK, WNS, TCGA and CHA (11 classes)**. Pre-extracted patch features of each encoder with retrieval were evaluated using the UKK, WNS and TCGA cohorts as the train fold and the CHA cohort as the test fold (189,142:178,187), with test performance (n=178,187 patches) reported using Acc@K for $K \in 1, 3, 5$ and MVAcc@5. Best performing model for each model is bolded. 95% CI is included in parentheses.

Encoder	Acc@1	Acc@3	Acc@5	MVAcc@5
ResNet-50 _{IN}	0.714 (0.708, 0.719)	0.872 (0.867, 0.876)	0.915 (0.911, 0.918)	0.770 (0.765, 0.775)
CTransPath	0.764 (0.758, 0.769)	0.880 (0.876, 0.884)	0.910 (0.906, 0.913)	0.798 (0.793, 0.803)
REMEDIS	0.765 (0.759, 0.770)	0.885 (0.882, 0.889)	0.917 (0.913, 0.920)	0.805 (0.800, 0.809)
UNI	0.793 (0.788, 0.798)	0.901 (0.897, 0.905)	0.928 (0.925, 0.931)	0.830 (0.825, 0.835)

Extended Data Table 50: **Image retrieval for CRC tissue classification based on HunCRC (9 classes)**. Pre-extracted patch features of each encoder with retrieval were evaluated on case-stratified train-test folds (76,753:22,655), with test performance (n=22,655 patches) reported using Acc@K for $K \in 1, 3, 5$ and MVAcc@5. Best performing model for each model is bolded. 95% CI is included in parentheses.

Encoder	SN	Acc@1	Acc@3	Acc@5	MVAcc@5
ResNet-50 _{IN}	✗	0.367 (0.363, 0.371)	0.532 (0.528, 0.537)	0.610 (0.606, 0.614)	0.453 (0.449, 0.458)
CTransPath	✗	0.521 (0.517, 0.525)	0.660 (0.657, 0.664)	0.722 (0.718, 0.725)	0.578 (0.575, 0.583)
REMEDIS	✗	0.627 (0.623, 0.631)	0.739 (0.735, 0.743)	0.786 (0.782, 0.789)	0.674 (0.670, 0.678)
UNI	✗	0.666 (0.663, 0.671)	0.780 (0.777, 0.784)	0.825 (0.822, 0.828)	0.712 (0.708, 0.716)
ResNet-50 _{IN}	✓	0.339 (0.335, 0.343)	0.508 (0.504, 0.512)	0.590 (0.586, 0.594)	0.433 (0.429, 0.437)
CTransPath	✓	0.483 (0.479, 0.488)	0.639 (0.635, 0.643)	0.707 (0.703, 0.711)	0.556 (0.552, 0.560)
REMEDIS	✓	0.567 (0.563, 0.571)	0.704 (0.701, 0.708)	0.760 (0.757, 0.764)	0.630 (0.626, 0.634)
UNI	✓	0.613 (0.609, 0.617)	0.748 (0.745, 0.752)	0.803 (0.800, 0.806)	0.672 (0.668, 0.676)

Extended Data Table 51: **Image retrieval for pan-cancer tissue classification based on TCGA (32 classes).** Pre-extracted patch features of each encoder with retrieval were evaluated on case-stratified train-test folds (216,350:55,360), with test performance (n=55,360 patches) reported using Acc@K for $K \in 1, 3, 5$ and MVAcc@5 with and without stain normalization (SN). Best performing model for each model is bolded. 95% CI is included in parentheses.

Encoder	Acc@1	Acc@3	Acc@5	MVAcc@5
ResNet-50 _{IN}	0.444 (0.424, 0.464)	0.648 (0.628, 0.666)	0.725 (0.707, 0.742)	0.514 (0.492, 0.534)
CTransPath	0.480 (0.460, 0.500)	0.632 (0.614, 0.651)	0.694 (0.675, 0.712)	0.523 (0.501, 0.541)
REMEDIS	0.437 (0.418, 0.456)	0.599 (0.580, 0.618)	0.670 (0.651, 0.688)	0.488 (0.469, 0.506)
UNI	0.504 (0.483, 0.524)	0.671 (0.652, 0.689)	0.736 (0.718, 0.753)	0.556 (0.536, 0.575)

Extended Data Table 52: **Image retrieval for CRC polyp classification based on UniToPatho.** Pre-extracted patch features of each encoder with retrieval were evaluated on the official case-stratified train-test folds (6,270:2,399) with resized 1792² image resolutions, with test performance (n=345,021 patches) reported using Acc@K for $K \in 1, 3, 5$ and MVAcc@5. Best performing model for each model is bolded. 95% CI is included in parentheses.

Encoder	Cell type	Dice	Precision	Recall
ResNet-50 _{IN}	Endothelium	0.665 (0.658-0.674)	0.709 (0.697-0.722)	0.658 (0.654-0.663)
CTransPath	Endothelium	0.658 (0.644-0.663)	0.695 (0.682-0.702)	0.656 (0.641-0.663)
REMEDIS	Endothelium	0.684 (0.677-0.694)	0.679 (0.672-0.688)	0.729 (0.724-0.736)
UNI	Endothelium	0.696 (0.686-0.703)	0.718 (0.707-0.726)	0.709 (0.700-0.716)
ResNet-50 _{IN}	Epithelium	0.812 (0.808-0.814)	0.840 (0.837-0.841)	0.816 (0.813-0.819)
CTransPath	Epithelium	0.815 (0.811-0.817)	0.842 (0.839-0.845)	0.816 (0.812-0.818)
REMEDIS	Epithelium	0.824 (0.819-0.829)	0.843 (0.840-0.846)	0.834 (0.829-0.838)
UNI	Epithelium	0.827 (0.823-0.830)	0.849 (0.847-0.851)	0.834 (0.831-0.838)
ResNet-50 _{IN}	Leukocyte	0.691 (0.689-0.693)	0.726 (0.724-0.727)	0.692 (0.690-0.695)
CTransPath	Leukocyte	0.686 (0.684-0.688)	0.710 (0.707-0.711)	0.699 (0.696-0.702)
REMEDIS	Leukocyte	0.706 (0.704-0.707)	0.725 (0.722-0.727)	0.719 (0.717-0.721)
UNI	Leukocyte	0.706 (0.705-0.709)	0.736 (0.734-0.737)	0.713 (0.712-0.716)
ResNet-50 _{IN}	Lymphocyte	0.631 (0.625-0.638)	0.693 (0.684-0.701)	0.626 (0.618-0.634)
CTransPath	Lymphocyte	0.629 (0.623-0.635)	0.677 (0.671-0.682)	0.627 (0.620-0.632)
REMEDIS	Lymphocyte	0.653 (0.650-0.660)	0.686 (0.680-0.696)	0.665 (0.659-0.669)
UNI	Lymphocyte	0.651 (0.647-0.658)	0.686 (0.680-0.693)	0.665 (0.657-0.673)
ResNet-50 _{IN}	Smooth Muscle	0.650 (0.646-0.652)	0.699 (0.696-0.703)	0.668 (0.664-0.672)
CTransPath	Smooth Muscle	0.655 (0.648-0.659)	0.703 (0.698-0.707)	0.670 (0.665-0.675)
REMEDIS	Smooth Muscle	0.674 (0.668-0.678)	0.724 (0.719-0.728)	0.687 (0.684-0.693)
UNI	Smooth Muscle	0.690 (0.685-0.694)	0.736 (0.731-0.740)	0.704 (0.700-0.708)
ResNet-50 _{IN}	Myeloid Cell	0.615 (0.611-0.620)	0.698 (0.690-0.703)	0.596 (0.592-0.602)
CTransPath	Myeloid Cell	0.621 (0.618-0.627)	0.697 (0.692-0.700)	0.604 (0.599-0.610)
REMEDIS	Myeloid Cell	0.652 (0.647-0.659)	0.728 (0.719-0.733)	0.630 (0.625-0.638)
UNI	Myeloid Cell	0.656 (0.655-0.662)	0.726 (0.724-0.730)	0.637 (0.634-0.643)
ResNet-50 _{IN}	Plasma Cell	0.703 (0.692-0.706)	0.761 (0.745-0.769)	0.692 (0.683-0.696)
CTransPath	Plasma Cell	0.713 (0.703-0.720)	0.754 (0.743-0.760)	0.709 (0.700-0.716)
REMEDIS	Plasma Cell	0.742 (0.734-0.747)	0.784 (0.775-0.786)	0.736 (0.725-0.742)
UNI	Plasma Cell	0.737 (0.730-0.743)	0.788 (0.778-0.794)	0.728 (0.722-0.732)
ResNet-50 _{IN}	RBC	0.797 (0.793-0.802)	0.827 (0.825-0.831)	0.808 (0.800-0.812)
CTransPath	RBC	0.786 (0.784-0.792)	0.818 (0.815-0.821)	0.794 (0.789-0.800)
REMEDIS	RBC	0.795 (0.791-0.800)	0.824 (0.821-0.827)	0.807 (0.802-0.815)
UNI	RBC	0.803 (0.800-0.808)	0.839 (0.837-0.843)	0.810 (0.804-0.817)
ResNet-50 _{IN}	Average	0.696	0.744	0.695
CTransPath	Average	0.695	0.737	0.700
REMEDIS	Average	0.716	0.749	0.726
UNI	Average	0.721	0.760	0.725

Extended Data Table 53: **Pan-cancer cell type segmentation based on SegPath (8 cell types treated as individual tasks).** ROI-level cell segmentation of eight major cell types using their official train-test folds in the SegPath dataset. We finetune each pretrained encoder using the Mask2Former framework¹³⁶, a flexible framework used commonly for adapting self-supervised models as segmentation backbones for dense prediction tasks. All encoders were trained and evaluated on the official train-validation-test folds, with test performance reported using dice score, precision, and recall. Best performing model for each metric is bolded. 95% CI is included in parentheses.

Encoder	Cohort	Top K	Balanced ACC	Weighted F1
ResNet-50 _{IN}	TCGA	5	0.531 (0.500-0.566)	0.398 (0.280-0.522)
CTransPath	TCGA	5	0.796 (0.705-0.869)	0.796 (0.712-0.868)
REMEDIS	TCGA	5	0.796 (0.707-0.874)	0.795 (0.709-0.877)
UNI	TCGA	5	0.908 (0.847-0.960)	0.908 (0.847-0.959)
ResNet-50 _{IN}	TCGA	50	0.531 (0.488-0.574)	0.412 (0.295-0.526)
CTransPath	TCGA	50	0.806 (0.724-0.878)	0.806 (0.724-0.878)
REMEDIS	TCGA	50	0.786 (0.701-0.868)	0.785 (0.701-0.867)
UNI	TCGA	50	0.918 (0.863-0.970)	0.918 (0.867-0.969)
ResNet-50 _{IN}	CPTAC	5	0.530 (0.517-0.544)	0.444 (0.407-0.481)
CTransPath	CPTAC	5	0.845 (0.823-0.865)	0.847 (0.825-0.867)
REMEDIS	CPTAC	5	0.771 (0.748-0.793)	0.752 (0.723-0.778)
UNI	CPTAC	5	0.902 (0.882-0.918)	0.902 (0.883-0.919)
ResNet-50 _{IN}	CPTAC	50	0.535 (0.520-0.551)	0.461 (0.426-0.497)
CTransPath	CPTAC	50	0.827 (0.805-0.848)	0.830 (0.808-0.852)
REMEDIS	CPTAC	50	0.806 (0.783-0.825)	0.793 (0.767-0.816)
UNI	CPTAC	50	0.901 (0.882-0.918)	0.901 (0.883-0.918)

Extended Data Table 54: **Prototypical NSCLC subtyping based on TCGA and CPTAC (2 classes)**. Class prototypes for MI-SimpleShot were developed using annotated ROIs from the TCGA Uniform Tumor Dataset, which we evaluate on the NSCLC subtyping task using the same folds in weakly-supervised ABMIL evaluation (train-test folds with 86:14, 602:98 slides), with external evaluation on slides ($n = 1091$) sourced from CPTAC-LUAD ($n = 578$) and CPTAC-LUSC ($n = 513$). Test performance was reported using balanced accuracy, and weighted F1 score. Best performing model for each metric is bolded. 95% CI is included in parentheses.

Encoder	Cohort	Top K	Balanced ACC	Weighted F1
ResNet-50 _{IN}	TCGA	5	0.636 (0.530-0.725)	0.501 (0.394-0.601)
CTransPath	TCGA	5	0.896 (0.814-0.950)	0.867 (0.803-0.928)
REMEDIS	TCGA	5	0.769 (0.712-0.828)	0.728 (0.625-0.826)
UNI	TCGA	5	0.928 (0.886-0.964)	0.888 (0.827-0.940)
ResNet-50 _{IN}	TCGA	50	0.700 (0.597-0.791)	0.607 (0.502-0.707)
CTransPath	TCGA	50	0.902 (0.824-0.956)	0.878 (0.813-0.930)
REMEDIS	TCGA	50	0.757 (0.696-0.820)	0.710 (0.609-0.809)
UNI	TCGA	50	0.938 (0.903-0.969)	0.897 (0.837-0.949)
ResNet-50 _{IN}	CPTAC	5	0.701 (0.654-0.741)	0.439 (0.405-0.473)
CTransPath	CPTAC	5	0.919 (0.905-0.930)	0.828 (0.804-0.849)
REMEDIS	CPTAC	5	0.957 (0.940-0.973)	0.939 (0.924-0.954)
UNI	CPTAC	5	0.952 (0.940-0.961)	0.896 (0.878-0.914)
ResNet-50 _{IN}	CPTAC	50	0.744 (0.694-0.791)	0.575 (0.543-0.606)
CTransPath	CPTAC	50	0.891 (0.846-0.925)	0.829 (0.807-0.849)
REMEDIS	CPTAC	50	0.957 (0.937-0.975)	0.951 (0.937-0.965)
UNI	CPTAC	50	0.957 (0.946-0.967)	0.909 (0.892-0.925)

Extended Data Table 55: **Prototypical RCC subtyping based on TCGA and CPTAC-DHMC (3 classes)**. Class prototypes for MI-SimpleShot were developed using annotated ROIs from the TCGA Uniform Tumor Dataset, which we evaluate on the RCC subtyping task using the same folds in weakly-supervised ABMIL evaluation (train-test folds with 82:18, 431:97 slides), with external evaluation on slides ($n = 872$) sourced from CPTAC-CCRCC ($n = 404$) and DHMC-Kidney ($n = 468$) (CCRCC, CHRCC, and PRCC cases only). Test performance was reported using balanced accuracy, and weighted F1 score. Best performing model for each metric is bolded. 95% CI is included in parentheses.

References

1. Coudray, N. *et al.* Classification and mutation prediction from non–small cell lung cancer histopathology images using deep learning. *Nature medicine* **24**, 1559–1567 (2018).
2. He, B. *et al.* Integrating spatial gene expression and breast tumour morphology via deep learning. *Nature biomedical engineering* **4**, 827–834 (2020).
3. Kather, J. N. *et al.* Deep learning can predict microsatellite instability directly from histology in gastrointestinal cancer. *Nature medicine* **25**, 1054–1056 (2019).
4. Skrede, O.-J. *et al.* Deep learning for prediction of colorectal cancer outcome: a discovery and validation study. *The Lancet* **395**, 350–360 (2020).
5. Wulczyn, E. *et al.* Interpretable survival prediction for colorectal cancer using deep learning. *npj Digital Medicine* **4** (2021).
6. Mobadersany, P. *et al.* Predicting cancer outcomes from histology and genomics using convolutional networks. *Proceedings of the National Academy of Sciences* **115**, E2970–E2979 (2018).
7. Courtiol, P. *et al.* Deep learning-based classification of mesothelioma improves prediction of patient outcome. *Nature Medicine* **25**, 1519–1525 (2019).
8. Vanguri, R. S. *et al.* Multimodal integration of radiology, pathology and genomics for prediction of response to pd-(l) 1 blockade in patients with non-small cell lung cancer. *Nature Cancer* (2022).
9. Bejnordi, B. E. *et al.* Diagnostic assessment of deep learning algorithms for detection of lymph node metastases in women with breast cancer. *JAMA* **318**, 2199–2210 (2017).
10. Bandi, P. *et al.* From detection of individual metastases to classification of lymph node status at the patient level: the camelyon17 challenge. *IEEE Transactions on Medical Imaging* **38**, 550–560 (2018).
11. Tolkach, Y., Dohmgörger, T., Toma, M. & Kristiansen, G. High-accuracy prostate cancer pathology using deep learning. *Nature Machine Intelligence* **2**, 411–418 (2020).
12. Bulten, W. *et al.* Automated deep-learning system for gleason grading of prostate cancer using biopsies: a diagnostic study. *The Lancet Oncology* **21**, 233–241 (2020).
13. Bera, K., Schalper, K. A., Rimm, D. L., Velcheti, V. & Madabhushi, A. Artificial intelligence in digital pathology—new tools for diagnosis and precision oncology. *Nature reviews Clinical oncology* **16**, 703–715 (2019).
14. Echle, A. *et al.* Deep learning in cancer pathology: a new generation of clinical biomarkers. *British journal of cancer* **124**, 686–696 (2021).
15. Hahn, W. C. *et al.* An expanded universe of cancer targets. *Cell* **184**, 1142–1155 (2021).
16. Cooper, M., Ji, Z. & Krishnan, R. G. Machine learning in computational histopathology: Challenges and opportunities. *Genes, Chromosomes and Cancer* (2023).
17. Graham, S. *et al.* Screening of normal endoscopic large bowel biopsies with interpretable graph learning: a retrospective study. *Gut* (2023).
18. Campanella, G. *et al.* Clinical-grade computational pathology using weakly supervised deep learning on whole slide images. *Nature Medicine* **25**, 1301–1309 (2019).
19. Kather, J. N. *et al.* Pan-cancer image-based detection of clinically actionable genetic alterations. *Nature Cancer* **1**, 789–799 (2020).

20. Fu, Y. *et al.* Pan-cancer computational histopathology reveals mutations, tumor composition and prognosis. *Nature Cancer* **1**, 800–810 (2020).
21. Bulten, W. *et al.* Artificial intelligence for diagnosis and gleason grading of prostate cancer: the panda challenge. *Nature Medicine* **28**, 154–163 (2022).
22. Chen, R. J. *et al.* Pan-cancer integrative histology-genomic analysis via multimodal deep learning. *Cancer Cell* **40**, 865–878 (2022).
23. Foersch, S. *et al.* Multistain deep learning for prediction of prognosis and therapy response in colorectal cancer. *Nature medicine* **29**, 430–439 (2023).
24. He, K. *et al.* Masked autoencoders are scalable vision learners. In *Proceedings of the IEEE/CVF conference on computer vision and pattern recognition*, 16000–16009 (2022).
25. Oquab, M. *et al.* Dinov2: Learning robust visual features without supervision. *arXiv preprint arXiv:2304.07193* (2023).
26. Huang, Z., Bianchi, F., Yuksekogonul, M., Montine, T. & Zou, J. Leveraging medical twitter to build a visual–language foundation model for pathology ai. *Nature medicine* (2023).
27. Lu, M. Y. *et al.* Towards a visual-language foundation model for computational pathology. *arXiv preprint arXiv:2307.12914* (2023).
28. Balestriero, R. *et al.* A cookbook of self-supervised learning. *arXiv preprint arXiv:2304.12210* (2023).
29. Chen, X., Xie, S. & He, K. An empirical study of training self-supervised vision transformers. In *Proceedings of the IEEE/CVF International Conference on Computer Vision* (2021).
30. Caron, M. *et al.* Emerging properties in self-supervised vision transformers. In *Proceedings of the IEEE/CVF international conference on computer vision*, 9650–9660 (2021).
31. Chen, T., Kornblith, S., Norouzi, M. & Hinton, G. A simple framework for contrastive learning of visual representations. In *International conference on machine learning*, 1597–1607 (PMLR, 2020).
32. Grill, J.-B. *et al.* Bootstrap your own latent—a new approach to self-supervised learning. *Advances in neural information processing systems* **33**, 21271–21284 (2020).
33. Oord, A. v. d., Li, Y. & Vinyals, O. Representation learning with contrastive predictive coding. *arXiv preprint arXiv:1807.03748* (2018).
34. Donahue, J. & Simonyan, K. Large scale adversarial representation learning. *Advances in neural information processing systems* **32** (2019).
35. Deng, J. *et al.* Imagenet: A large-scale hierarchical image database. In *2009 IEEE conference on computer vision and pattern recognition*, 248–255 (Ieee, 2009).
36. Russakovsky, O. *et al.* Imagenet large scale visual recognition challenge. *International journal of computer vision* **115**, 211–252 (2015).
37. Sun, C., Shrivastava, A., Singh, S. & Gupta, A. Revisiting unreasonable effectiveness of data in deep learning era. In *Proceedings of the IEEE international conference on computer vision*, 843–852 (2017).
38. Zhai, X., Kolesnikov, A., Houlsby, N. & Beyer, L. Scaling vision transformers. In *Proceedings of the IEEE/CVF Conference on Computer Vision and Pattern Recognition*, 12104–12113 (2022).
39. Goyal, P., Mahajan, D., Gupta, A. & Misra, I. Scaling and benchmarking self-supervised visual representation learning. In *Proceedings of the IEEE/CVF International Conference on computer vision*, 6391–6400 (2019).

40. OpenAI. Gpt-4 technical report (2023). 2303.08774.
41. Bommasani, R. *et al.* On the opportunities and risks of foundation models. *arXiv preprint arXiv:2108.07258* (2021).
42. Yuan, L. *et al.* Florence: A new foundation model for computer vision. *arXiv preprint arXiv:2111.11432* (2021).
43. Weinstein, J. N. *et al.* The cancer genome atlas pan-cancer analysis project. *Nature genetics* **45**, 1113–1120 (2013).
44. Wang, X. *et al.* Transpath: Transformer-based self-supervised learning for histopathological image classification. In *International Conference on Medical Image Computing and Computer-Assisted Intervention*, 186–195 (Springer, 2021).
45. Chen, R. J. & Krishnan, R. G. Self-supervised vision transformers learn visual concepts in histopathology. *Learning Meaningful Representations of Life, NeurIPS 2021* (2022).
46. Wang, X. *et al.* Transformer-based unsupervised contrastive learning for histopathological image classification. *Medical Image Analysis* **81**, 102559 (2022).
47. Azizi, S. *et al.* Robust and data-efficient generalization of self-supervised machine learning for diagnostic imaging. *Nature Biomedical Engineering* 1–24 (2023).
48. Kang, M., Song, H., Park, S., Yoo, D. & Pereira, S. Benchmarking self-supervised learning on diverse pathology datasets. In *Proceedings of the IEEE/CVF Conference on Computer Vision and Pattern Recognition*, 3344–3354 (2023).
49. Li, B., Li, Y. & Eliceiri, K. W. Dual-stream multiple instance learning network for whole slide image classification with self-supervised contrastive learning. In *Proceedings of the IEEE/CVF Conference on Computer Vision and Pattern Recognition*, 14318–14328 (2021).
50. Lazard, T., Lerousseau, M., Decencière, E. & Walter, T. Giga-ssl: Self-supervised learning for gigapixel images. In *Proceedings of the IEEE/CVF Conference on Computer Vision and Pattern Recognition*, 4304–4313 (2023).
51. Yu, Z., Lin, T. & Xu, Y. Slpd: Slide-level prototypical distillation for wsis. *arXiv preprint arXiv:2307.10696* (2023).
52. Schirris, Y., Gavves, E., Nederlof, I., Horlings, H. M. & Teuwen, J. Deepsmile: contrastive self-supervised pre-training benefits msi and hrd classification directly from h&e whole-slide images in colorectal and breast cancer. *Medical Image Analysis* **79**, 102464 (2022).
53. Vu, Q. D., Rajpoot, K., Raza, S. E. A. & Rajpoot, N. Handcrafted histological transformer (h2t): Unsupervised representation of whole slide images. *Medical Image Analysis* **85**, 102743 (2023).
54. Quiros, A. C. *et al.* Self-supervised learning unveils morphological clusters behind lung cancer types and prognosis. *arXiv preprint arXiv:2205.01931* (2022).
55. Claudio Quiros, A. *et al.* Adversarial learning of cancer tissue representations. In *International Conference on Medical Image Computing and Computer-Assisted Intervention*, 602–612 (Springer, 2021).
56. Zhao, Y. *et al.* Predicting lymph node metastasis using histopathological images based on multiple instance learning with deep graph convolution. In *Proceedings of the IEEE/CVF Conference on Computer Vision and Pattern Recognition*, 4837–4846 (2020).
57. Jiang, S., Hondelink, L., Suriawinata, A. A. & Hassanpour, S. Masked pre-training of transformers for histology image analysis. *arXiv preprint arXiv:2304.07434* (2023).

58. Wang, X. *et al.* Retccl: clustering-guided contrastive learning for whole-slide image retrieval. *Medical image analysis* **83**, 102645 (2023).
59. Filiot, A. *et al.* Scaling self-supervised learning for histopathology with masked image modeling. *medRxiv* 2023–07 (2023).
60. Srinidhi, C. L., Kim, S. W., Chen, F.-D. & Martel, A. L. Self-supervised driven consistency training for annotation efficient histopathology image analysis. *Medical Image Analysis* **75**, 102256 (2022).
61. Srinidhi, C. L. & Martel, A. L. Improving self-supervised learning with hardness-aware dynamic curriculum learning: an application to digital pathology. In *Proceedings of the IEEE/CVF International Conference on Computer Vision*, 562–571 (2021).
62. Saillard, C. *et al.* Self supervised learning improves dMMR/MSI detection from histology slides across multiple cancers. In *COMPAY 2021: The third MICCAI workshop on Computational Pathology* (2021).
63. Dehaene, O., Camara, A., Moindrot, O., de Lavergne, A. & Courtiol, P. Self-supervision closes the gap between weak and strong supervision in histology. *MLAH Workshop in NeurIPS* (2020).
64. Koohbanani, N. A., Unnikrishnan, B., Khurram, S. A., Krishnaswamy, P. & Rajpoot, N. Self-path: Self-supervision for classification of pathology images with limited annotations. *IEEE Transactions on Medical Imaging* (2021).
65. Boyd, J. *et al.* Self-supervised representation learning using visual field expansion on digital pathology. In *Proceedings of the IEEE/CVF International Conference on Computer Vision*, 639–647 (2021).
66. Ciga, O., Xu, T. & Martel, A. L. Self supervised contrastive learning for digital histopathology. *Machine Learning with Applications* 100198 (2021).
67. Li, J., Lin, T. & Xu, Y. Sslp: Spatial guided self-supervised learning on pathological images. In *Medical Image Computing and Computer Assisted Intervention–MICCAI 2021: 24th International Conference, Strasbourg, France, September 27–October 1, 2021, Proceedings, Part II* **24**, 3–12 (Springer, 2021).
68. Yang, P., Hong, Z., Yin, X., Zhu, C. & Jiang, R. Self-supervised visual representation learning for histopathological images. In *Medical Image Computing and Computer Assisted Intervention–MICCAI 2021: 24th International Conference, Strasbourg, France, September 27–October 1, 2021, Proceedings, Part II* **24**, 47–57 (Springer, 2021).
69. Lin, T. *et al.* Sgcl: Spatial guided contrastive learning on whole-slide pathological images. *Medical Image Analysis* 102845 (2023).
70. DiPalma, J., Torresani, L. & Hassanpour, S. Histoperm: A permutation-based view generation approach for improving histopathologic feature representation learning. *Journal of Pathology Informatics* **14**, 100320 (2023).
71. Tellez, D., Litjens, G., van der Laak, J. & Ciompi, F. Neural image compression for gigapixel histopathology image analysis. *IEEE Transactions on Pattern Analysis and Machine Intelligence* (2019).
72. Jiang, C. *et al.* Hierarchical discriminative learning improves visual representations of biomedical microscopy. In *Proceedings of the IEEE/CVF Conference on Computer Vision and Pattern Recognition*, 19798–19808 (2023).
73. Saldanha, O. L. *et al.* Self-supervised attention-based deep learning for pan-cancer mutation prediction from histopathology. *NPJ Precision Oncology* **7**, 35 (2023).
74. Niehues, J. M. *et al.* Generalizable biomarker prediction from cancer pathology slides with self-supervised deep learning: A retrospective multi-centric study. *Cell Reports Medicine* **4** (2023).

75. Seraphin, T. P. *et al.* Prediction of heart transplant rejection from routine pathology slides with self-supervised deep learning. *European Heart Journal-Digital Health* **4**, 265–274 (2023).
76. Lu, M. Y. *et al.* Visual language pretrained multiple instance zero-shot transfer for histopathology images. In *Proceedings of the IEEE/CVF Conference on Computer Vision and Pattern Recognition (CVPR)*, 19764–19775 (2023).
77. Mokhtari, R. *et al.* Interpretable histopathology-based prediction of disease relevant features in inflammatory bowel disease biopsies using weakly-supervised deep learning. In *Medical Imaging with Deep Learning* (2023).
78. Jaume, G. *et al.* Modeling dense multimodal interactions between biological pathways and histology for survival prediction. *arXiv preprint arXiv:2304.06819* (2023).
79. Hörst, F. *et al.* Histology-based prediction of therapy response to neoadjuvant chemotherapy for esophageal and esophagogastric junction adenocarcinomas using deep learning. *JCO Clinical Cancer Informatics* **7**, e2300038 (2023).
80. Wagner, S. J. *et al.* Fully transformer-based biomarker prediction from colorectal cancer histology: a large-scale multicentric study. *arXiv preprint arXiv:2301.09617* (2023).
81. Hörst, F. *et al.* Cellvit: Vision transformers for precise cell segmentation and classification. *arXiv preprint arXiv:2306.15350* (2023).
82. Zhang, J. *et al.* Prompt-mil: Boosting multi-instance learning schemes via task-specific prompt tuning. *arXiv preprint arXiv:2303.12214* (2023).
83. Kaczmarzyk, J. R. *et al.* Champkit: a framework for rapid evaluation of deep neural networks for patch-based histopathology classification. *Computer Methods and Programs in Biomedicine* 107631 (2023).
84. Zhang, J. *et al.* Gigapixel whole-slide images classification using locally supervised learning. In *International Conference on Medical Image Computing and Computer-Assisted Intervention*, 192–201 (Springer, 2022).
85. Nasrallah, M. P. *et al.* Machine learning for cryosection pathology predicts the 2021 who classification of glioma. *Med* (2023).
86. Li, H. *et al.* Task-specific fine-tuning via variational information bottleneck for weakly-supervised pathology whole slide image classification. In *Proceedings of the IEEE/CVF Conference on Computer Vision and Pattern Recognition*, 7454–7463 (2023).
87. Saltz, J. *et al.* Spatial organization and molecular correlation of tumor-infiltrating lymphocytes using deep learning on pathology images. *Cell reports* **23**, 181–193 (2018).
88. Komura, D. *et al.* Universal encoding of pan-cancer histology by deep texture representations. *Cell Reports* **38** (2022).
89. Kalra, S. *et al.* Yottixel—an image search engine for large archives of histopathology whole slide images. *Medical Image Analysis* **65**, 101757 (2020).
90. Schmauch, B. *et al.* A deep learning model to predict rna-seq expression of tumours from whole slide images. *Nature communications* **11**, 3877 (2020).
91. Graham, S. *et al.* One model is all you need: multi-task learning enables simultaneous histology image segmentation and classification. *Medical Image Analysis* **83**, 102685 (2023).
92. Diao, J. A. *et al.* Human-interpretable image features derived from densely mapped cancer pathology slides predict diverse molecular phenotypes. *Nature Communications* **12** (2021).

93. Wulczyn, E. *et al.* Deep learning-based survival prediction for multiple cancer types using histopathology images. *PLoS One* **15**, e0233678 (2020).
94. Riasatian, A. *et al.* Fine-tuning and training of densenet for histopathology image representation using tcga diagnostic slides. *Medical Image Analysis* **70**, 102032 (2021).
95. Dosovitskiy, A. *et al.* An image is worth 16x16 words: Transformers for image recognition at scale. In *International Conference on Learning Representations* (2021).
96. Consortium, G. *et al.* The genotype-tissue expression (gtex) pilot analysis: multitissue gene regulation in humans. *Science* **348**, 648–660 (2015).
97. Kundra, R. *et al.* Oncotree: a cancer classification system for precision oncology. *JCO clinical cancer informatics* **5**, 221–230 (2021).
98. Zhou, J. *et al.* ibot: Image bert pre-training with online tokenizer. *International Conference on Learning Representations* (2022).
99. Campbell, J. D. *et al.* Distinct patterns of somatic genome alterations in lung adenocarcinomas and squamous cell carcinomas. *Nature genetics* **48**, 607–616 (2016).
100. Lu, M. Y. *et al.* Data efficient and weakly supervised computational pathology on whole slide images. *Nature Biomedical Engineering* (2020).
101. Shao, Z. *et al.* Transmil: Transformer based correlated multiple instance learning for whole slide image classification. *Advances in Neural Information Processing Systems* **34** (2021).
102. Ilse, M., Tomczak, J. & Welling, M. Attention-based deep multiple instance learning. In *Proceedings of the 35th International Conference on Machine Learning*, 2132–2141 (2018).
103. He, K., Zhang, X., Ren, S. & Sun, J. Deep residual learning for image recognition. In *Proceedings of the IEEE conference on computer vision and pattern recognition*, 770–778 (2016).
104. Kim, Y. J. *et al.* Paip 2019: Liver cancer segmentation challenge. *Medical Image Analysis* **67**, 101854 (2021).
105. Lipkova, J. *et al.* Deep learning-enabled assessment of cardiac allograft rejection from endomyocardial biopsies. *Nature medicine* **28**, 575–582 (2022).
106. Edwards, N. J. *et al.* The cptac data portal: a resource for cancer proteomics research. *Journal of proteome research* **14**, 2707–2713 (2015).
107. Gillette, M. A. *et al.* Proteogenomic characterization reveals therapeutic vulnerabilities in lung adenocarcinoma. *Cell* **182**, 200–225 (2020).
108. Satpathy, S. *et al.* A proteogenomic portrait of lung squamous cell carcinoma. *Cell* **184**, 4348–4371 (2021).
109. Network, C. G. A. R. Comprehensive molecular characterization of clear cell renal cell carcinoma. *Nature* **499**, 43–49 (2013).
110. Davis, C. F. *et al.* The somatic genomic landscape of chromophobe renal cell carcinoma. *Cancer cell* **26**, 319–330 (2014).
111. Network, C. G. A. R. Comprehensive molecular characterization of papillary renal-cell carcinoma. *New England Journal of Medicine* **374**, 135–145 (2016).
112. Li, Y. *et al.* Histopathologic and proteogenomic heterogeneity reveals features of clear cell renal cell carcinoma aggressiveness. *Cancer cell* **41**, 139–163 (2023).

113. Zhu, M. *et al.* Development and evaluation of a deep neural network for histologic classification of renal cell carcinoma on biopsy and surgical resection slides. *Scientific reports* **11**, 7080 (2021).
114. Brancati, N. *et al.* Bracs: A dataset for breast carcinoma subtyping in h&e histology images. *Database* **2022**, baac093 (2022).
115. Roetzer-Pejrimovsky, T. *et al.* The digital brain tumour atlas, an open histopathology resource. *Scientific Data* **9**, 55 (2022).
116. Brennan, C. W. *et al.* The somatic genomic landscape of glioblastoma. *Cell* **155**, 462–477 (2013).
117. Network, C. G. A. R. Comprehensive, integrative genomic analysis of diffuse lower-grade gliomas. *New England Journal of Medicine* **372**, 2481–2498 (2015).
118. Jacovi, A., Caciularu, A., Goldman, O. & Goldberg, Y. Stop uploading test data in plain text: Practical strategies for mitigating data contamination by evaluation benchmarks. *arXiv preprint arXiv:2305.10160* (2023).
119. Magar, I. & Schwartz, R. Data contamination: From memorization to exploitation. In *Proceedings of the 60th Annual Meeting of the Association for Computational Linguistics (Volume 2: Short Papers)*, 157–165 (2022).
120. Brown, T. *et al.* Language models are few-shot learners. *Advances in neural information processing systems* **33**, 1877–1901 (2020).
121. Dodge, J. *et al.* Documenting large webtext corpora: A case study on the colossal clean crawled corpus. In *Proceedings of the 2021 Conference on Empirical Methods in Natural Language Processing*, 1286–1305 (2021).
122. Kapoor, S. & Narayanan, A. Leakage and the reproducibility crisis in machine-learning-based science. *Patterns* (2023).
123. Xiang, J. & Zhang, J. Exploring low-rank property in multiple instance learning for whole slide image classification. In *The Eleventh International Conference on Learning Representations* (2022).
124. Kather, J. N. *et al.* Predicting survival from colorectal cancer histology slides using deep learning: A retrospective multicenter study. *PLoS medicine* **16**, e1002730 (2019).
125. Pataki, B. Á. *et al.* Hunccrc: annotated pathological slides to enhance deep learning applications in colorectal cancer screening. *Scientific Data* **9**, 370 (2022).
126. Barbano, C. A. *et al.* Unitopatho, a labeled histopathological dataset for colorectal polyps classification and adenoma dysplasia grading. In *2021 IEEE International Conference on Image Processing (ICIP)*, 76–80 (IEEE, 2021).
127. Brummer, O., Polonen, P., Mustjoki, S. & Bruck, O. Integrative analysis of histological textures and lymphocyte infiltration in renal cell carcinoma using deep learning. *bioRxiv* 2022–08 (2022).
128. Huo, X. *et al.* Comprehensive ai model development for gleason grading: From scanning, cloud-based annotation to pathologist-ai interaction (2022).
129. Aresta, G. *et al.* Bach: Grand challenge on breast cancer histology images. *Medical image analysis* **56**, 122–139 (2019).
130. Tolkach, Y. *et al.* Artificial intelligence for tumour tissue detection and histological regression grading in oesophageal adenocarcinomas: a retrospective algorithm development and validation study. *The Lancet Digital Health* **5**, e265–e275 (2023).

131. Howard, F. M. *et al.* The impact of site-specific digital histology signatures on deep learning model accuracy and bias. *Nature communications* **12**, 4423 (2021).
132. Macenko, M. *et al.* A method for normalizing histology slides for quantitative analysis. In *2009 IEEE international symposium on biomedical imaging: from nano to macro*, 1107–1110 (IEEE, 2009).
133. Chen, C. *et al.* Fast and scalable search of whole-slide images via self-supervised deep learning. *Nature Biomedical Engineering* **6**, 1420–1434 (2022).
134. Li, S. *et al.* High-order correlation-guided slide-level histology retrieval with self-supervised hashing. *IEEE Transactions on Pattern Analysis and Machine Intelligence* (2023).
135. Komura, D. *et al.* Restaining-based annotation for cancer histology segmentation to overcome annotation-related limitations among pathologists. *Patterns* **4** (2023).
136. Cheng, B., Misra, I., Schwing, A. G., Kirillov, A. & Girdhar, R. Masked-attention mask transformer for universal image segmentation. In *2021 IEEE/CVF Conference on Computer Vision and Pattern Recognition (CVPR)* (2022).
137. Fang, Y. *et al.* Eva: Exploring the limits of masked visual representation learning at scale. In *Proceedings of the IEEE/CVF Conference on Computer Vision and Pattern Recognition*, 19358–19369 (2023).
138. Fang, Y. *et al.* Eva-02: A visual representation for neon genesis. *arXiv preprint arXiv:2303.11331* (2023).
139. Li, Y., Mao, H., Girshick, R. & He, K. Exploring plain vision transformer backbones for object detection. In *European Conference on Computer Vision*, 280–296 (Springer, 2022).
140. Chen, Z. *et al.* Vision transformer adapter for dense predictions. In *The Eleventh International Conference on Learning Representations* (2023).
141. Wang, Y., Chao, W.-L., Weinberger, K. Q. & Van Der Maaten, L. Simpleshot: Revisiting nearest-neighbor classification for few-shot learning. *arXiv preprint arXiv:1911.04623* (2019).
142. Snell, J., Swersky, K. & Zemel, R. Prototypical networks for few-shot learning. *Advances in neural information processing systems* **30** (2017).
143. Lu, M. Y. *et al.* Ai-based pathology predicts origins for cancers of unknown primary. *Nature* **594**, 106–110 (2021).
144. Liang, J. *et al.* Deep learning supported discovery of biomarkers for clinical prognosis of liver cancer. *Nature Machine Intelligence* **5**, 408–420 (2023).
145. Abdul Jabbar, K. *et al.* Geospatial immune variability illuminates differential evolution of lung adenocarcinoma. *Nature Medicine* 1–9 (2020).
146. Wang, X. *et al.* Spatial interplay patterns of cancer nuclei and tumor-infiltrating lymphocytes (tils) predict clinical benefit for immune checkpoint inhibitors. *Science Advances* **8**, eabn3966 (2022).
147. Leo, P. *et al.* Computationally derived cribriform area index from prostate cancer hematoxylin and eosin images is associated with biochemical recurrence following radical prostatectomy and is most prognostic in gleason grade group 2. *European urology focus* **7**, 722–732 (2021).
148. Jaume, G. *et al.* Quantifying explainers of graph neural networks in computational pathology. In *Proceedings of the IEEE/CVF Conference on Computer Vision and Pattern Recognition*, 8106–8116 (2021).
149. Pati, P. *et al.* Hierarchical graph representations in digital pathology. *Medical image analysis* **75**, 102264 (2022).

150. Kolesnikov, A., Zhai, X. & Beyer, L. Revisiting self-supervised visual representation learning. In *Proceedings of the IEEE/CVF conference on computer vision and pattern recognition*, 1920–1929 (2019).
151. Zhai, X., Oliver, A., Kolesnikov, A. & Beyer, L. S4l: Self-supervised semi-supervised learning. In *Proceedings of the IEEE/CVF international conference on computer vision*, 1476–1485 (2019).
152. Chen, R. J. *et al.* Scaling vision transformers to gigapixel images via hierarchical self-supervised learning. In *Proceedings of the IEEE/CVF Conference on Computer Vision and Pattern Recognition* (2022).
153. Devlin, J., Chang, M.-W., Lee, K. & Toutanova, K. Bert: Pre-training of deep bidirectional transformers for language understanding. *Proceedings of the 2019 Conference of the North American Chapter of the Association for Computational Linguistics: Human Language Technologies, Volume 1 (Long and Short Papers)* (2018).
154. Tian, K. *et al.* Designing bert for convolutional networks: Sparse and hierarchical masked modeling. In *The Eleventh International Conference on Learning Representations* (2023).
155. Sablayrolles, A., Douze, M., Schmid, C. & Jégou, H. Spreading vectors for similarity search. In *International Conference on Learning Representations* (2019).
156. Touvron, H., Vedaldi, A., Douze, M. & Jegou, H. Fixing the train-test resolution discrepancy. In Wallach, H. *et al.* (eds.) *Advances in Neural Information Processing Systems*, vol. 32 (Curran Associates, Inc., 2019).
157. Dao, T., Fu, D. Y., Ermon, S., Rudra, A. & Ré, C. FlashAttention: Fast and memory-efficient exact attention with IO-awareness. In *Advances in Neural Information Processing Systems* (2022).
158. Chen, R. J. *et al.* Multimodal co-attention transformer for survival prediction in gigapixel whole slide images. In *Proceedings of the IEEE/CVF International Conference on Computer Vision*, 4015–4025 (2021).
159. Liu, Z. *et al.* Swin transformer: Hierarchical vision transformer using shifted windows. In *Proceedings of the IEEE/CVF International Conference on Computer Vision*, 10012–10022 (2021).
160. Kolesnikov, A. *et al.* Big transfer (bit): General visual representation learning. In *Computer Vision—ECCV 2020: 16th European Conference, Glasgow, UK, August 23–28, 2020, Proceedings, Part V 16*, 491–507 (Springer, 2020).
161. Loshchilov, I. & Hutter, F. Decoupled weight decay regularization. In *International Conference on Learning Representations* (2019).
162. Bentley, J. L. Multidimensional binary search trees used for associative searching. *Communications of the ACM* **18**, 509–517 (1975).
163. Zhu, C., Byrd, R. H., Lu, P. & Nocedal, J. Algorithm 778: L-bfgs-b: Fortran subroutines for large-scale bound-constrained optimization. *ACM Transactions on mathematical software (TOMS)* **23**, 550–560 (1997).
164. Mu, N., Kirillov, A., Wagner, D. & Xie, S. Slip: Self-supervision meets language-image pre-training. In *European Conference on Computer Vision*, 529–544 (Springer, 2022).
165. Li, A. C., Efros, A. A. & Pathak, D. Understanding collapse in non-contrastive siamese representation learning. In *European Conference on Computer Vision*, 490–505 (Springer, 2022).
166. Lee, D. H., Choi, S., Kim, H. J. & Chung, S.-Y. Unsupervised visual representation learning via mutual information regularized assignment. *Advances in Neural Information Processing Systems* **35**, 29610–29623 (2022).

167. Sariyıldız, M. B., Kalantidis, Y., Alahari, K. & Larlus, D. No reason for no supervision: Improved generalization in supervised models. In *The Eleventh International Conference on Learning Representations* (2023).
168. Fang, Z. *et al.* Seed: Self-supervised distillation for visual representation. In *International Conference on Learning Representations* (2020).
169. Pedregosa, F. *et al.* Scikit-learn: Machine learning in python. *the Journal of machine Learning research* **12**, 2825–2830 (2011).
170. Du, X., Zoph, B., Hung, W.-C. & Lin, T.-Y. Simple training strategies and model scaling for object detection. *ArXiv* **abs/2107.00057** (2021).
171. Ghiasi, G. *et al.* Simple copy-paste is a strong data augmentation method for instance segmentation. In *Proceedings of the IEEE/CVF conference on computer vision and pattern recognition*, 2918–2928 (2021).
172. El Banani, M., Desai, K. & Johnson, J. Learning visual representations via language-guided sampling. In *Proceedings of the IEEE/CVF Conference on Computer Vision and Pattern Recognition*, 19208–19220 (2023).
173. Allen, K., Shelhamer, E., Shin, H. & Tenenbaum, J. Infinite mixture prototypes for few-shot learning. In *International conference on machine learning*, 232–241 (PMLR, 2019).
174. Koch, G., Zemel, R., Salakhutdinov, R. *et al.* Siamese neural networks for one-shot image recognition. In *ICML deep learning workshop*, vol. 2 (Lille, 2015).
175. Vinyals, O., Blundell, C., Lillicrap, T., Wierstra, D. *et al.* Matching networks for one shot learning. *Advances in neural information processing systems* **29** (2016).
176. Edwards, H. & Storkey, A. Towards a neural statistician. In *International Conference on Learning Representations* (2017).
177. Yu, J.-G. *et al.* Prototypical multiple instance learning for predicting lymph node metastasis of breast cancer from whole-slide pathological images. *Medical Image Analysis* **85**, 102748 (2023).
178. Yang, J., Chen, H., Yan, J., Chen, X. & Yao, J. Towards better understanding and better generalization of low-shot classification in histology images with contrastive learning. In *International Conference on Learning Representations* (2021).
179. Tian, Y., Wang, Y., Krishnan, D., Tenenbaum, J. B. & Isola, P. Rethinking few-shot image classification: a good embedding is all you need? In *Computer Vision—ECCV 2020: 16th European Conference, Glasgow, UK, August 23–28, 2020, Proceedings, Part XIV 16*, 266–282 (Springer, 2020).
180. Wang, Y., Liu, Z., Luo, Y. & Luo, C. A transductive learning method to leverage graph structure for few-shot learning. *Pattern Recognition Letters* **159**, 189–195 (2022).
181. Xu, J. *et al.* Alleviating the sample selection bias in few-shot learning by removing projection to the centroid. *Advances in Neural Information Processing Systems* **35**, 21073–21086 (2022).
182. Zhu, H. & Koniusz, P. Transductive few-shot learning with prototype-based label propagation by iterative graph refinement. In *Proceedings of the IEEE/CVF Conference on Computer Vision and Pattern Recognition*, 23996–24006 (2023).
183. Fei, N., Gao, Y., Lu, Z. & Xiang, T. Z-score normalization, hubness, and few-shot learning. In *Proceedings of the IEEE/CVF International Conference on Computer Vision*, 142–151 (2021).

184. Stojanov, S., Thai, A. & Rehg, J. M. Using shape to categorize: Low-shot learning with an explicit shape bias. In *Proceedings of the IEEE/CVF conference on computer vision and pattern recognition*, 1798–1808 (2021).
185. Lloyd, S. Least squares quantization in pcm. *IEEE transactions on information theory* **28**, 129–137 (1982).
186. Zhu, X., Yao, J., Zhu, F. & Huang, J. Wsisa: Making survival prediction from whole slide histopathological images. In *Proceedings of the IEEE/CVF Conference on Computer Vision and Pattern Recognition*, 7234–7242 (2017).
187. Yao, J., Zhu, X. & Huang, J. Deep multi-instance learning for survival prediction from whole slide images. In *International Conference on Medical Image Computing and Computer-Assisted Intervention*, 496–504 (Springer, 2019).
188. Yao, J., Zhu, X., Jonnagaddala, J., Hawkins, N. & Huang, J. Whole slide images based cancer survival prediction using attention guided deep multiple instance learning networks. *Medical Image Analysis* **65**, 101789 (2020).
189. Li, R., Yao, J., Zhu, X., Li, Y. & Huang, J. Graph cnn for survival analysis on whole slide pathological images. In *International Conference on Medical Image Computing and Computer-Assisted Intervention*, 174–182 (Springer, 2018).
190. Sivic & Zisserman. Video google: A text retrieval approach to object matching in videos. In *Proceedings ninth IEEE international conference on computer vision*, 1470–1477 (IEEE, 2003).
191. Fei-Fei, L. & Perona, P. A bayesian hierarchical model for learning natural scene categories. In *2005 IEEE Computer Society Conference on Computer Vision and Pattern Recognition (CVPR'05)*, vol. 2, 524–531 (IEEE, 2005).
192. Cruz-Roa, A., Caicedo, J. C. & González, F. A. Visual pattern mining in histology image collections using bag of features. *Artificial intelligence in medicine* **52**, 91–106 (2011).
193. Xu, Y. *et al.* Weakly supervised histopathology cancer image segmentation and classification. *Medical image analysis* **18**, 591–604 (2014).
194. Roetzer-Pejrimovsky, T. *et al.* The digital brain tumour atlas, an open histopathology resource (2022). URL <https://kg.ebrains.eu/search/instances/Dataset/8fc108ab-e2b4-406f-8999-60269dc1f994>.
195. Pati, P. *et al.* Weakly supervised joint whole-slide segmentation and classification in prostate cancer. *arXiv preprint arXiv:2301.02933* (2023).
196. Kather, J. N., Halama, N. & Marx, A. 100,000 histological images of human colorectal cancer and healthy tissue (2018). URL <https://doi.org/10.5281/zenodo.1214456>.
197. Brück, O. & Brummer, O. Training data for the "Integrative Analysis of Histological Textures and Lymphocyte Infiltration in Renal Cell Carcinoma using Deep Learning" (2022). URL <https://doi.org/10.5281/zenodo.7898308>.
198. Tolkach, Y. Datasets for Publication "Artificial intelligence for tumor detection and histological regression grading in oesophageal adenocarcinomas: a retrospective algorithm development and validation study" Tolkach Y. *et al.* (2023). URL <https://doi.org/10.5281/zenodo.7548828>.
199. Bertero, L. *et al.* Unitopatho (2021). URL <https://dx.doi.org/10.21227/9fsv-tm25>.
200. Kather, J. N. Histological image tiles for tcga-crc-dx, color-normalized, sorted by msi status, train/test split (2020). URL <https://zenodo.org/record/3832231>.

201. Komura, D. & Ishikawa, S. Histology images from uniform tumor regions in TCGA Whole Slide Images (2021). URL <https://doi.org/10.5281/zenodo.5889558>.
202. Abousamra, S. *et al.* Deep learning-based mapping of tumor infiltrating lymphocytes in whole slide images of 23 types of cancer. *Frontiers in oncology* **11**, 806603 (2022).
203. Kaczmarzyk, J. R., Abousamra, S., Kurc, T., Gupta, R. & Saltz, J. Dataset for tumor infiltrating lymphocyte classification (304,097 image patches from TCGA) (2022). URL <https://doi.org/10.5281/zenodo.6604094>.
204. Paszke, A. *et al.* Pytorch: An imperative style, high-performance deep learning library. *Advances in neural information processing systems* **32** (2019).
205. Goldberger, A. L. *et al.* Physiobank, physiotoolkit, and physionet: components of a new research resource for complex physiologic signals. *circulation* **101**, e215–e220 (2000).
206. Azizi, S. *et al.* Medical ai research foundations: A repository of medical foundation models (2023). URL <https://physionet.org/content/medical-ai-research-foundation/1.0.0/>.
207. Wu, Y., Kirillov, A., Massa, F., Lo, W.-Y. & Girshick, R. Detectron2. <https://github.com/facebookresearch/detectron2> (2019).
208. Clark, K. *et al.* The cancer imaging archive (tcia): maintaining and operating a public information repository. *Journal of digital imaging* **26**, 1045–1057 (2013).